Probing Spin in Organic Semiconductors via Magnetic Resonance

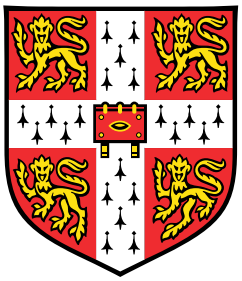

Remington Lane Carey

Robinson College
University of Cambridge

This dissertation is submitted for the degree of
Doctor of Philosophy

Department of Physics

May 2022

DECLARATION

I hereby declare that except where specific reference is made to the work of others, the contents of this dissertation are original and have not been submitted in whole or in part for consideration for any other degree or qualification in this, or any other university. This dissertation is my own work and contains nothing which is the outcome of work done in collaboration with others, except as specified in the text and Acknowledgements. This dissertation contains fewer than 60,000 words including appendices, bibliography, footnotes, tables and equations and has fewer than 150 figures.

Remington Lane Carey
May 2022

ABSTRACT

The study of spin dynamics in organic semiconductors is interesting not only for the exceptionally long spin lifetimes present in organics, but also because it can act as a probe of charge dynamics. Tools and techniques developed over the past 15 years aim to probe this connection, focusing on how the inexorable relationship between charge and spin can be leveraged in device design. Of particular interest is how quantum spin can be used to enhance or inhibit charge transport, and how spin itself can be used as a means of information transfer. Tied to all of these ideas is that spin can be altered via its couplings to the local environment. While this very property is what permits such techniques in the first place, it also introduces the challenge of preventing unwanted changes in spin. Much research has gone into understanding the coupling mechanisms that influence spin, and how to tailor molecules for device-specific goals.

This thesis uses magnetic resonance techniques to explore spin dynamics in detail. Chapter 1 is an introduction to the topic, while Chapters 2, 3, and 4 provide the theoretical and experimental background necessary to analyze the data presented. Chapter 5 is the first experimental chapter. The measurements described within are designed to probe spin relaxation at temperatures between 5 and 300 K, and emphasize especially those occurring between 150 and 300 K — a regime not currently well modeled. By using ambipolar semiconductors, the research links the spatial extent of the wavefunction and its position along the semiconductor backbone to relaxation via nuclear torsion. This is the first experimental evidence for the relaxation model at 'high temperatures' (150 - 300 K) first proposed by our group in 2019. Chapter 6 continues work on ambipolar systems. In this case, electrically detected magnetic resonance is used to understand how spin affects electrical currents flowing through devices. We sweep through all regimes of device operation (electron-only, ambipolar, hole-only) to provide evidence for both bipolaron-inhibited and recombination-assisted currents. Chapter 7 focuses on small-molecule crystalline systems rather than amorphous polymers. In rubrene — a model system for organic field-effect transistors — we report microsecond-long relaxation times from 15 K all the way to room temperature. In the framework of the relaxation theory developed in Chapter 2, we show how such long and stable relaxation times are possible, and how spin-spin interactions manifest.

Probing Spin in Organic Semiconductors via Magnetic Resonance
Remington Lane Carey

ACKNOWLEDGEMENTS

The following seven chapters describe in detail the totality of my academic work in Cambridge over the past four years. While I don't want to diminish my own efforts, I also think it's fair to say that this would not exist if not for the many wonderful and supportive people in my life. To not recognize them and their efforts here would be a tremendous disservice.

To begin, I must thank Professor Henning Sirringhaus for his constant support — both financial and academic. He has always given me the freedom to pursue the projects I find most interesting, and has entrusted me with the tools to do so. In the moments I've been unsure of my own conclusions, I've always been able to count on him for appropriate validation, criticism, and commentary. His style of mentorship — giving students flexibility in their work and allowing them to progress at a reasonable, yet still comfortable, pace — has given me the time to be thorough and expansive in my own studies. I truly appreciate his support.

Not all PhD students have the luxury of having a mentor, let alone one who shares the same office as them. I am fortunate in that I had Dr. Sam Schott to guide me daily through the past four years, from teaching me about the coffee machine in lab to helping design the experiments in this thesis. Even with emails sent at midnight about single lines of code in a program, I knew I could rely on him. (To be honest, in retrospect I can't help but realize that I must have been a very annoying student. I hope this serves as a proper apology.)

Dr. Xinglong Ren is a second postdoctoral researcher to whom I owe great thanks. Though I've only known him for the final part of my PhD, a solid third of my experimental work was made possible by him. He has been flexible, ingenuitive, and a great source of insight on all things rubrene. I view all of my work in Chapter 7 as a collaborative effort between the two of us.

Traveling to various parts of Europe has been one of the most enjoyable parts of my time at Cambridge. Through funding from the European Research Council (ERC) on a Synergy Grant, I have had the opportunity to collaborate with researchers from across Europe, landing me in both Spain and Germany multiple times. As part of that collaboration, I owe thanks to Professor Jairo Sinova, Dr. Erik McNellis, and the INSPIRE group at Johannes Gutenberg Universität Mainz for their theoretical work in spin relaxation, and to Professor Ian McCulloch and his groups at Imperial College, London and King Abdullah University (KAUST) for their willingness to provide new and exciting systems to measure.

I must also thank Professor Jan Behrends at Freie Universität Berlin for his inspiration for and help in the EDMR measurements reported in Chapter 6. He has been incredibly generous in teaching our group how to perform such techniques, loaning the necessary equipment we need for them, and helping

us understand our results. To this day I wonder how much more I could have learned had I not been incredibly sleep-deprived and, what felt like, near-death when I first met him. Alas, my first night in Berlin was spent in a life-or-death battle with my sinuses due to the furry spectre of the cat that stayed in the AirBnB the night previous. I am aggressively allergic to cats.

While all the members of Henning's OE-FET group have been entertaining to work with, several deserve special recognition for their support: Dr. Radoslav Chakalov, Roger Beadle, and Tom Sharp for their efforts in all things technical and mechanical; Alan Turner for continually working to protect the EPR magnets from overheating in summer; Mingfeo Xiao for his help in fabricating the fused copolymers presented in Chapter 6 and 7; and Ian Jacobs for his constant willingness to provide chemistry advice and all-around helpful research attitude.

And, of course, I owe great thanks to all the friends and family who have made my time here all the more enjoyable. Our lab socials, board game evenings, and nights out have made the past four years fly by. I'm already beginning to miss them. Special recognition goes to my boyfriend, Dániel Besenyői, who has been an incredible support and constant source of laughter since the day we met. And finally to my parents, Lane and Diana Carey, who have always been my proudest supporters. I could never thank them enough for all that they've given me. This thesis is dedicated to them.

NOTES

The below notation is used in mathematical expressions. Exceptions occur only in instances where there is a near-universal acceptance of some other style. (For example, the g-tensor will not be in calligraphic font.)

- Vectors are represented by boldface, non-italicized letters (e.g., $\mathbf{p}$);
- matrices are represented by Greek letters (e.g., the Pauli spin matrices σ_i);
- second-rank tensors are represented by boldface, script, Roman letters (e.g., $\boldsymbol{\mathcal{D}}$).

The International System of Units (SI) is used in this report. Constants used are as follows:

Symbol	**Name**	**Value**	**Units**
g_e	Free electron g-factor	$2.002\,319\,304\,362\,56(35)$	
$\hbar$	Reduced Planck constant	1.054×10^{-34}	$\mathrm{J\,s}$
q	Elementary charge	1.602×10^{-19}	C
m	Electron mass	9.109×10^{-31}	kg
m_p	Proton mass	1.673×10^{-27}	kg
c	Speed of light	2.998×10^{8}	$\mathrm{m\,s^{-1}}$
ε_0	Vacuum permittivity	8.854×10^{-12}	$\mathrm{F\,m^{-1}}$
μ_0	Vacuum permeability	1.256×10^{-6}	$\mathrm{H\,m^{-1}}$
k_B	Boltzmann constant	1.381×10^{-23}	$\mathrm{N\,A^{-2}}$
$\mu_\mathrm{B} \equiv q\hbar/2m$	Bohr magneton	9.274×10^{-24}	$\mathrm{J\,T^{-1}}$
$\gamma_\mathrm{e} \equiv g_\mathrm{e}\mu_\mathrm{B}/\hbar$	Free electron gyromagnetic ratio	1.761×10^{11}	$\mathrm{rad\,s^{-1}\,T^{-1}}$
$\mu_\mathrm{N} \equiv q\hbar/2m_\mathrm{p}$	Nuclear magneton	5.051×10^{-27}	$\mathrm{J\,T^{-1}}$

TABLE OF CONTENTS

Chapter 1

Introduction

For over a century semiconductors have been one of the most basic building blocks of modern development. From diodes and transistors to sensors and photocells, these semiconducting devices make up the bulk of everyday technology, and their use is only expected to grow.[1] While metals and inorganics dominated the electronics industry for decades, the introduction of a polyacetylene-based semiconducting switch by Dr. John McGinness in 1974 paved the way for their organic counterparts.[2] Today, organics comprise 37% of the display technology market.[3]

Given their applicability to wide-area, flexible displays and electronics, as well as their comparatively simple fabrication procedures, it is no surprise that organic semiconductors (OSCs) have exploded in popularity. With recognition by the 2000 Nobel Prize in Chemistry as well as the 2010 Millennium Technology Prize,[1] their relevance to everyday life is clear. As of 2020, photovoltaics alone have a worth of approximately $55.63 million,[4] while altogether the organic electronics industry is expected to reach $145.3 billion by 2026.[1]

Undoubtedly the greatest asset of organic semiconductors is their π-conjugated electronic structure. Though typically not able to produce electrical currents equaling those of inorganic devices, π-conjugated systems have two primary advantages: (1) the difference between their highest occupied orbital and lowest unoccupied orbital overlaps well with the range of visible light (see Figure 1.1 for reference), and (2) their extended structure allows for chemical tuning to tailor specific molecules to specific functions. Organic emitters, for example, have undergone three generations of improvement via chemical tuning.[5] These types of devices operate by converting injected electrical charges to emitted light, and their first iteration was limited to only 25% efficiency due to spin statistics. By leveraging spin-orbit coupling and replacing key molecular components with larger elements from the same column of the periodic table, second- and third-generation emitters have pushed this limit.[6] Organic displays, on the other hand, are appealing because they produce true black color, respond quickly to input, and allow for thin architecture and design.[7] Flexible displays in particular are germane to the use of organic technology since some classes of polymer possess both the electrical transport properties and low long-range structural order necessary to realize pliable electronics. (This should be compared to inorganics, where it is extremely rare to find materials with high disorder and high mobility.)

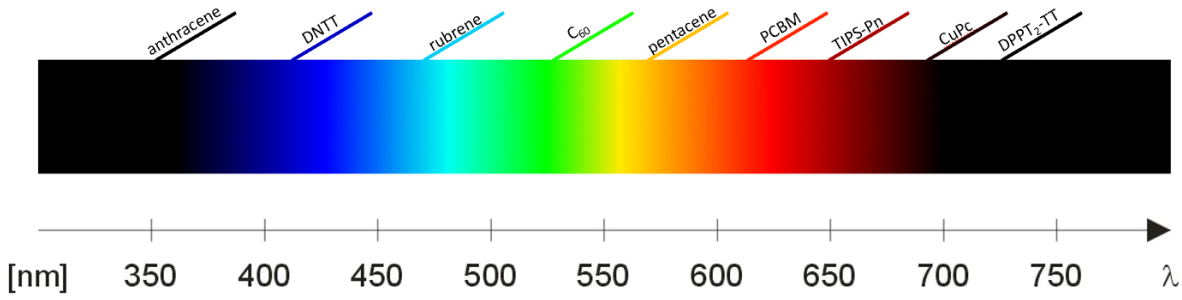

Fig. 1.1 Optical gaps of several select organic semiconductors. Data taken from Kim (2017).[8]

A key challenge to leveraging these advantages while also minimizing the corresponding disadvantages is an understanding of the fundamental charge-transport physics at play. The central figure of merit for transport properties is the electron (or hole) mobility μ, which characterizes how quickly an electron (or hole)* moves in response to an electric field. Over the course of three decades, the average mobility of p-type organic field-effect transistors (OFETs) – the most widely used type of transistor – has increased from 10^{-4} to over 10 cm^2/Vs[5] (see Figure 1.2). The highest-performing OFETs even outclass amorphous silicon, which is the most widely used inorganic for similar applications.[9]

Though various theories exist to explain charge transport in these systems, their relatively high degree of disorder and tunability make it difficult to adapt conventional models.[11,12] Nevertheless, an understanding of the microscopic charge transport mechanisms is possible, and these insights often prove necessary to overcome challenges in the field. One particular means by which to probe microscopic transport is to focus on electronic spin rather than charge. Because each charge carrier also possesses a spin, and because the electric and magnetic fields are manifestations of the same underlying field,[13] measurements of spin behavior are inexorably linked to measurements of charge behavior. As one example, the theoretical 25% efficiency of first-generation emitters was surpassed by placing moving spins in the presence of heavy nuclei, which is a leveraging of the spin-orbit interaction.[14] As a second example, recent studies have shown that mobility increases in polymeric systems can be attributed to both faster and farther charge motion, information gathered by measuring the average lifetime of a spin during electronic transit.[15]

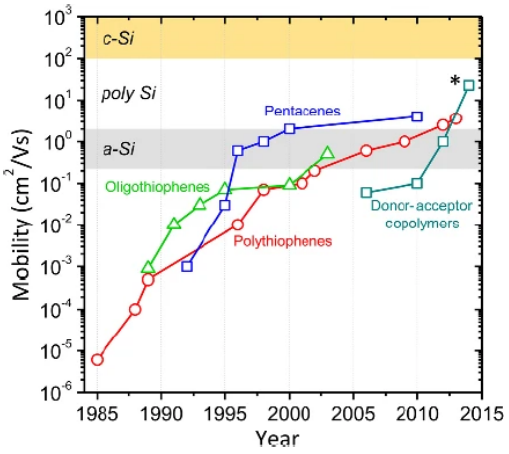

Fig. 1.2 The mobilities of several select organic semiconductors over time compared to amorphous silicon. Plot reproduced from Himmelberger (2015).[10]

*For ease of reading and writing, the term "carrier mobility" will be used in discussions in which the difference between a hole and an electron is irrelevant. When it is relevant, holes are often called p-type carriers while electrons are known as n-type carriers.

The study of spin in organic semiconductors is not only interesting for its application in charge transport, but spin-based devices are exceptional in their own right. Perhaps the most prominent example is magnetic random-access memory storage (MRAM), a spin-based type of computer information storage that has been used for the past forty years.[16] A more recent (and often deemed more exciting) application is that of quantum computers, which far exceed the capabilities of normal computers in a variety of algorithms and problem-solving challenges.[17] The advantage of spin-based computing comes from the mutability of spin: because it is not a conserved property in charge transport, spin-based information transfer makes device design quite flexible. In fact, the boon to MRAM came in the early 2000s, when the first mass-produced, non-volatile* MRAM chip required less power and a smaller architecture than its competitors.[18] Broadly speaking, information transport based on spin has been dubbed *spintronics* in reference to the charge-based electronics. Equivalently, a *spin current* refers to the spatial propagation of spin, which can be accomplished by producing an electric current that is *spin-polarized*, propagating a spin-flip down a line of immobile electrons, or by forcing spin-up and spin-down electrons to move in opposite directions.

There are two central hurdles to the production of spin transistors and spintronic devices using conventional metal and inorganic materials: low spin injection and short spin lifetimes. In other words, although spin-based circuits are advantageous because spin is not a conserved quantity, the ease with which it can be changed presents a challenge in ensuring information is preserved during transit. Fortunately, organics again offer a potential solution: due to their carbon- and hydrogen-based structure, these systems have orders-of-magnitude longer lifetimes than their inorganic counterparts. Their electronic structure offers a unique blend of charge-spin interactions, giving rise to the spin-Hall effect, inverse spin-Hall effect,[19] magnetoresistance in the absence of magnetic order,[20] and long spin diffusion lengths.[21]

Although the charge-transport and electronic properties of organic semiconductors have been extensively studied – revealing intricate relationships between device structure, molecular geometry, external stresses, and local morphologies[15,22–26] – similar studies of spin dynamics in organics are rarer. Far less is known about the unique spin physics these systems have to offer compared to charge physics. While it is well-documented that two key interactions drive spin relaxation — hyperfine fields due to nuclear magnetic moments and spin-orbit coupling due to electrons moving at relativistic speeds in electric fields — the connection between these, device and molecular properties, and charge transport still has much to be revealed.

It is the goal of this thesis to explore this connection in detail. The main characterization techniques employed are field-induced electron spin resonance (FI-ESR) and electrically detected magnetic resonance (EDMR), two methods which marry probes of charge transport with those of paramagnetic resonance. Chapter 2 will begin by introducing electron spin resonance (EPR)† with particular emphasis on theory, detection mechanisms, instrumentation, and best practices for the goals at hand. Starting with

*In this context, non-volatile means that information can be stored without the need for applied power.

†The terms electron paramagnetic resonance (EPR) and electron spin resonance (ESR) are used interchangeably in this work.

the Dirac equation, the Hamiltonian relevant to spin processes will be derived in detail, and particular focus will be given to terms that most often manifest in organic seminconductors. The types of signals commonly observed in organic EPR will be derived and discussed, especially in regards to how fitting parameters reveal information about electronic motion. The chapter will conclude by making a connection between coupling parameters in the spin Hamiltonian and observable features in the resonance signals, thus showing how a measurement can probe material microstructure and electronic environment.

Chapter 3 will introduce organic field-effect transitions, the devices used throughout this thesis to characterize the materials therein. It will then introduce field-induced electron spin resonance (FI-ESR), a powerful technique combining OFET and ESR principles to probe polaron dynamics in organics. Various applications of the technique in charge transport, molecular microstructure, electronic structure, and molecular crystallinity will be discussed to show the versatility of the technique, and the chapter will conclude with recent advancements and open questions.

Chapter 4 is an experimental chapter describing (1) the device fabrication methods used to design the samples reported here, and (2) experimental design and interpretation intricacies important to properly understanding the data presented. It will focus on measurement parameters, fitting strategies, and device variables that must be carefully considered to make accurate conclusions about the physics in question. Examples will be shown of many of the topics discussed in order to demonstrate how experimental artifacts manifest and may be avoided.

Previous work using FI-ESR has experimentally linked spin relaxation to charge transport at temperatures of 150 K and below. In this regime, decoherence between spins is governed by an interplay between local variations in hyperfine fields and hopping rates: as temperature increases, hopping rates also increase, thus more easily averaging local field differences. However, at higher temperatures (> 150 K) coherence is again lost. The reason behind this is still not understood fully, and so the experiments described in Chapter 5 attempt to elucidate this mechanism. They feature measurements performed on ambipolar molecules in order to link wavefunction delocalization with spin relaxation while avoiding a change in molecular microstructure. We show that high-temperature spin relaxation is driven by the spatial extent and location of the molecular wavefunction, whereby nuclear torsional modes relax spins by shuttling electrons back-and-forth across the polymer backbone. The conclusions reached provide an improved understanding of spin relaxation from 5 K to room temperature.

Chapter 6 further delves into spin-transport physics by probing only those polarons that contribute to charge transport. By again selecting a representative ambipolar system, we show that bipolaron formation inhibits charge transport in organic semiconducting devices. The chapter begins by describing electrically detected magnetic resonance (EDMR) — the characterization technique central to the experiments — then shows how it can be used to detect signatures of bipolaron-inhibited transport in organics. Not only does this observation clarify the origin of previously observed (and disputed) signals in EDMR, but also reveals the effect of bipolaron *type* on resonance signals. In particular, we observe that charge mobility and FET operational parameters can influence the strength of the EDMR signal by increasing or decreasing percolation paths through which polarons may travel. We thus conclude that

material electronic structure and device operational regimes are influential factors in such spin-dependent processes.

Chapter 7 moves focus from relatively disordered polymers to small-molecule, semi-crystalline systems. Rubrene, the inimitable organic in terms of mobility, is used in a capacitance architecture to probe spin dynamics in high-mobility systems. What is observed is that spins in rubrene have exceptionally long lifetimes even at room temperature, whereas those of amorphous systems are hundreds or even thousands of times shorter. This behavior is explained via the Redfield theory of spin relaxation, in which spins move between local environments faster than they decohere at each site. Finally, we conclude by reporting an observation of the spin-spin dipolar interaction at injection values greater than approximately 3×10^{12} charges/cm^2, indicating that typically neglected spin-spin physics may be present even in model systems.

CHAPTER 2

ELECTRON SPIN RESONANCE

This chapter will cover the theoretical background necessary to understand the experiments reported in this thesis. We begin with a basic overview of electron paramagnetic resonance experiments, then use the Dirac equation to derive the fundamental equations describing magnetic resonance in detail. We then develop a systematic framework in which to link the observables measured in electron spin resonance spectroscopy to physical, microscopic phenomena, with particular emphasis on electron-electron and electron-nucleon interactions. Next, we cover the various signals that might be observed in paramagnetic resonance experiments and how they are altered by physical characteristics of the system. Finally, we derive how the individual terms of the spin Hamiltonian manifest themselves as observable features in resonance spectra, and how different regimes of charge transport can affect both spectral shapes and intensities.

2.1 Foundations of Electron Spin Resonance

Before deriving ESR theory in detail, it is useful to give an overview of the process. Measurements can, in principle, be taken on any system with non-zero spin that is not restricted in changing its spin state,* though in practice this normally amounts to the study of radical molecules and polarons.† For simplicity, we shall always take the magnetic species to be an electron or pair of electrons, unless otherwise stated.

A typical experiment begins by applying a static field $B\hat{\mathbf{z}}$ to the paramagnetic species. While the two spin states are degenerate in energy in the absence of a field, the Zeeman interaction $\mathcal{H} = \mu_B g \mathbf{S} \cdot \mathbf{B}$ lifts this degeneracy, each spin state then possessing an energy $\pm\frac{1}{2} g \mu_B B$. An oscillating magnetic field $B_1 \cos \omega t$ is then applied to the sample, and the energy of the inidividual photons swept by modulating the frequency ω. When the energy of a photon of this field matches the energy gap of the split states, i.e.,

$$\hbar\omega = \Delta E = \mu_B g B, \tag{2.1}$$

*Such a restriction would likely be imposed by the Pauli exclusion principle.

†The difference between the two will be discussed in more detail in Chapter 3.

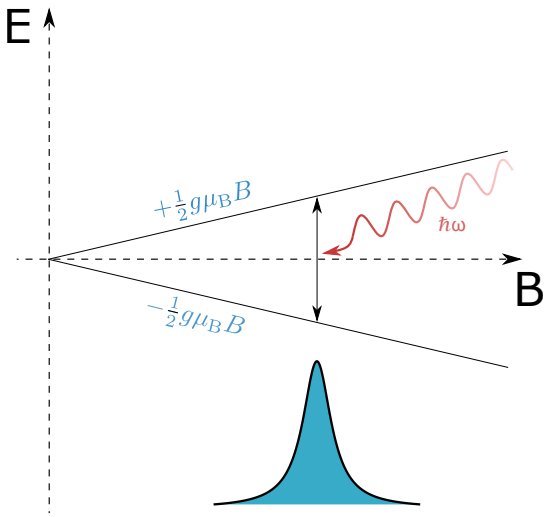

Fig. 2.1 A diagram depicting the lifting of degenerate spin states in a magnetic field due to the Zeeman interaction, as well as the resonance condition (2.1). The black lines indicate the energies of the two spin states as a function of B. When the gap between them (black double-sided arrow) matches the energy of the resonance field (red squiggly line; energy $\hbar\omega$), a transition is induced. The teal curve is a Lorentzian distribution and represents the EPR signal observed upon resonance. The cause of the shape of the signal will be discussed in Subsection 2.1.3.

an absorption signal — typically a Lorentzian lineshape — is observed. This is depicted in Figure 2.1.

In this expression $\hbar$ and μ_B are the reduced Planck's constant and Bohr magneton, respectively, while g is a material-dependent parameter; it is *not* the free-electron g-factor. The reason is that, while the energy of the spin states are primarily split by the Zeeman interaction, there are small, perturbative interactions that also affect the magnitude of this splitting. These interactions are usually dependent on the microscopic details of the system under study. We can therefore gain insight into the specifics of the material under study by measuring g, which is typically done by either fixing ω and sweeping B or fixing B and sweeping ω. Values of g are normally reported as a *shift* from that of a completely free electron, $g_e = 2.00231930436256(35)$.[27]

2.1.1 The Breit equation

The fundamental process behind electron spin resonance is the lifting of the energetic degeneracy of spin states. Because the Dirac equation introduces spin as an inherent property of electrons, it makes a nice starting place to understand this phenomenon. The Schrödinger equation can be used if the appropriate spin interactions are included in the Hamiltonian, but not only does this approach assume that all such interactions are known, it also gives predictions that differ from experiment by a factor of two. Quantum field theory may also be used, and, at first glance, is tempting because it gives the most accurate predictions known, but its corrections to Dirac theory are negligibly small for the purposes here and make the conceptual framework more cumbersome.

The Dirac equation for a single electron in an electric potential ϕ and a magnetic potential $\mathbf{A}$ is

$$\mathscr{D}\psi = i\hbar\frac{\partial}{\partial t}\psi \qquad \left(\mathscr{D} \equiv c\boldsymbol{\alpha}\cdot\left(\mathbf{p}+q\mathbf{A}\right) - q\phi + \beta mc^2\right), \tag{2.2}$$

which is identical to the Schrödinger equation after replacing the Hamiltonian $\mathscr{H}$ with the Dirac Hamiltonian $\mathscr{D}$.[13] This equation was designed to incorporate special relativity into quantum mechanics, so the quantities $\boldsymbol{\alpha}$ and β must be chosen such that this expression remains Lorentz invariant. Since there are no scalars satisfying this condition, matrices must be used, and 4-by-4 matrices are the smallest possible. It is standard to use the Pauli basis:

$$\alpha_{x,y,z} \equiv \begin{pmatrix} 0 & \sigma_{x,y,z} \\ \sigma_{x,y,z} & 0 \end{pmatrix} \qquad \beta \equiv \begin{pmatrix} \mathbb{1} & 0 \\ 0 & -\mathbb{1} \end{pmatrix}. \tag{2.3}$$

Accordingly, the Dirac equation yields a four-component solution for a single charged particle. Two components are identical to those of the Schrödinger equation for a spin-1/2 electron while the other two are commonly known as the positron solutions. At energies of magnitude far greater than the particle's rest energy, the components of the electron and of the positron are both significant and electron-positron pairs may be created.[28] In this report, however, we will be considering only energies of order rest energy, meaning only the electronic wavefunctions will be significant.[29] It is therefore desirable to rewrite the Dirac Hamiltonian such that the positron solutions make no contribution to the expectation values of observables. One such procedure, known as the Foldy-Wouthuysen Transformation, achieves this by expanding the Dirac Hamiltonian in powers of v/c.[30] The results of that procedure follow.

To account for interactions between the spins of electrons, one Dirac Hamiltonian must be added for each electron in the Dirac equation, along with their interaction terms. While possible, such a many-body approach is not always necessary because electron-electron interactions are often negligible. Indeed, for Chapter 5 and Chapter 6 the theory necessary to understand the results considers only a single-electron system.* However, because the spectra observed in Chapter 7 require consideration of the spin-spin dipolar interaction, this chapter will derive fully the Hamiltonian for a two-electron system. (The results of course apply to single-electron systems as well.) This section provides qualitative insight into how these interactions modify ESR spectra.

Classically, the electron-electron interaction term is the Coulomb interaction. It violates special relativity, however, which is unfortunate. To preserve the Lorentz invariance of the Dirac equation, quantum field theory may be used by assuming that the energy eigenvalues of the classical equation are known and then introducing an operator to act as a perturbation to these solutions. The resulting

*If, for some reason, someone were to return to this section after reading Chapter 6, they might point out that the experiments described in that chapter rely on two electrons meeting each other in transit. However, because the physics of the EDMR spectra reported depend on only one of the two spin species, the spin-spin interaction is not relevant. At most, in that chapter the effect of spins interacting is only to prevent two electrons from occupying the same state, which is not an explicit term in the Hamiltonian.

steady-state equation is

$$\left(\mathscr{D}_1+\mathscr{D}_2+\frac{1}{4\pi\varepsilon_0}\frac{q_1q_2}{r_{12}}-E\right)\psi=\mathscr{B}\psi, \tag{2.4}$$

where $\mathscr{D}_i$ is the single-electron Dirac operator for electron i, r_{12} is the position of electron 1 with respect to electron 2, and

$$\mathscr{B}\equiv\frac{1}{4\pi\varepsilon_0}\frac{q_1q_2}{2r_{12}}\left[\boldsymbol{\alpha}_1\cdot\boldsymbol{\alpha}_2+\frac{(\boldsymbol{\alpha}_1\cdot\mathbf{r}_{12})(\boldsymbol{\alpha}_2\cdot\mathbf{r}_{12})}{r_{12}^2}\right] \tag{2.5}$$

is the *Breit operator*.[31] Equation (2.4) is known as the *Breit equation*. Since only electrons are of concern, we will simplify notation by setting $q_1=q_2=q$ and $m_1=m_2=m$.

Solutions to the Breit equation contain four components for each of the two particles. As was mentioned previously, the energy regime covered here is low enough that the positron components may be neglected. A Foldy-Wouthuysen procedure may therefore be used to uncouple the electron and positron contributions. The details can be found in the original article by Chraplyvy (1953).[32] The result is a Hamiltonian which contains two solutions for each particle and, to order v^2/c^2, has three terms: $\mathcal{H}=\mathcal{H}_1+\mathcal{H}_2+\mathcal{H}_{\text{ee}}$.[29] The first two are identical in form and describe all single-electron interactions,

$$\mathcal{H}_i=mc^2+q\phi(\mathbf{r}_i)+\frac{1}{2m}(\boldsymbol{\alpha}_i\cdot\boldsymbol{\Pi}_i)^2-\frac{1}{8m^3c^2}(\boldsymbol{\alpha}_i\cdot\boldsymbol{\Pi}_i)^4+\frac{1}{8m^2c^2}\left[[\boldsymbol{\alpha}_i\cdot\boldsymbol{\Pi}_i,q\phi(\mathbf{r}_i)],\boldsymbol{\alpha}_i\cdot\boldsymbol{\Pi}_i\right], \tag{2.6}$$

(where $i=1,2$ and $\boldsymbol{\Pi}\equiv\mathbf{p}+q\mathbf{A}$) and the third describes the electron-electron interaction,

$$\begin{aligned}\mathcal{H}_{\text{ee}}=&\frac{1}{4\pi\varepsilon_0}\frac{q^2}{r_{12}}+\frac{1}{4\pi\varepsilon_0}\frac{1}{8m^2c^2}\left[\left[\boldsymbol{\alpha}_1\cdot\boldsymbol{\Pi}_1,\frac{q^2}{r_{12}}\right],\boldsymbol{\alpha}_1\cdot\boldsymbol{\Pi}_1\right]+\frac{1}{4\pi\varepsilon_0}\frac{1}{8m^2c^2}\left[\left[\boldsymbol{\alpha}_2\cdot\boldsymbol{\Pi}_2,\frac{q^2}{r_{12}}\right],\boldsymbol{\alpha}_2\cdot\boldsymbol{\Pi}_2\right]\\&-\frac{1}{8m^2c^2}\left(\left\{\{\boldsymbol{\alpha}_1\cdot\boldsymbol{\Pi}_1,\mathscr{B}\},\boldsymbol{\alpha}_2\cdot\boldsymbol{\Pi}_2\right\}+\left\{\{\boldsymbol{\alpha}_2\cdot\boldsymbol{\Pi}_2,\mathscr{B}\},\boldsymbol{\alpha}_1\cdot\boldsymbol{\Pi}_1\right\}\right).\end{aligned} \tag{2.7}$$

(The square brackets indicate the commutator and the curly brackets indicate the anticommutator.)

A better understanding of this Hamiltonian can be reached by defining the electromagnetic potentials in an electron spin resonance experiment. We choose to work in the Coulomb gauge so that there is no external electric potential, and we take the internal electric potential to be the sum of contributions from n nuclei, each possessing atomic number Z_n and at a distance r_n from the electron. We also assume that the magnetic potential can be divided into two parts: the first of a uniform, external magnetic field $\mathbf{B}\equiv B\hat{\mathbf{z}}$ (applied by the experimenter) and the second the sum of surrounding nuclear magnetic dipoles of magnetic moments $\boldsymbol{\mu}_n$. Then,

$$\phi=\phi_{\text{int}}=\frac{q}{4\pi\varepsilon_0}\frac{Z_n}{r_n}\qquad\qquad\mathbf{A}=\underbrace{\frac{1}{2}(\mathbf{B}\times\mathbf{r})}_{\mathbf{A}_0}+\underbrace{\frac{\mu_0}{4\pi}\frac{1}{r_n^3}(\boldsymbol{\mu}_n\times\mathbf{r}_n)}_{\mathbf{A}_n} \tag{2.8}$$

$$\mathbf{E} = \frac{q}{4\pi\varepsilon_0}\frac{Z_n}{r_n^3}\mathbf{r}_n - \frac{\partial \mathbf{A}}{\partial t} \qquad \mathbf{B} = B\hat{\mathbf{z}} \underbrace{- \frac{\mu_0}{4\pi}\frac{\boldsymbol{\mu}_n}{r_n^3} + 3\frac{\mu_0}{4\pi}\frac{(\boldsymbol{\mu}_n \cdot \mathbf{r}_n)}{r_n^5}\mathbf{r}_n}_{\mathbf{B}_n}. \tag{2.9}$$

The insertion of these potentials and fields into the Hamiltonians (2.6) and (2.7) is carried out in Harriman (1978).[29] The full result is lengthy, but fortunately we can omit terms not dependent on spin since ESR only detects the *difference(s)* in spin energy levels. This gives the much less lengthy*

$$\begin{aligned}
\mathcal{H} = \sum_{i=1,2} \Bigg\{ & -\frac{1}{4\pi\varepsilon_0}\frac{q^2\hbar}{4m^2c^2}\underbrace{\boldsymbol{\sigma}_i \cdot \sum_n \frac{Z_n}{r_{in}^3}\mathbf{L}_{in}}_{\mathcal{H}_{\mathrm{so}}} + \frac{1}{\sqrt{\varepsilon_0\mu_0}}\frac{q\hbar}{2mc}\Bigg[\underbrace{\boldsymbol{\sigma}_i \cdot \mathbf{B}}_{\mathcal{H}_{\mathrm{sZ}}} + \frac{\mu_0}{4\pi}\sum_n \underbrace{\left(-\frac{\boldsymbol{\sigma}_i \cdot \boldsymbol{\mu}_n}{r_{in}^3} + 3\frac{(\boldsymbol{\sigma}_i \cdot \mathbf{r}_{in})(\boldsymbol{\mu}_n \cdot \mathbf{r}_{in})}{r_{in}^5}\right)}_{\mathcal{H}_{\mathrm{hf\,sZ}}}\Bigg] \\
& + \frac{1}{\sqrt{\varepsilon_0\mu_0}}\frac{q}{mc}\left(\frac{1}{2}\underbrace{\mathbf{B} \cdot \mathbf{L}_i}_{\mathcal{H}_{\mathrm{oZ}}} + \frac{\mu_0}{4\pi}\sum_n \underbrace{\frac{1}{r_{in}^3}\boldsymbol{\mu}_n \cdot \mathbf{L}_{in}}_{\mathcal{H}_{\mathrm{hf\,oZ}}}\right)\Bigg\} - \frac{q^2}{4\pi\varepsilon_0}\frac{\hbar}{8m^2c^2}\underbrace{\left(\frac{1}{r_{12}^3}\boldsymbol{\sigma}_1 \cdot \mathbf{L}_{12} + \boldsymbol{\sigma}_1 \cdot \mathbf{L}_{12}\frac{1}{r_{12}^3}\right)}_{\mathcal{H}_{\mathrm{ee\,s_1o_1}}} \\
& - \frac{q^2}{4\pi\varepsilon_0}\frac{\hbar}{8m^2c^2}\underbrace{\left(\frac{1}{r_{12}^3}\boldsymbol{\sigma}_2 \cdot \mathbf{L}_{21} + \sigma_2 \cdot \mathbf{L}_{21}\frac{1}{r_{12}^3}\right)}_{\mathcal{H}_{\mathrm{ee\,s_2o_2}}} - \frac{q^2}{4\pi\varepsilon_0}\frac{\hbar}{2m^2c^2}\frac{1}{r_{12}^3}\underbrace{(\boldsymbol{\sigma}_2 \cdot \mathbf{r}_{12} \times \mathbf{p}_1 - \boldsymbol{\sigma}_1 \cdot \mathbf{r}_{12} \times \mathbf{p}_2)}_{\mathcal{H}_{\mathrm{ee\,soo}}} \\
& + \frac{q^2}{4\pi\varepsilon_0}\frac{\hbar^2}{4m^2c^2}\frac{1}{r_{12}^3}\underbrace{\left[\boldsymbol{\sigma}_1 \cdot \boldsymbol{\sigma}_2 - 3\frac{(\boldsymbol{\sigma}_1 \cdot \mathbf{r}_{12})(\boldsymbol{\sigma}_2 \cdot \mathbf{r}_{12})}{r_{12}^2}\right]}_{\mathcal{H}_{\mathrm{ee\,dipolar}}} - \frac{q^2}{4\pi\varepsilon_0}\frac{8\pi}{3}\frac{\hbar^2}{4m^2c^2}\underbrace{\boldsymbol{\sigma}_1 \cdot \boldsymbol{\sigma}_2\delta(\mathbf{r}_{12})}_{\mathcal{H}_{\mathrm{ee\,contact}}}
\end{aligned} \tag{2.10}$$

(where $\mathbf{L}_{ij} \equiv \mathbf{r}_{ij} \times \mathbf{p}_i$ indicates the angular momentum operator of particle i measured with respect to particle j). This expression is frighteningly complex, but fortunately we do not plan to actually use it. Instead, it is written out here to explicitly show each interaction in the two-electron spin Hamiltonian. Each term listed will be discussed in detail, and all are relevant for the theory developed later to understand the results reported herein.

$\mathcal{H}_{\mathrm{sZ}}$ and $\mathcal{H}_{\mathrm{hf\,sZ}}$ are the *spin Zeeman* and *hyperfine spin Zeeman* terms. They describe the interactions of the electrons' spins with the applied magnetic field and local magnetic fields from nuclear dipoles, respectively. $\mathcal{H}_{\mathrm{so}}$ is the *spin-orbit coupling* between each electron's spin and the effective magnetic field felt due to having an angular momentum in the electric field of surrounding nuclei. The $\mathcal{H}_{\mathrm{ee\,s}_i\mathrm{o}_i}$ terms similarly describe the interactions of each electron's spin with the effective magnetic field felt due to having an angular momentum in the electric field of the other electron. $\mathcal{H}_{\mathrm{ee\,soo}}$ is the *spin-other-orbit coupling* between electronic spin and the *real* magnetic field produced by the angular momentum of the other electron. $\mathcal{H}_{\mathrm{ee\,dipolar}}$ and $\mathcal{H}_{\mathrm{ee\ contact}}$ are the decoupling into orientation-dependent and orientation-independent components of the interaction between the magnetic dipoles of the two spin-1/2 particles. Finally, while $\mathcal{H}_{\mathrm{oZ}}$ and $\mathcal{H}_{\mathrm{hf\,oZ}}$ are spin-independent, they are included in the reduced Hamiltonian

*Though facetious, this statement is nonetheless true. It *is* much shorter.

because they are indirectly coupled to electronic spin via the spin Zeeman and spin-orbit coupling interactions.

2.1.2 An effective Hamiltonian for ESR

The full Hamiltonian (2.10) is quite intractable to work with in an experimental setting. A slight change in a molecule is likely to influence every term in some way, and the resulting net effect is extremely difficult to predict. It is far more convenient to work with a Hamiltonian that captures the relevant interactions in a given experiment while treating the remainder as perturbing forces. To do so systematically, we note that the Hamiltonian consists of terms of the form $\mathbf{A}\cdot\mathbf{B}$ in increasing powers of v/c, where $\mathbf{A}$ and $\mathbf{B}$ are vector operators that may be spin, magnetic field, position, etc. Our new Hamiltonian will consist of the unique zero-order terms (in v/c), while the higher-order terms will be mimicked by a tensor modifying the product of the operators. For a single spin, this gives the *effective Hamiltonian*

$$\mathcal{H} = \mathcal{H}_0 + \mathbf{S}\cdot\mathfrak{D}\cdot\mathbf{S} + \mathbf{S}\cdot\mathbf{g}\cdot\mathbf{B} + \sum_n \mathbf{S}\cdot\mathcal{A}_n\cdot\mathbf{I}_n + \sum_n \mathbf{I}_n\cdot\mathfrak{T}_n\cdot\mathbf{B} + \sum_{nn'}\mathbf{I}_n\cdot\mathfrak{Q}_{n,n'}\cdot\mathbf{I}_{n'}, \tag{2.11}$$

where $\mathcal{H}_0$ captures all spin-independent terms.* The center elements of each term (i.e., $\mathfrak{D}$, $\mathbf{g}$, $\mathcal{A}_n$, $\mathfrak{T}_n$, and $\mathfrak{Q}_{nn'}$) are tensors. They act to modify the major interactions of the full Hamiltonian (2.10) in such a way as to replicate the effects of the remaining interactions as small, perturbing forces. It is important to note that this Hamiltonian has not been derived directly from the reduced Breit Hamiltonian (2.10), but instead is a model intended to simplify the relevant interactions.† As such, various terms are added or removed depending on their relevance to individual measurements or discussions.

In this form, the Hamiltonian has been significantly simplified, but still remains larger than necessary for the work described herein. To further reduce it, we note that $\mathfrak{T}_n$ and $\mathfrak{Q}_{nn'}$ are the *nuclear Zeeman tensor* and *nuclear spin-spin tensor*, respectively. Because they are nuclear interactions in the spin Hamiltonian, they have no direct coupling to electron terms, and their indirect couplings are often third- or fourth-order; they will be dropped. The remaining terms, $\mathbf{g}$, $\mathcal{A}_n$, and $\mathfrak{D}$ are the *electron g-tensor*, *hyperfine tensor*, and *spin-spin dipolar tensor*, respectively. Their relevance to spin dynamics in organic semiconductors is difficult to overstate, and therefore we shall analyze them fully below.

The g-tensor; spin-orbit coupling

The $\mathbf{g}$-tensor encompasses all interactions between the electron spin and the magnetic field. Because it explicitly contains the electromagnetic potentials, it must include corrections for gauge-invariance to first-order, as well as relativistic corrections to the kinetic energy. To second order, it must include indirect interactions between spin and the magnetic field, such the orbital Zeeman effect (wherein the

*These include the Coulomb and kinetic energies, as well as the diamagnetic energy $\mathbf{B}\cdot\mathbf{d}\cdot\mathbf{B}$, where $\mathbf{d}$ is the magnetic susceptibility. The *effect* of the exchange interaction is also sometimes included here, though it's important to remember that this is not a true energetic interaction.

†Notice that the individual spin operators $\mathbf{S}_1$ and $\mathbf{S}_2$ have been replaced by the total spin operator $\mathbf{S} = \mathbf{S}_1 + \mathbf{S}_2$.

direct coupling between **L** and **B** results in an indirect coupling between **S** and **B** via conservation of total angular momentum) and the spin-orbit terms (whose dependence on **L** couples to **B** via the orbital Zeeman term).

Because there exists the free-electron g-factor g_e, it is often preferred to report the *shift* from this value, i.e., $\Delta\mathbf{g}$ as defined by $\mathbf{g} \equiv g_e\mathbb{1} + \Delta\mathbf{g}$. Following the steps of Harriman (1978),[29] we can decompose the *g-shift* into the sum of individual terms, three of which are relevant for a single electron while additional terms may be added to account for electron-electron spin-orbit effects. Because no such effects are relevant for the experiments described herein, we omit these.

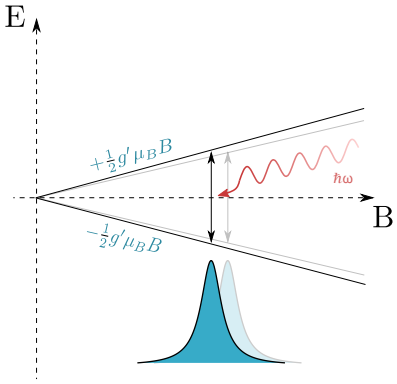

Fig. 2.2 The shift of an absorption peak due to an altered g value: g' here compared to g in Figure 2.1 (also shown as the translucent signal here).

In component form and introducing the symbol ψ to represent the state $|nlms\rangle$ (defined by the principal, azimuthal, magnetic, and spin quantum numbers), the first of the three single-electron terms is the relativistic correction to the kinetic energy,

$$\Delta g_{ab}^{\mathrm{KE}} = \delta_{ab}\frac{g_e\mu_B}{2m^2c^2}\left\langle \sum_i \mathbf{p}_i^2 \right\rangle_\psi \tag{2.12}$$

while the remaining two are

$$\Delta g_{ab}^{(1)} = \frac{1}{4\pi\varepsilon_0}\frac{g_e\mu_B^3}{\hbar^2c^2}\sum_n Z_n\left\langle \sum_i \frac{1}{r_{in}^3}[r_{in}^2\delta_{ab} - (\mathbf{r}_{in})_a(\mathbf{r}_{in})_b] \right\rangle_\psi \tag{2.13}$$

and*

$$\Delta g_{ab}^{(2)} = \frac{1}{4\pi\varepsilon_0}\frac{g_e\mu_B^3}{\hbar^2c^2}\sum_n Z_n\left\{ \sum_{\psi\neq\psi'}\left(\langle\psi'|\sum_i \frac{(\mathbf{L}_{in})_a}{r_{in}^3}|\psi\rangle \langle\psi|\sum_j (\mathbf{L}_{jn})_b|\psi'\rangle (E_{\psi'} - E_\psi)^{-1} + \text{c.c.} \right)\right\}. \tag{2.14}$$

These latter two terms couple the orbital Zeeman and spin-orbit interactions while also preserving gauge invariance. Collectively they are often referred to as the spin-orbit coupling term, and their significance is difficult to overstate. As a primary example, spin-orbit coupling and the g-shift are used to determine molecular orientation. The spin-orbit interaction is anisotropic with respect to the magnetic field, yet — because it is a term in the Hamiltonian — it can always be diagonalized with respect to the molecular frame. Thus, by performing angle-resolved measurements of the g-shift in EPR one can determine molecular crystal orientations. As a second example, the dependence of **g** on nuclear charge Z_n makes it obvious that molecular tuning can be achieved by incorporating heavier atoms when the

*The notation c.c. stands for the complex conjugate of the preceding term, and E_ψ is the energy of the state ψ.

effects of spin-orbit coupling are desirable. In organics, this usually amounts to replacing sulfur with selenium or tellurium.

The exact effect of **g** depends on the symmetries of the molecule in question as well as the dynamics of the spins contributing to the EPR signal. In gas and liquid samples, molecules (and thus spins) are free to rotate on timescales much shorter than individual data points are measured. This causes an averaging of the anisotropy of **g**, thus resulting in a single resonance peak whose center is determined by some linear combination of **g** components. (This is the situation often represented by the resonance condition (2.1).) Powder samples consist of a random distribution of fixed molecular orientations, thus resulting in an overlap of many different resonance peaks. In these cases, the resonance signal is not symmetric and all components of **g** are relevant. For other solids, the spectral signal will depend on the distribution of molecular orientations present, the symmetries of the molecule(s), and the dynamics of the electron spins. The spectral signal can range from many non-overlapping peaks to a single peak whose resonance center is determined by some linear combination of the components of **g**.[33]

The $\mathcal{A}$-tensor; hyperfine interactions

The hyperfine spin Zeeman interaction is the coupling between an electron's spin and the magnetic field felt from surrounding nonzero nuclear spins. It manifests as two terms to first order. The first is the Fermi contact term

$$\mathcal{A}^{\mathrm{F}}_{ab} = \frac{\mu_0}{4\pi}\frac{8\pi}{3}\delta_{ab} g_{\mathrm{e}} \mu_{\mathrm{B}} g_{\mathrm{n}} \mu_{\mathrm{n}} \left\langle \sum_{i,n} \delta(\mathbf{r}_{in}) \right\rangle_{\psi}, \tag{2.15}$$

which is necessarily isotropic and proportional to the charge density at the nucleus in question. (In this expression, $\delta(\mathbf{r}_{in})$ is the Dirac delta distribution as a function of the distance between electron i and nucleon n.) The dipolar hyperfine interaction, on the other hand,

$$\mathcal{A}^{\mathrm{dip.}}_{ab} = \frac{\mu_0}{4\pi} g_{\mathrm{e}} \mu_{\mathrm{B}} g_{\mathrm{n}} \mu_{\mathrm{n}} \left\langle \sum_{i,n} \frac{1}{r^3_{in}} \left[\delta_{ab} - 3\frac{(\mathbf{r}_{in})_a (\mathbf{r}_{in})_b}{r^2_{in}} \right] \right\rangle_{\psi}, \tag{2.16}$$

is an anisotropic coupling dependent on orbital shape.

The measurement of these two effects provides insight into molecular motion and configuration. For example, molecules in solution undergoing rapid rotation and translation will average out anisotropic contributions, thus yielding a zero contribution from the dipolar term. A more interesting application is that of the non-vanishing Fermi contribution: because this interaction requires overlap between nuclear and electric charge densities, one might expect zero contribution from this effect since charge carriers in organic semiconductors often lie in π-orbitals, which are, to first approximation, linear combinations of p orbitals (which have no electron density at nuclear sites); however, a Fermi contact contribution

is nevertheless observed, thus emphasizing the importance of orbital mixing* in these systems. This mixing often arises from spin-orbit and exchange couplings.

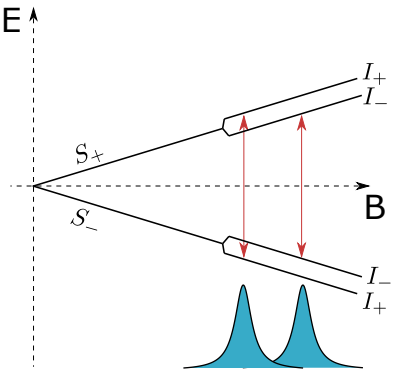

Fig. 2.3 A depiction of the multiple resonances observed due to a single spin$-1/2$ electron interacting with a single spin$-1/2$ nucleon. Four energy eigenstates exist, but spin conservation laws permit only two transitions. (The nuclear spin cannot change.)

The effect of $\mathcal{A}$ is simplest to understand when a single $I = 1/2$ nucleon interacts with an electron. In this case there are four nondegenerate spin states, one for each possible combination of electronic and nuclear spin. This is known as *hyperfine splitting* and is depicted in Figure 2.3. Two resonances are observed: one for the $|S_-, I_-\rangle \leftrightarrow |S_+, I_-\rangle$ and the other for $|S_-, I_+\rangle \leftrightarrow |S_+, I_+\rangle$. As suggested, transitions only occur between states in which nuclear spin does not change. By the nuclear resonance condition $\hbar\omega = \mu_n g_n B$, this is expected. Even in the case of a proton, μ_n is three orders of magnitude smaller than the Bohr magneton, meaning that resonance is extremely unlikely to occur at the B chosen for ESR.[34]

The more strongly coupled the electronic and nuclear spins are to each other, the greater the corresponding increase (or decrease) in energy. Thus, larger values of $\mathcal{A}$ give larger splitting between resonance peaks. For the specific case of $I = 1/2$ the distance between resonances is $\Delta B = |a|/2$† (where the constant a is simply the Fermi contact contribution (2.15) without the spin operator S_{in}), while the generalization to higher-spin and higher numbers of nuclei is straightforward.[29]

In the case that the splitting between hyperfine peaks is smaller than the spectral linewidth $1/\gamma_e T_2$, the individual peaks will remain unresolved and the observed spectrum will be a convolution of these hyperfine peaks with a Lorentzian signal (to be shown later in this chapter). This is one example of *inhomogeneous broadening*, which will be covered in Section 2.2. For now we simply note that if the number of nuclei broadening the spectrum is large, then the observed signal is a convolution of a Gaussian and Lorentzian. The average Fermi contact coupling constant $\overline{a}$ in this case can be estimated from the relation

$$\Delta B_{1/2} = \frac{\overline{a}}{\sqrt{\mathcal{N}}}, \tag{2.17}$$

where $\Delta B_{1/2}$ is the half-width-at-half-max of the recorded spectrum and $\mathcal{N}$ is the number of nuclei over which the electron is spread.[35]

In this case of unresolved, inhomogeneous broadening, (2.17) shows that the Gaussian linewidth narrows as the electron becomes spread over more nuclei. To understand this, we must extend Figure 2.3 to include one additional spin-1/2 nucleus. In this case, each I_+ and I_- line splits into two (just as the two S_+ and S_- states did). The splitting is symmetric, so the upper line/energy level that splits from the

*Specifically, between π- and σ-orbitals.

†The discussion in the previous section regarding measurement of individual components of $\mathbf{g}$ also applies to $\boldsymbol{\mathcal{A}}$.

$|S_+, I_-\rangle$ state overlaps exactly with the lower line that splits from the $|S_+, I_+\rangle$ state. As a result, only three energy levels are created, though the center one is doubly degenerate. Because the same scenario occurs for the $|S_-, I_-\rangle$ and $|S_-, I_+\rangle$ states, the result of adding the second nuclei is that six unique energy levels exist, with the middle level in each $S_\pm$ band being doubly occupied. Thus, this transition occurs with greater frequency than the others, and thus contributes more strongly to the ESR signal. Extending this logic to more nuclei results in the center energy being the dominant signal in EPR due to increased degeneracy, and thus the linewidth of the signal narrowing.

In organics, the most common sources of hyperfine splitting are from hydrogen and nitrogen, the most common isotopes of which carry nuclear spin 1/2 and 1, respectively. Note that equation (2.17) can only give a lower estimate of wavefunction extent, as it only captures portions of the wavefunction in contact with nuclei containing non-zero nuclear spin.

The $\mathcal{D}$-tensor; spin-spin interactions

The term $\mathbf{S}\cdot\mathcal{D}\cdot\mathbf{S}$ is relevant for samples in which electronic spins interact with one another. To first order it contains the contact and spin-spin dipolar interactions, while to second order it contains spin-orbit interactions; the second-order term will not be needed here.

The contact interaction is labeled $\mathcal{H}_{\text{ee contact}}$ in (2.10). In spherical tensor coordinates,* it has the form

$$\frac{\left\langle -\sum_{i<j}\delta(r_{ij})\mathscr{S}_0^{(0)}(ij)\right\rangle_\psi}{\left\langle \mathscr{S}_0^{(0)}\right\rangle_\psi}, \tag{2.18}$$

where $\mathscr{S}_0^{(0)}$ is a spherical tensor spin operator of rank zero (e.g., $\mathbf{S}^2$, $\mathbf{S}_1\cdot\mathbf{S}_2$, $\mathbf{I}^2$, $\mathbf{S}\cdot\mathbf{I}$).[29] Because it is independent of the magnetic spin quantum number, it provides a constant energy offset to the states. We shall ignore it here.

The dipolar interaction from (2.10) is often the most significant contribution to $\mathcal{D}$ in EPR experiments. In Cartesian coordinates it is

$$\mathcal{D}'_{ab} = \frac{\mu_0}{4\pi}\frac{4\mu_B^2}{S(2S-1)}\left\langle \sum_{i<j}\frac{r_{ij}^2\delta_{ab} - 3(r_{ij})_a(r_{ij})_b}{r_{ij}^5}\left(2S_{i,z}S_{j,z} - S_{i,x}S_{j,x} - S_{i,y}S_{j,y}\right)\right\rangle_\psi . \tag{2.19}$$

As expected, this term is only relevant for systems with $S > 1/2$.†‡

In general $\mathcal{D}$ is the electron-electron equivalent of the hyperfine coupling matrix $\mathcal{A}$, i.e., the magnetic interaction of two spins. The isotropic portion is captured in in the contact term, which is a diagonal matrix whose components depend only on the distance between the two electrons. Even in the absence of a magnetic field, the spin-spin contact term separates the energy of the singlet state from that

*Spherical tensor notation is used here because it allows for quick evaluation of many integrals using the Wigner-Eckart theorem. A summary of spherical tensor notation can be found in Appendix C.

†While the denominator vanishes if $S < 1$, the numerator does as well.

‡In this expression, i and j refer to electron indices and a and b run over the Cartesian indices x, y, and z.

of the three triplet states. Depicted on the left in Figure 2.4, this is one contribution to *zero-field splitting*. In the example shown the contact term is negative, meaning the singlet state is higher in energy. Note that resonance only occurs between the triplet substates. Moreover, resonance is strongest for the $|1,-1\rangle \leftrightarrow |1,0\rangle$ and $|1,+1\rangle \leftrightarrow |1,0\rangle$ transitions, but a weaker signal can be observed for $|1,-1\rangle \leftrightarrow |1,+1\rangle$. This latter peak is known as the *half-field* resonance, and occurs with low probability due to spin selection rules.

The anisotropic portion of $\mathfrak{D}$ is contained in $\mathfrak{D}'$. Representing the interaction between two magnetic dipoles, it further contributes to zero-field splitting by lifting the degeneracies of the triplet states at $B = 0$. While nonzero $\mathfrak{D}'$ will always split the $|1,+1\rangle$ and $|1,-1\rangle$ states from $|1,0\rangle$, the symmetry of the molecule will determine if the ± 1 states are split from each other.[36] Similar to $\mathcal{A}$, the distance between resonances gives a measure of $\mathfrak{D}'$. Because $\mathfrak{D}$ is an asymmetric, traceless tensor, only two parameters are needed to define it completely. It is customary to write them as

$$D \equiv \frac{3}{2}\mathcal{D}'_{\mathrm{Z}} \qquad\qquad E \equiv \frac{1}{2}(\mathcal{D}_{\mathrm{X}} - \mathcal{D}_{\mathrm{Y}}), \tag{2.20}$$

where $D_{X,Y,Z}$ are the principal components of $\mathfrak{D}'$.

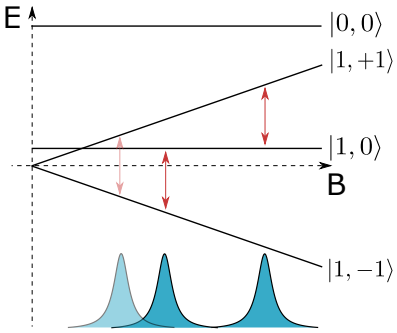

Fig. 2.4 A depiction of the multiple resonances observed due to the interaction of two spin$-1/2$ electrons. Two 'allowed' transitions exist, for which $\Delta m_s = \pm 1$. The 'forbidden' transition for $|1,-1\rangle \leftrightarrow |1,+1\rangle$ is occasionally observed. Even at zero magnetic field the spin states are not degenerate due to zero-field splitting and the exchange interaction.

2.1.3 The Bloch equations

A bulk sample will consist of many paramagnetic species described by the Hamiltonian (2.11). Each of these species will have a magnetic moment $\boldsymbol{\mu}$ and the net magnetization of the sample will be the sum of these moments, $\mathbf{M} \equiv \sum_i \boldsymbol{\mu}_i / V$. Assuming the species is not ferromagnetic, $\mathbf{M} = 0$ in the absence of any magnetic fields. This corresponds to the populations of the spin states being equal (which follows from their energies being equal). Once we apply the external field $B_0\hat{\mathbf{z}}$ however, the interaction $\boldsymbol{\mu} \cdot \mathbf{B}$ alters the energy of the z-spin states. For simplicity, 'spin states' will refer specifically to the z-spin states unless otherwise noted. In the case of a single free electron, there will be two spin states and we shall take the spin-up state to have the higher energy. In the case of two free electrons, we will use the singlet-triplet basis and take the triplet energy as being lowest for $m_{\mathrm{s}} = -1$ and highest for $m_{\mathrm{s}} = +1$.

The first interaction to consider in an ESR experiment is that of the sample and the static Zeeman-splitting field. The spin-up electrons are referred to as 'hot' because their energy has been raised. They will attempt to minimize their energetic increase by transferring energy to their molecular surroundings and flipping to a lower energy spin state. This process is known as *spin-lattice relaxation* (SLR). It leads to an excess of spins in the lower energy states compared to the higher energy states, i.e., $n_- > n_+$ for a radical and $n_{-1} > n_0 > n_{+1}$ for a diradical. There follows a net magnetization M_{z}^0 along the z-axis.[34] After sufficient time has passed since the application of a static field, the equilibrium magnetization of

the sample can be written in the form[37]

$$\mathbf{M}^0 = \chi_0 \mathbf{B}, \tag{2.21}$$

where the static susceptibility χ_0 depends on the number of nonzero magnetic moments in the sample.

For samples containing only molecules with one unpaired electron, N is a constant equal to the number of said electrons. If the Fermi level of the bulk is well below the thermal energy ($\varepsilon_\mathrm{F} \ll k_\mathrm{B}T$), Boltzmann statistics gives

$$\chi_0 = N\frac{\mu_\mathrm{B}^2 g^2}{3T}S(S+1) \qquad (\text{radical}, \varepsilon_\mathrm{F} \ll k_\mathrm{B}T), \tag{2.22}$$

which scales inversely with temperature and is known as the *Curie susceptibility*.[37] Alternatively, if the temperature is low enough that the Pauli exclusion principle becomes significant (i.e., $k_\mathrm{B}T \ll \varepsilon_\mathrm{F}$), Fermi-Dirac statistics give

$$\chi_0 = \frac{1}{(3\pi^2)^{2/3}}\frac{2m_e\mu_\mathrm{B}^2}{\hbar^2}\left(\frac{N}{V}\right)^{1/3} \qquad (\text{radical}, \varepsilon_\mathrm{F} \gg k_\mathrm{B}T), \tag{2.23}$$

which is independent of temperature and is known as the *Pauli susceptibility*.[37]

ESR measures the magnetization of a sample based on the electromagnetic energy it absorbs from an applied field. This is possible because the energy absorbed by the sample per unit time depends on its magnetization via

$$P = \frac{\mathrm{d}\mathcal{H}}{\mathrm{d}t} = -\frac{\mathrm{d}}{\mathrm{d}t}\sum_m \boldsymbol{\mu}_m \cdot \mathbf{B} = -V\frac{\mathrm{d}\mathbf{M}}{\mathrm{d}t}\cdot\mathbf{B}. \tag{2.24}$$

For a paramagnetic sample in an EPR experiment, the dynamics of magnetization are (see Appendix A)

$$\frac{\mathrm{d}\mathbf{M}}{\mathrm{d}t} = -g\mu_\mathrm{B}\mathbf{M}\times\mathbf{B} - \mathbf{T}\cdot(\mathbf{M} - M_z^0\hat{\mathbf{z}}), \tag{2.25}$$

where

$$\mathbf{T} \equiv (1/T_2, 1/T_2, 1/T_1). \tag{2.26}$$

These are known as the *Bloch equations*.[38] They show that M_z decays to M_z^0 after sufficient time has passed. The time describing the decay is T_1, the *spin-lattice* or *longitudinal relaxation time*. The latter name reflects the magnetic field and the magnetization being along the same axis; the former reflects the fact that z-oriented spins must exchange energy with the lattice to flip from the up-state to the down-state.[34] These equations also show that M_z and M_y precess around the z-axis; this corresponds to Larmor precession. Because there is no driving force in this direction, these magnetizations eventually decay to zero. The amount of time this requires is known as the *spin-spin* or *transverse relaxation time*,

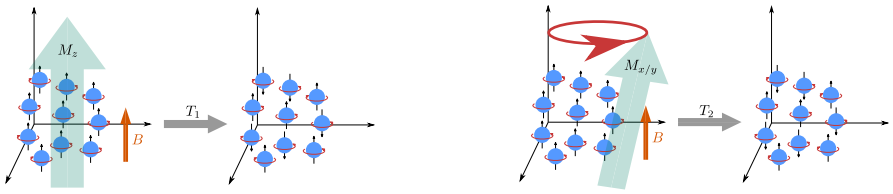

Fig. 2.5 Diagrams showing longitudinal (**left**) and transverse (**right**) relaxation. In longitudinal relaxation, the external field aligns a majority of spins with it, in turn creating a magnetization in that direction. Once the field is removed, the spins return to their equilibrium alignment. In transverse relaxation, the spins precess coherently around the external field (and the transverse components of magnetization follow). After the field is removed, the spins lose their coherence and the transverse magnetization vanishes.

T_2. While the latter name is clear, the former is chosen because spins can only change their x- and y-components by interacting with local fields produced by other spins. These spins can be from other electrons or from nucleons. Figure 2.5 schematically shows these two relaxation processes.

If $\mathbf{B}$ only includes a static magnetic field, the sample will reach equilibrium and stop absorbing energy. There must be a constant driving force to move the system out of equilibrium. This is normally done with a magnetic field that oscillates perpendicular to the static field. Taking it along the x-axis as $\mathbf{B}_{\text{mw}} = 2B_{\text{mw}} \cos \omega_{\text{mw}} t \hat{\mathbf{x}}$, Appendix A shows

$$M_x = B_{\text{mw}}(\chi' \cos \omega_{\text{mw}} t - \chi'' \sin \omega_{\text{mw}} t) = \mathcal{R}e\{\chi B_{\text{mw}} e^{i\omega_{\text{mw}} t}\} \tag{2.27}$$

where

$$\begin{aligned} \chi' &= \chi_0 \frac{\omega_{\text{L}} T_2^2 (\omega_{\text{L}} - \omega_{\text{mw}})}{1 + (\omega_{\text{L}} - \omega_{\text{mw}})^2 T_2^2 + \gamma^2 B_{\text{mw}}^2 T_1 T_2} \\ \chi'' &= \chi_0 \frac{\omega_{\text{L}} T_2}{1 + (\omega_{\text{L}} - \omega_{\text{mw}})^2 T_2^2 + \gamma^2 B_{\text{mw}}^2 T_1 T_2} \end{aligned} \tag{2.28}$$

are the components of a *complex susceptibility*, $\chi \equiv \chi' + i\chi''$.[38] The term χ' describes the dispersion of electromagnetic waves in the material while the term χ'' describes the material's absorption or radiation of energy.[39] The power absorbed over one cycle of the microwave field is[33]

$$\begin{aligned} \overline{P} &= \frac{V}{\mu_0} \omega_{\text{mw}} B_{\text{mw}}^2 \chi'' \\ &= \frac{V}{\mu_0} \chi_0 \frac{\omega_{\text{mw}} \omega_{\text{L}} B_{\text{mw}}^2 T_2}{1 + (\omega_{\text{L}} - \omega_{\text{mw}})^2 T_2^2 + \gamma^2 B_{\text{mw}}^2 T_1 T_2}. \end{aligned} \tag{2.29}$$

This is the equation describing the magnetic response of a system of identical spins at resonance. The actual shape of the spectral signal *observed*, however, will differ due to (1) measurement conditions and (2) the possibility of a sample containing multiple spin ensembles. While the effect of the former is only relevant in ensuring signals are fitted properly (and not related to the underlying physics at play), careful consideration is still warranted to ensure that extracted fitting parameters are accurate; these will be discussed fully in Chapter 4. The latter does manifest as a change in the spectral line, but this change is

straightforward to parameterize, and the physics of interest is still captured in (2.29) . Therefore it is this equation that is most relevant for theoretical discussion.

2.2 Lineshapes & Broadening

The absorption equation (2.29) can be rewritten as

$$\mathcal{L}(B|\omega_{\mathrm{mw}},\rho) = \frac{B_{\mathrm{mw}}^2\chi_0\gamma B\omega_{\mathrm{mw}}}{\sqrt{1+\gamma^2B_{\mathrm{mw}}^2T_1T_2}}\underbrace{\frac{1}{\pi\rho}\frac{\rho^2}{\rho^2+(\gamma B-\omega_{\mathrm{mw}})^2}}_{\mathscr{L}}, \tag{2.30}$$

where

$$\rho \equiv \frac{\sqrt{1+\gamma^2B_{\mathrm{mw}}^2T_1T_2}}{\gamma T_2} \tag{2.31}$$

is the half-width-at-half-height of the normalized Lorentzian function $\mathscr{L} = \mathscr{L}(B|\omega_{\mathrm{mw}},\rho)$.* It shows that the signal will be maximized at the resonance $\omega_L = \omega_{\mathrm{mw}}$.[36]

In this form, we see that a basic ESR signal has a Lorentzian lineshape whose width is determined by the transverse relaxation time, T_2. Because relaxation times are relevant to many spintronics processes, lineshape analysis is a fundamental part of ESR measurements. Of particular interest are the mechanisms by which linewidths may be broadened.

For a fixed frequency† the resonance condition (2.1) implies that a singular field amplitude will result in resonance, thus giving a delta function (or first derivative) as a signal. The reason this is not the case — as shown in the above equation — is as follows: Even in the limit of a single spin magically floating inside the cavity and somehow unaffected by all forces in the universe aside from the Zeeman and microwave fields, the observed signal would still have a Lorentzian lineshape. This is due to the finite broadening of energetic states, as described by the uncertainty principle: the energetic levels of the spin are not sharply defined, meaning a small range of values satisfy the resonance condition and thus give rise to a small, Lorentzian band of resonance positions.

Lineshapes described by the Lorentzian relation (2.30) between T_2 and the linewidth are known as *homogeneously broadened*. Physically, this means that every spin in the system has the same broadening of energy levels,‡. The above-mentioned broadening due to the finite lifetimes of states is one manifestation of homogeneous broadening; others include the spin dipolar interaction, the spin-lattice interaction, interactions with the microwave field, and—to be expanded upon later—motional narrowing. In essence, any interaction that affects all spins in the system identically will lead to homogeneous broadening.

*The vertical bar separates the swept variable from the parameter(s) needed to describe the distribution. The functional dependence of $\mathcal{L}$ is chosen to be B (or sometimes $\omega_{\mathrm{L}} = \gamma B$) because in a typical ESR experiment it is the Zeeman field that is swept and the oscillating field that is fixed.

†Or field amplitude, if you want to be a cowboy and sweep the frequency instead.

‡As suggested by choice of the adjective *homogeneous*.

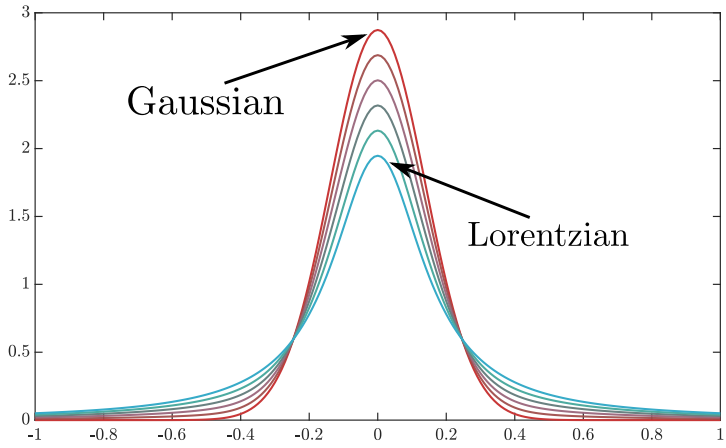

Fig. 2.6 The evolution of a Voigtian curve created from the weighted convolution of a Lorentzian and Gaussian with equal full-width-at-half-max. The dark red curve is a pure Gaussian contribution while the light blue curve is a pure Lorentzian contribution.

In many systems, however, it is not reasonable to treat all spins as equivalent. Often physical processes operate in such a way as to divide the system into different subsystems, each of which contains identical spins. In such cases, each subsystem contributes a unique Lorentzian to the overall signal. In rare instances each Lorentzian can be resolved fully, thus yielding a spectrum consisting of several non-overlapping Lorentzian. However, more often it occurs that g-factors are close enough and intrinsic linewidths broad enough that individual resolution is impossible; the signal is instead a convolution of Lorentzians. This is known as *inhomogeneous broadening*.[36] There are many possible causes of inhomogeneous broadening, such as small hyperfine splitting, anisotropy in a sample with randomly-oriented molecules, and electron-electron interactions. While the exact effect will depend on the mechanism(s) at play, it can usually be modeled by a Gaussian distribution of resonance centers whose variance is determined by the variance in local fields:[29]

$$\mathcal{G}(B|\omega_{\mathrm{mw}},B_{\nu}) = \frac{1}{\sqrt{2\pi B_{\nu}^2}}\exp\left[-\frac{(B-\omega_{\mathrm{mw}}/\gamma)^2}{2B_{\nu}^2}\right], \tag{2.32}$$

The overall lineshape in this case follows as a Gaussian distribution of Lorentzians:

$$\mathcal{V}(B|\omega_{\mathrm{mw}},B_{\nu},\rho) = \int_{-\infty}^{\infty}\mathcal{G}(B'|B_{\nu})\mathcal{L}(B-B'|\rho)dB'. \tag{2.33}$$

This convolution is known as a Voigtian.[40] It is normally only present at temperatures below 20 K for the organic samples described here. Because it is defined entirely in terms of the Lorentzian $\mathcal{L}$ and a fitting parameter B_{ν}, future discussions will focus exclusively on $\mathcal{L}$.

Finally, it should be noted that lineshapes other than Lorentzian, Gaussian, and Voigtian exist. Deriving them requires different assumptions about the basic Hamiltonian as well as the magnetic response of the system. Because these are not relevant to the data described here, they will be omitted.

2.3 The Microscopic Origins of Spin Relaxation

As mentioned in the introduction of this thesis, long spin lifetimes are necessary to realize spin transistors and realistically produce spintronic circuits on the mass scale. In the Bloch equations these lifetimes have been introduced simply as phenomenological parameters for exponential decay. To properly make the case for increasing relaxation times via molecular tuning, we first need to understand the microscopic origins of these parameters. The derivations in this section to do so will follow the works of Pake and Slichter.[33,38]

At the macroscopic level, T_1 and T_2 describe how quickly net magnetization decays back to equilibrium along the quantization axis and in the transverse plane, respectively. In either case, this process results from different spins in the ensemble evolving differently than others. In other words, the system contains many different ensembles, each of which is described by a different effective spin Hamiltonian (see (2.11)). This translates into quantum mechanics by describing the system via a spin density matrix ρ. Then, the dynamics of magnetization are given by the ensemble average of the spin operator (see Appendix B),

$$\begin{aligned}\frac{\mathrm{d}}{\mathrm{d}t}\overline{\langle \mathbf{M}\rangle} &= \frac{\mathrm{d}}{\mathrm{d}t}\sum_{n,n'}\langle n|\rho|n'\rangle\langle n'|\mathbf{M}|n\rangle \\ &= \sum_{n,n'}\frac{\mathrm{d}}{\mathrm{d}t}\Big(\langle n|\rho|n'\rangle\Big)\langle n'|\mathbf{M}|n\rangle,\end{aligned} \tag{2.34}$$

and the evolution of the density matrix is given by

$$\frac{\partial\rho}{\partial t} = \frac{i}{\hbar}[\rho, \mathcal{H}_0 + \mathcal{H}_1], \tag{2.35}$$

where the total Hamiltonian is the sum of the static Zeeman interaction and a perturbative field that varies both in space and time. This perturbative field is due to one or more terms in the effective Hamiltonian (2.11). For a general treatment, we note that each term effectively equates to a spin interacting with a local magnetic field. We can characterize fluctuations in this field by the magnitude of their root-mean-square variance, B_{rms}, as well as the average fluctuation time, τ_c. We assume that fluctuations in the perturbative field are random such that both their ensemble and time averages vanish.*

Without the perturbative field, the density matrix would simply be

$$\rho(t) = e^{-i\mathcal{H}_0 t/\hbar}\rho(0)e^{i\mathcal{H}_0 t/\hbar}, \tag{2.36}$$

which suggests a solution to the time-dependent equation of the form

$$\rho(t) = e^{-i\mathcal{H}_0 t/\hbar}\rho'(t)e^{i\mathcal{H}_0 t/\hbar}. \tag{2.37}$$

*These assumptions require that we omit the effect of the microwave field. Fortunately, adding that term is not difficult and does not significantly change the results.[38]

Inserting this into the Liouville-von Neumann equation (2.35) gives

$$\frac{i}{\hbar}[\rho,\mathcal{H}_0]+\exp\left[\frac{-i\mathcal{H}_0 t}{\hbar}\right]\frac{\partial\rho'}{\partial t}\exp\left[\frac{i\mathcal{H}_0 t}{\hbar}\right]=\frac{i}{\hbar}[\rho,\mathcal{H}], \tag{2.38}$$

from which it follows that

$$\frac{\partial\rho'}{\partial t}=\frac{i}{\hbar}[\rho',\mathcal{H}_1^{'}], \tag{2.39}$$

where $\mathcal{H}_1^{'}$ is the interaction-picture time-dependent Hamiltonian:

$$\mathcal{H}_1^{'}=\exp\left[\frac{i\mathcal{H}_0 t}{\hbar}\right]\mathcal{H}_1\exp\left[-\frac{i\mathcal{H}_0 t}{\hbar}\right]. \tag{2.40}$$

This is the equation that must be solved in order to determine the evolution of the density matrix and thus acquire an expression for magnetization via (2.34). Doing so would give an expression similar to the Bloch equations for magnetization, which would directly link the interaction terms in the effective Hamiltonian (2.11) to relaxation times. In other words, this expression will allow us to move from the individual coupling terms in the spin Hamiltonian to bulk, observable quantities in a typical EPR experiment. The relevance given to specific terms in the spin Hamiltonian will determine how accurate the Bloch equations (or similar equations) are in predicting experimental curves. In organic semiconductors, the best theoretical approach to solve this equation depends on the fluctuation rate of the perturbing fields. Three regimes are normally considered: fast fluctuations, slow fluctuations, and no fluctuations. They are considered in turn in the following sections.

2.3.1 Fast fluctuations: the Redfield regime

Integration of (2.39) gives

$$\rho'(t)=\rho'(0)+\frac{i}{\hbar}\int_0^t\left[\rho'(t'),\mathcal{H}_1^{'}(t')\right]dt'. \tag{2.41}$$

This cannot be integrated since the integrand requires knowledge of $\rho'(t)$, which is the quantity for which we are trying to solve. An approximation will have to do, such as by replacing $\rho'(t')$ with $\rho'(0)$. To get a better approximation, we can insert the resulting expression for $\rho'(t)$ into the original equation's integrand. To second order in $\mathcal{H}_1$, this is

$$\begin{aligned}\rho'(t)=&\rho'(0)+\frac{i}{\hbar}\int_0^t\left[\rho'(0),\mathcal{H}_1^{'}(t')\right]dt'\\&+\left(\frac{i}{\hbar}\right)^2\int_0^t\int_0^{t'}\left[\left[\rho'(0),\mathcal{H}_1^{'}(t'')\right],\mathcal{H}_1^{'}(t')\right]dt'dt'',\end{aligned} \tag{2.42}$$

which has

$$\frac{d\rho'}{dt} = \frac{i}{\hbar}\left[\rho'(0), \dot{\mathcal{H}_1'}(t)\right] + \left(\frac{i}{\hbar}\right)^2 \int_0^t \left[\left[\rho'(0), \dot{\mathcal{H}_1'}(t')\right], \dot{\mathcal{H}_1'}(t)\right] dt'. \tag{2.43}$$

as its time evolution. By virtue of our assumption that the average variance of the field across the ensemble vanishes ($\overline{\mathcal{H}_1'(t)} = 0$), the first term on the right-hand side equates to zero.

To progress, we must make one further assumption: that correlations between the field at different points in time vanish after some characteristic timescale. This is of course the same timescale that characterizes fluctuations in the field, τ_c. This assumption allows us to extend the upper limit of integration in the second term on the right-hand side to infinity. Then, it gives terms of the form

$$\frac{1}{\hbar^2}\int_0^t \overline{\langle n|\mathcal{H}'(t-\tau)|m\rangle \langle m'|\mathcal{H}'(t)|n'\rangle} \exp\left[-\frac{i(E_n - E_m)\tau}{\hbar}\right] \exp\left[\frac{i(E_n - E_m + E_{m'} - E_{n'})t}{\hbar}\right] d\tau, \tag{2.44}$$

where $\tau \equiv t - t'$.

The overlined expression in this integral is known as the *correlation function*:

$$G_{nmn'm'}(\tau) = \overline{\langle n|\mathcal{H}_1(t)|m\rangle \langle m'|\mathcal{H}_1(t+\tau)|n'\rangle}. \tag{2.45}$$

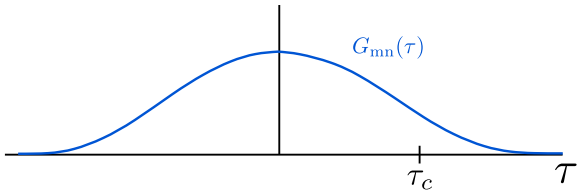

Fig. 2.7 A sketch of a typical correlation function. For times far greater or early than the critical timescale τ_c, the perturbed Hamiltonian is uncorrelated with itself. Reproduced from Slichter (1963).[38]

Written in this way (with the four states n, m, n', and m'), it describes the average correlation of the Hamiltonian with itself at different points and between different eigenstates.* However, by matching indices it can be used to evaluate the time-correlation of $\mathcal{H}'$ between exactly two eigenstates (by setting $m = m'$ and $n = n'$ with $n \neq m$) or for just one state (by setting all indices equal to each other). In general and on average, this correlation should be independent of time at large time scales and should vanish once τ exceeds some critical value τ_c. A sketch of a generic correlation function between two states n and m is shown in Figure 2.7.

Noting the similarity to (2.44), we define the Fourier transform of the correlation function as the *spectral density*:

$$J_{nn'mm'}(\omega) = \int_{-\infty}^{\infty} G_{nn'mm'}(\tau) e^{-i\omega\tau} d\tau \tag{2.46}$$

Elements of the spectral density matrix provide the transition probability between the states m and n:[38]

$$W_{nm} = \frac{J_{nm}(n-m)}{\hbar^2} \tag{2.47}$$

*This form is typically only used in large summations to compute cross-state transition probabilities.

To understand the relevance of this, we note that the spectral density elements are the Fourier transform of the elements of the correlation matrix. Due to this relation, the area under the spectral density curve is fixed even as the correlation time τ_c changes. (This is depicted in Figure 2.8.) As a result, the correlation element J_{nm} corresponding to the frequency ω_{nm} is maximized for a single, specific value of τ_c. By the transition probability (2.47), this then means that the evolution of the states of a system becomes heavily dependent on the correlation time.

With the spectral density defined, integration of (2.43) yields

$$\frac{\mathrm{d}\rho'_{nn'}}{\mathrm{d}t} = \sum_{m,m'} R_{nn'mm'} \exp\left[\frac{i(E_n - E_{n'} - E_m + E_{m'})t}{\hbar}\right] \rho'_{mm'}(0), \tag{2.48}$$

where

$$\begin{aligned} R_{nn'mm'} =& \frac{1}{2\hbar^2}\big[J_{nmn'm'}(n'-m') + J_{nmn'm'}(n-m) \\ &- \delta_{n'm'}\sum_k J_{kmkn}(k-m) - \delta_{nm}\sum_k J_{kn'km'}(k-m')\big]. \end{aligned} \tag{2.49}$$

This is in fact the first term of a power-series expansion of the density matrix elements. By making an assumption of non-correlation between the perturbing Hamiltonian and itself at timescales greater than τ_c, yet still integrating to infinity, we have related the evolution of the density matrix at time t to itself at $t = 0$ only for timescales greater than the correlation time of the field, τ_c. In other words, we can calculate $\mathrm{d}\rho'(t)/\mathrm{d}t$ from $\rho'(0)$ as long as $t > \tau_\mathrm{c}$.

In order for the above expression to converge, $\rho'_{nn'}(t)$ must not be too different from its initial $t = 0$ value. Consequently, there are timescales for which $t > \tau$, yet $\rho'_{nn'}(t) \approx \rho'_{nn'}(0)$. This implies

$$\frac{1}{R_{nn'mm'}} \gg t \gg \tau_\mathrm{c}, \tag{2.50}$$

which then allows us to replace the instances of $\rho'_{mm'}(0)$ with $\rho'_{mm'}(t)$. We then find

$$\frac{\mathrm{d}\rho'_{nn'}}{\mathrm{d}t} = \sum_{m,m'} R_{nn'mm'} \exp\left[\frac{i(E_n - E_{n'} - E_m + E_{m'})t}{\hbar}\right] \rho'_{mm'}, \tag{2.51}$$

which is Redfield's equation* for the components of the density matrix. It is valid so long as the density matrix does not change too much over the timescale of fluctuations and that we only are interested in times greater than this characteristic timescale.

With this expression for density matrix, we can calculate $\mathrm{d}\overline{\langle \mathbf{M} \rangle}/\mathrm{d}t$ from (2.34). All that remains is to choose a form of the perturbing Hamiltonian, which will manifest in the density matrix through $R_{nn'mm'}$ via the spectral densities. For most cases of interest, it takes the form of a spin operator coupled

*Technically, the Redfield equation without a bath contribution. One can be added derived rigorously, but we will simply add its presence as a relaxation term later since the physical mechanisms of the bath are not of interest here.

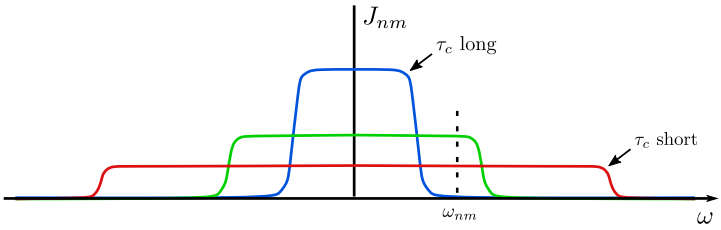

Fig. 2.8 A sketch of a typical spectral density function for three different values of τ_c. By the transition probability (2.47), the transition between n and m (with corresponding frequency difference ω_{nm} is most probable for medium-length correlation times. Reproduced from Slichter (1963).[38]

to a magnetic field:

$$\mathcal{H}_1 = -\sum_q \mathcal{B}_q(t)\mathcal{S}_q. \tag{2.52}$$

Two examples of this are (1) the Zeeman effect due to inhomogeneities in the external, static field and (2) hyperfine interactions with a distribution of different nuclei.

This Hamiltonian gives spectral density terms such as

$$\frac{1}{2\hbar^2}J_{nmn'm'}(\omega) = \frac{\gamma^2}{2}\sum_{q,q'}\langle S_q\rangle_{nm}\langle S'_q\rangle_{m'n'}k_{q,q'}(\omega), \tag{2.53}$$

where

$$k_{qq'}(\omega) \equiv \frac{1}{2}\int_{\infty}^{\infty}\overline{\mathcal{B}_q(t)\mathcal{B}_{q'}(t+\tau)}e^{-i\omega\tau}\mathrm{d}\tau \tag{2.54}$$

has been introduced for simplicity.

We then find for the z-component of $\mathrm{d}\overline{\langle\mathbf{M}\rangle}/\mathrm{d}t$

$$\frac{\mathrm{d}}{\mathrm{d}t}\langle S_z\rangle = \gamma_B\{\langle\mathbf{S}\rangle\times\mathbf{B}\}_z - \gamma_B^2[k_{zz}(\omega_L)+k_{yy}(\omega_L)]\left(\langle S_z\rangle - S_z^{(0)}\right), \tag{2.55}$$

where the equilibrium magnetization $S_z^{(0)}$ has been added to ensure coupling to a bath.

The x- and y-components follow similarly, but decay toward zero:

$$\frac{\mathrm{d}}{\mathrm{d}t}\langle S_{x,y}\rangle = \gamma_B\{\langle\mathbf{S}\rangle\times\mathbf{B}\}_{x,y} - \gamma_B^2[k_{yy,xx}(\omega_L)+k_{zz}(0)]\langle S_{x,y}\rangle - S_0. \tag{2.56}$$

Identifying

$$T_1^{-1} = \gamma_B^2[k_{zz}(\omega_L)+k_{yy}(\omega_L)] \qquad T_2^{-1} = \gamma_B^2[k_{yy}(\omega_L)+k_{zz}(\omega_L)], \tag{2.57}$$

these are the Bloch equations. Specifically, they are the Bloch equations for an ensemble of spins evolving in the presence of a varying Hamiltonian of the form $\mathcal{H}_1(t) = \sum_q \mathcal{B}_q(t)\mathcal{S}_q$, i.e., relaxation due

to variance in explicit fields. The consideration of other forms of $\mathcal{H}_1$ would yield different expressions for T_1 and T_2 in terms of the coupling parameters in the spin Hamiltonian (2.11). The effect of the dipolar coupling between electrons is considered in Chapter 7.

More descriptive forms of the relaxation times can by found by assuming a certain form of the field autocorrelation $\overline{B_q(t)B_q(t+\tau)}$. Specifically, if it decays exponentially with time, i.e., $\overline{B_q(t)B_q(t+\tau)} = \overline{B_q^2}\exp[-|\tau|/\tau_c]$,* then the relaxation times are given by

$$\frac{1}{T_1} = \gamma_{\mathcal{B}}^2\left(\overline{\mathcal{B}_x^2}+\overline{\mathcal{B}_y^2}\right)\frac{\tau_c}{1+\omega_L^2\tau_c^2} \qquad \frac{1}{T_2} = \frac{1}{2T_1}+\gamma_{\mathcal{B}}^2\overline{\mathcal{B}_z^2}\tau_c. \tag{2.58}$$

The quantities $\overline{\mathcal{B}_q^2}$ are, of course, simply the mean-square variance of the amplitude of the fluctuations theorized at the beginning of this section: $\overline{\mathcal{B}_q^2} = \mathcal{B}_{\text{rms}}^2$, while τ_c is the characteristic frequency at which the fields fluctuate. From the reference frame of a single spin, this can be due to external forces, such as increased nuclear activity changing local nuclear magnetic moments, or internal forces, such as a moving spin changing its environment. In organic semiconductors for temperature below 200 K, τ_c often has the same temperature dependence as mobility.[15] Thus, it is interpreted as the inverse of the average hopping frequency of a charge, ν.

These results are readily interpreted: T_1 corresponds to a change in the z-magnetization, which occurs from spins flipping along this direction. Only fields in the transverse directions, x and y, can produce these flips, meaning only these components of the perturbing field contribution to this relaxation. Moreover, while all fluctuations contribute to T_1 decay by some amount, fluctuation frequencies that match the Larmor frequency will be most effective at driving relaxation. Figure 2.9 shows the behavior of T_1 and T_2 as the autocorrelation time (normalized by the Larmor period) changes; a minimum occurs when $\tau_c = \tau_L$. This is a manifestation of the simple fact that spin flipping induced by transverse fields is most probable at frequencies matching the Larmor frequency, just as in EPR experiments.

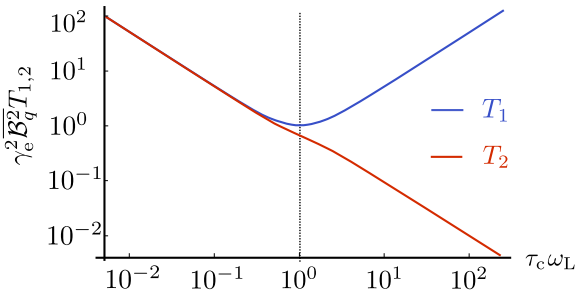

Fig. 2.9 A sketch of the transverse and longitudinal relaxation times as a function of the correlation time (normalized against the period of the Larmor frequency). T_1 is minimized when the two timescales are equal. T_2 decreases as the correlation time increases. Adapted from Slichter (1963).[38]

Meanwhile, dephasing in the transverse direction can be caused by (1) changes in the local Larmor frequencies (which occur via z-oriented fields) or (2) spin flips (which are again effected by transverse fields), though each spin flip has only a 50% chance of dephasing an individual spin. Separating these

*There is no *a priori* reason this form is expected for local field fluctuations. However, it can be justified by noting that (1) many random decay processes are described by exponential curves and (2) it yields the Bloch equations. One sometimes wonders how many brilliant insights were first justified by, 'Well, it gives us the right answer!'.

two contributions gives

$$\frac{1}{T_2'} = \frac{1}{T_2} - \frac{1}{2T_1} = \gamma_e^2 \mathcal{B}_{\text{rms}}^2 \tau_c, \tag{2.59}$$

which is the pure dephasing component of T_2 (i.e., excluding spin flips). As the autocorrelation time is lowered (caused by more rapid motion), T_2 increases because each spin moves rapidly enough such that local variations become averaged-out, and each spin experiences the same local environment. This is a manifestation of what was noted earlier in this section: the evolution of the density matrix as described by (2.48) suggests the existence of timescales $t > \tau_c$ over which the density matrix does not change too much from itself. This is known as *motional narrowing* because it results in the narrowing of the resonance signal (see (2.29)). As seen in Figure 2.9, T_2 monotonically decreases with the hopping frequency, a simple consequence of decreased motional narrowing.

Ultimately, because convergence of (2.48) is only possible if the density matrix does not change too much over the time $t > \tau_c$ the Redfield expressions for T_1 ad T_2 are valid only in this regime of motional narrowing. This is also known as the rapid motion regime. It is quantified by the requirement that the fluctuation rate of the field be far greater than the average rate at which dephasing occurs. Since dephasing corresponds to an acquisition of a phase due to the Larmor frequency of the local field ($\delta\omega = \gamma_e \delta\mathcal{B}_{\text{rms}}$), this requirement is $\delta\omega \ll \omega_c$, or $\tau_c \delta\omega \ll 1$.

2.3.2 Slow fluctuations; no fluctuations

As motion slows, motional narrowing is no longer effective enough to ensure $\rho'_{nn'}(t) \approx \rho'_{nn'}(0)$ and therefore the Redfield expressions derived above are invalid. To analyze this regime, we instead consider two spins initially in-phase. The time over which the spins remain coherent depends upon two factors. The first of these is the average time that must elapse before local fields fluctuate; this is simply τ_c. The second is the average time it takes for the Larmor phase acquired by the new fields (after fluctuation has occurred) to decohere the spins. Because multiple fluctuations can occur before decoherence is complete, the total Larmor phase (and thus timescale) acquired must be the sum of that of every precession event before decoherence. On average, this is the average precession time multiplied by the number of fluctuations before decoherence: $t_{\text{pre}}(1 + t_{\text{pre}}/\tau_c)$.

Noting that $1/t_{\text{pre}} = \omega = \gamma_e \mathcal{B}_{\text{rms}}$, this gives for the decoherence time

$$T_2' = \tau_c + \frac{1}{\gamma_e \mathcal{B}_{\text{rms}}} \left(1 + \frac{1}{\gamma_e \mathcal{B}_{\text{rms}} \tau_c} \right). \tag{2.60}$$

In the limit of extremely slow fluctuations, τ_c becomes large and the first term dominates. This results in long decoherence times, which is sensible for systems in which local fluctuations vary slowly in time. In the ultimate limit of frozen motion, both τ_c and T_2' become infinite, indicating spins do not decohere. This occurs because spins cannot experience different local fields.

As the fluctuation rate increases, τ_c becomes small and the final term of (2.60) dominates, eventually converging to the Redfield expression (2.59).

CHAPTER 3

FIELD-INDUCED ELECTRON SPIN RESONANCE

ESR is a powerful spectroscopic tool not only because it allows for the unique determination of species in a sample (via the g-factor), but also because it allows us to measure the strengths of nuclear, electronic, spin-orbit, dipolar, exchange, and other coupling mechanisms. Of particular interest for this report are the relaxation times: by relating the characteristic timescale of relaxation we will show how ESR can be used to probe charge and spin dynamics.

The main drawback of ESR is that the sample must exhibit a magnetic response.* Thus, to study electron dynamics, it is desirable to choose a system in which the strength of the magnetic response can be tuned. Organic field-effect transistors are ideally suited for the job: the number of injected charges (and thus the number of unpaired electrons) scales with the applied gate voltage. The study of electron dynamics via field-effect transistors is known as field-induced electron spin resonance (FIESR).

3.1 Organic Field-Effect Transistors

In field-effect transistors, the source-drain current is modulated by a voltage applied to a third electrode: the gate. This is achieved by placing an electric insulator and a semiconductor between the gate and the source-drain electrodes. The role of the gate in OFETs is to *accumulate* charge carriers rather than to deplete them: a positive (negative) gate voltage will inject negative (positive) charge carriers from the electrodes; applying a source-drain voltage will then allow these carriers to flow. A schematic of this is shown in Figure 3.1.

The dielectric serves to prevent current from flowing directly between the gate and source/drain while also enhancing the effectiveness of the gate voltage; in this way, it acts as a capacitor. If no drain voltage is applied† then the simple relation

$$q_m = \mathcal{C} V_{\mathrm{g}}$$

*Well, to be exact, a non-diamagnetic response.

†For simplicity, we always assume the source electrode to be grounded.

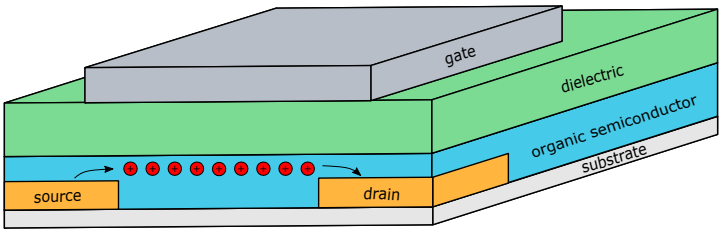

Fig. 3.1 The working principle of an organic field-effect transistor. When a voltage is applied to the gate, the magnetic polarization induced in the dielectric draws electrons from the electrodes and accumulates them at the dielectric-semiconductor interface. These polarons are the charge carriers in the device. In this architecture, the device is known as *top-gate, bottom-contact*.

should relate the number of mobile charge carriers per unit area, the capacitance per unit area of the dielectric, and the gate voltage. In reality, imperfections in the semiconductor will lead to trap states, reducing the overall number of free charges. These traps act by reducing the applied electric field felt by the accumulated charges. If the gate voltage does not exceed this minimum, no charges can flow. Therefore, there is a *threshold voltage* that reduces the actual voltage felt by the electrons. This means V_{g} is actually replaced by $V_{\mathrm{eff}} = V_{\mathrm{g}} - V_{\mathrm{th}}$ in the above capacitance relation:

$$q_m = \mathcal{C}(V_{\mathrm{g}} - V_{\mathrm{th}}). \tag{3.1}$$

Once a drain voltage is applied, there is not a constant voltage differential across the channel. The charge carrier area density is now a function of position in the channel:

$$q_m(x) = \mathcal{C}(V_{\mathrm{g}} - V_{\mathrm{th}} - V(x)), \tag{3.2}$$

where $V(x)$ is the potential at location x due to the source/drain electrodes. It vanishes at the source, $x = 0$, and is maximized at the drain, $V(L) = V_{\mathrm{d}}$.

Ohm's law can be used to relate the charge carrier concentration to the device current so long as the channel length is at least 10 times longer than the dielectric thickness.* This is known as the *gradual channel approximation*. Using it, we have

$$\begin{aligned} I =& W q_m \mu \frac{\mathrm{d}V}{\mathrm{d}x} \\ =& W \mathcal{C}(V_{\mathrm{g}} - V_{\mathrm{th}} - V(x)) \mu \frac{\mathrm{d}V}{\mathrm{d}x}, \end{aligned} \tag{3.3}$$

where W is the channel width and μ is the charge carrier mobility. Integrating this equation gives

$$I = \frac{W}{L} \mu \mathcal{C} \left[(V_{\mathrm{g}} - V_{\mathrm{th}}) V_{\mathrm{d}} - \frac{1}{2} V_{\mathrm{d}}^2 \right]. \tag{3.4}$$

*Since we fabricate the devices, this condition is always satisfied in this report.

When the gate voltage far exceeds the drain voltage, i.e., $V_g \gg V_d$, the last term can be dropped and we have

$$I_{lin} = \frac{W}{L}\mu_{lin}\mathcal{C}(V_g - V_{th})V_d \qquad \mu_{lin} = \frac{\partial I_{lin}}{\partial V_g}\frac{L}{W\mathcal{C}V_d} \tag{3.5}$$

for the current and mobility. The device is said to operate in the *linear regime* since the current increases linearly with the drain voltage. As V_d becomes comparable to and eventually exceeds V_g, however, the number of accumulated carriers drops since the drain acts as a sink for them. Charges are no longer accumulated across the channel, but are instead *pinched-off* at some point. The transistor is said to be *saturated* since the current no longer scales with the drain voltage. In this regime, the drain voltage must be replaced by the voltage at the pinch-off point. This gives

$$I_{sat} = \frac{W}{2L}\mu_{sat}\mathcal{C}(V_g - V_{th})^2 \qquad \mu_{sat} = \left(\frac{\partial\sqrt{I_{sat}}}{\partial V_g}\right)^2\frac{2L}{W\mathcal{C}} \tag{3.6}$$

as the current and mobility in the saturation regime. A depiction of the carrier concentration in the channel as a function of potential difference is depicted in Figure 3.2.

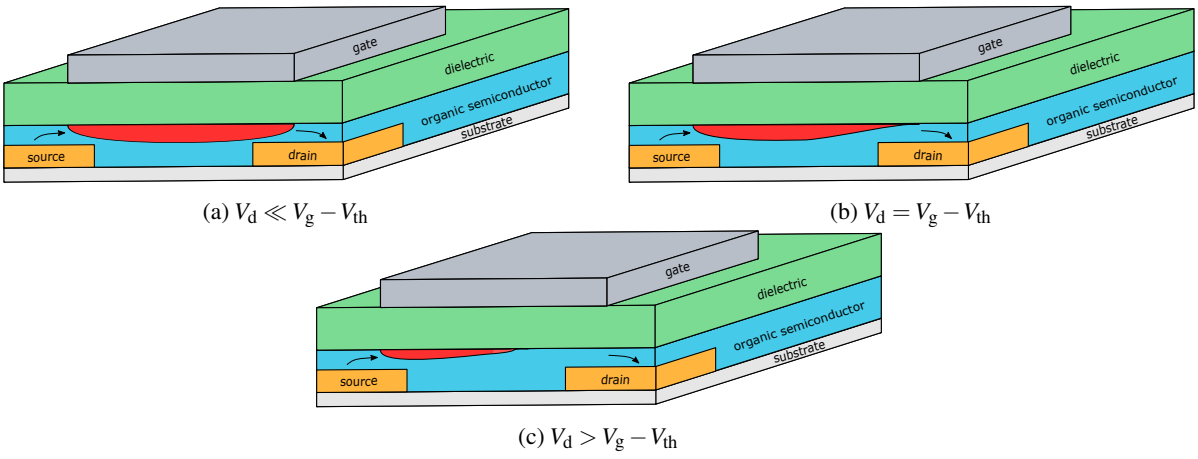

(a) $V_d \ll V_g - V_{th}$

(b) $V_d = V_g - V_{th}$

(c) $V_d > V_g - V_{th}$

Fig. 3.2 The evolution of the carrier concentration in the channel as the drain voltage moves from $|V_d| \ll |V_g - V_{th}|$ to $|V_d| \gg |V_g - V_{th}|$. As V_d increases, the charge density in the channel decreases since the effective gate potential is lowered.

There are two common methods by which to characterize transistor performance. The first, known as an *output measurement*, plots the device current as a function of drain voltage; this allows one to distinguish between the linear and saturation regimes (since, according to equations (3.5) and (3.6), only the current in the linear regime will show a dependence on the drain voltage). The second, known as a *transfer measurement*, plots the device current as a function of gate voltage. Such a measurement is normally taken twice: once with the drain voltage low enough for the device to operate linearly, and once with it high enough for the device to operate in saturation. This allows for an easy determination of

the device threshold voltage and on-off ratio (of the drain current). The mobility can also be extracted using the slope of the plot.

3.2 Field-Induced Electron Spin Resonance

Because FETs allow one to modulate the number of free charge carriers in the device, they make an excellent choice for the study of electron dynamics using ESR spectroscopy. Figure 3.3 shows the basic premise of a field-induced electron spin resonance experiment: (a) Without a gate voltage applied to the FET, the polymer is in its neutral state; no free charges exist to resonate. (b) After a voltage is applied, polarons accumulate in the HOMO.* (c) The Zeeman field is then switched on, causing the two states of the orbital to become non-degenerate. (d) Finally, the free electron is able to resonate upon excitation from the microwave field.

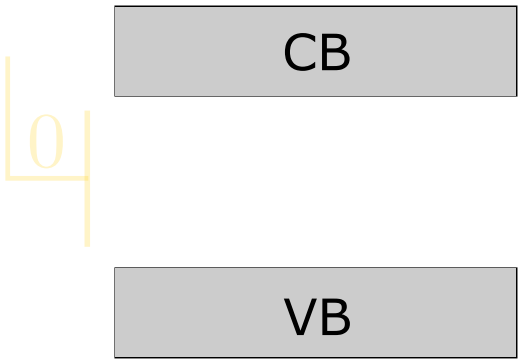

(a) The conduction and valence bands of the neutral polymer.

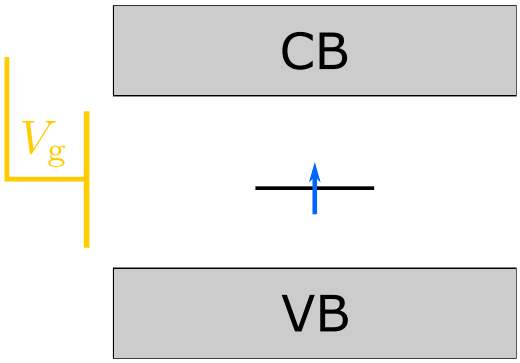

(b) After a bias voltage is applied, charges accumulate in the HOMO.

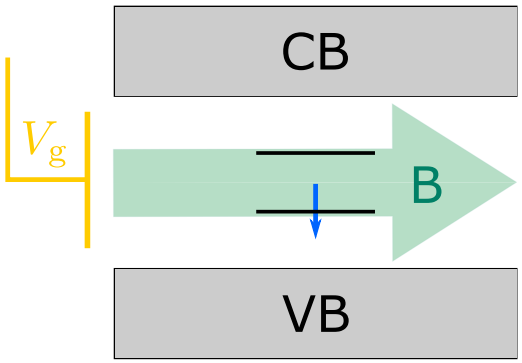

(c) The degeneracy of the HOMO is lifted upon activation of the Zeeman field.

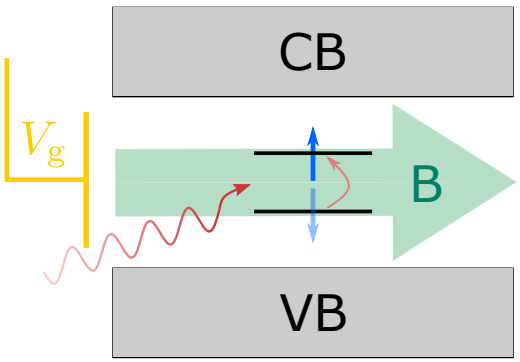

(d) The injected charges are able to resonate between the non-degenerate states via microwave radiation.

Fig. 3.3 A schematic depicting how OFETs can be used in an ESR experiment, i.e., FI-ESR.

*If one injections holes, then the neutral HOMO goes from being doubly occupied to singularly occupied. If electrons are injected, the neutral LUMO becomes a singularly occupied HOMO.

3.2.1 Detection of polarons and bipolarons

In organic semiconductors, a missing or additional electron on a molecule causes a rearrangement of the surrounding nuclei, and this distortion propagates as the charge moves through the system. The combination of the charge and the distortion is known as a positive (in the case of a missing electron) or negative (in the case of an additional electron) *polaron*. Though the jump from an induced radical on a molecule to a polaron is straightforward to make, it is important to remember that a polaron carries a specific *polaron binding energy* with it.[12] In FI-ESR, the charges accumulated in the field-effect transistor become polarons when the device is switched on.*

Marumoto et al. (2006) were the first to demonstrate the utility of FI-ESR in organic FETs.[25] In pentacene FETs, they showed that the number of carriers detected by EPR is equal to and follows the same dependence on V_g as those calculated via capacitance measurements, thus showing that FI-ESR indeed measures all injected polarons. Next, they presented resonance spectra for the device aligned parallel and perpendicular to the Zeeman field, showing different g-factors and peak-to-peak linewidths between the two. By comparing their results to diffraction data, they showed that these differences are attributable to anisotropy in the g-tensor and the averaging between its different components that occurs depending on the angle between the molecule and the Zeeman field. This demonstrated the ability of FI-ESR to corroborate estimated values of the the molecular g-tensor and, by extension, the packing arrangement of a molecule. Finally, they extracted the average delocalization length of an electron in the device via the parallel and perpendicular peak-to-peak linewidths, which in turn supported then-recent calculations of a larger delocalization length than previously estimated.

The simple correlation between number of injection carriers and intensity of the ESR signal has led to a diverse range of conclusions. Marumoto et al. (2007) measured composite regioregular poly(3-hexylthiophene) (RR-P3HT) and C_{60} metal-insulator-semiconductors (MIS) diodes using FI-ESR, monitoring the resonance position and width as a function of gate voltage.[26] They found a clear signal at $g \approx 2.002$ whose intensity grew with negative gate voltage, and at $g \approx 1.998$ whose intensity grew with positive gate voltage. Based on the device structure, they were able to unambiguously show that positive charge carriers were injected into the RR-P3HT while negative carriers were injected into the C_{60}. Tanaka et al. (2009), meanwhile, used FI-ESR to provide additional evidence for the gradual-channel approximation of OFETs.[41] In RR-P3HT FETs, they observed an increase of the ESR signal with increasing gate voltage and zero drain voltage, a linear decrease of the signal upon application of small drain voltages, and finally a drain-voltage-independent signal as V_d became comparable to V_g. This observation matches the carrier concentration vs. V_{sd} behavior predicted by the gradual-channel approximation, which reads as

$$Q = \left[\frac{1}{2}V_{ds} - (V_{gs} - V_{th})\right] LW\mathcal{C}, \tag{3.7}$$

*Since the molecular rearrangement occurs as soon as charges are injected, some may say that polarons are induced directly rather than electrons or holes that soon become polarons. For the purposes in this thesis, the difference isn't relevant.

in the linear regime and as

$$Q = -\frac{1}{2}(V_{gs} - V_{th})LW\mathcal{C} \tag{3.8}$$

in the saturation regime (where $V_{ds} = V_{gs} - V_{th}$). They expanded upon this work later,[42] noting that charge transport dominated by variable-range hopping[43] should have a power-law dependence on the effective gate voltage, i.e., $\mu \sim V_{eff}^{\beta-2}$. They showed that the EPR-extracted carrier concentration agreed well with this dependence using a value of 2.6 in pentacene FETs and 2.3 in P3HT devices.

Perhaps unintuitive at first, Kuroda et al. (2009) showed the ESR can also be used to detect the formation of spinless bipolarons in FETs.[22] Monitoring the carrier concentration as a function of V_g in RR-P3HT MIS diodes, they observed that the carrier concentration increases linearly with voltage until approximately -15 V, where it begins to saturate. They attribute this behavior to the formation of bipolarons, which begins to occur at a spin concentration of about 0.2%. Their pentacene diodes, however, showed no such deviation despite reaching similar spin concentrations. This showed the bipolaron formation is a system-dependent process that differs between polymers and small-molecules. In fact, comparison between different derivatives of P3HT showed that it is the molecular backbone — not the side-chain — that sets the saturation point.

3.2.2 Motional narrowing

Motional narrowing* is another area of interest when using FI-ESR. The first experimental evidence of polaron motional narrowing in organic semiconductors was found by Matsui et al. in 2003.[44†] They measured pentacene thin-film transistors (TFTs) and monitored the evolution of the resonance signal with both gate voltage and temperature. They found that direct correspondence between the field-effect mobility and linewidth; specifically, higher mobilities resulted in narrower lines. Using Redfield theory, they estimated the average time a polaron spent in a trap state to be approximately 1 ns, far longer than polarons in band transport (see (2.59)). From this, they were also able to estimate the average hopping distance in pentacene (10 nm) using the Einstein relation for diffusive transport,

$$\mu = q\frac{\overline{R}^2\nu}{k_B T}. \tag{3.9}$$

(It is important to emphasize that this equation is being used to estimate the hopping frequency of a spin-carrying charge, not a pure spin. The reason this distinction is necessary is because disagreement exists regarding whether the diffusivity constant in the Einstein relation is the same as the diffusivity constant used in calculations of the spin diffusion length of a system. For a more thorough discussion, see the supplementary information of Schott et al.'s (2019) recent work on polaron spin dynamics.[15])

*The theory of motional narrowing is explained in detail in Subsection 2.3.1.

†Actually, this was the first experimental evidence of polaron motional narrowing in *any* field-effect devices, not just organics.

3.2.3 Trap states; intra- and inter-domain transport

Leveraging the microscopic insight that FI-ESR gives, Kawamura et al. (2017)[45] measured the resonance signal of P3HT and PBTTT* FETs down to 4 K. Observed was that both the peak-to-peak linewidths and mobilities obey an Arrhenius curve with temperature, but with different activation energies: in both cases that of the bulk mobility was 10 times larger than that of B_{pp}. Because the peak-to-peak linewidth is a measure of charge hopping frequency (see Subsection 2.3.1) — primarily an intra-domain event — this showed that the barrier to transport within domains is significantly smaller than that between domains. In other words, bulk device mobility is limited primarily by the time charges spend moving between polymer domains. Interestingly, the intra-domain mobility in these amorphous systems was found to be near that of semicrystalline systems.

Building upon this work, Matsui and Hasegawa (2009) compared the temperature dependence of linewidths between high- and low-mobility pentacene TFTs.[24]. They observed a saturation value of 200 μT in the peak-to-peak linewidth, which corresponds to an activation energy of about 10 meV. Because this saturation occurred for both devices, it is clear that the distribution of intra-grain trap states is roughly equivalent in pentacene films; the major effect on bulk mobility comes from deep trap states that are formed at inter-grain boundaries.

A more detailed insight into the distribution of trap states came from Matsui, Mishchenko, and Hasegawa (2010) when they investigated the ESR spectra of pentacene TFTs at temperatures below 50 K.[46] Here, the spectra are Gaussian due to all accumulated charges being frozen in their local environments. If one assumes an energetic distribution of trap states, then each electron falls into one level in the distribution. The collection of all electrons at a single level contributes one Gaussian to the overall signal. Matsui et al. showed that, following this argument, their spectra could each be decomposed into three significant contributions, i.e., they identified three major groups of trap states. The first and second are characterized by wavefunctions spanning only 1.5 and 5 molecules, and have binding energies of 140 and 22 meV. The third is much broader, spanning 6-20 molecules and having a binding energy between five and 15 meV. Further, because this final set of states lies lower than the others in energy, we may conclude that these are the 'shallow' traps that are filled quickly during device operation.

One means by which to improve device performance is to passivate these trap states. Marumoto et al. (2011) systematically characterized the linewidth of FETs made with single crystals of rubrene (RSC-FET) with and without application of a self-assembled monolayer (SAM).[47] By extracting autocorrelation times, they found that trap residency time decreases from 700 to 60 ps when a SAM is placed at the semiconductor-dielectric interface. Not only does this correspond to an increase in mobility (from 0.72 to 7.68 cm^2/Vs), but also shows that the most inhibitive traps toward charge transport are located at the device interface — an observation bolstered by the fact that the g-factor (and thus molecular crystallinity) of the material did not change with SAM treatment.

*The initialism PBTTT is obvious once you learn that the full chemical name is poly(2,5-bis(3-hexadecylthiophene-2-yl)thieno[3,2- b]thiophene).

3.2.4 Material microstructure

As was mentioned in the previous chapter, the g-tensor is directly related to molecular microstructure via coupling to angular momentum. Watanabe et al. (2011)[48] used this by measuring P3HT/PCBM blends in MIS diodes. For pure P3HT devices, they found that the p-type polaron (the hole) has a resonance position of $g = 2.0031$, corresponding to an edge-on orientation of the holes along the lamellar structure. As PCBM was added, however, they saw a second peak emerge at $g = 2.0022$, indicating flat-on localization. Not only did this peak grow with increasing PCBM in the blend, but the device mobility fell by three orders of magnitude. Such a steep decrease is attributable to the pπ-orbitals that constitute the flat-on orientation because they interrupt the two-dimensional charge transport between edge-on π orbitals.

Tanaka et al. (2019)[49] measured two diketopyrrolo-pyrrole-based devices (DPP-based) to link their microstructure to their charge transport properties. By measuring at 4 K — where inter-domain transport does not occur — they were able to measure intra-domain mobility and extract the corresponding activation energy. They found it to be as low as 10 meV; not only far lower than that of inter-domain transport, but even lower than that of intra-domain transport in other semicrystalline systems. Based on ESR measurements supplemented with DFT calculations, they ascribed this value to the high molecular planarity of the molecules. They further noted that this rigid structure allows for nearly identical transport between and within domains, as the effects of motional narrowing in the two regimes were found to be identical.

CHAPTER 4

EXPERIMENTAL ANALYSIS & CONSIDERATIONS

While the lineshape (2.29) describes the form of the absorption function, it does not properly describe the spectrum $\mathcal{S}$ recorded by the spectrometer. This is because there are several instrumental factors that alter both the magnitude and linewidth of the signal. In order to properly extract physical values and meaning from fitted parameters, it is crucial to understand the origins of these contributions as well as how to properly analyze them. That is the goal of this chapter.

As a simple example, (2.30) showed that absorption will be maximized at the resonance $\gamma B = \omega_{\mathrm{L}}$. One therefore requires precise recordings of B to properly determine the g-factor. In the experimental ESR setup used for this report, the Zeeman field is measured by an NMR teslameter sitting several centimeters away from the sample. The corresponding offset in magnetic field is easily corrected by measuring a sample with a known g-factor, finding the resonance, and calculating the difference between resonant field and teslameter-recorded field.

4.1 Experimental Setup

All EPR measurements reported in this thesis were taken on a Bruker E500 spectrometer using a Bruker ER 4122SHQE cavity and an X-band microwave source. An Oxford Instruments ESR900 cryostat controlled by an Oxford Instruments Mercury iTC was used for temperature-dependent spectra, and a Keithley 2602b source unit was used for electrical characterization. CustomXepr, a Python package developed by Sam Schott,[15] was used to integrate the above-mentioned instruments and automate measurements when desired.

A typical FI-ESR substrate is a 40 mm x 3 mm x 0.5 mm fused quartz plate (UQG optics, FQP-5005) with an organic field-effect transistor fabricated on top. The bottom of the sample is adhered to a sample holder/boat using Kapton tape or silver conductive paint. The end of the boat nearest the sample consists of three contact pads, which are contacted to the OFET pads via wire-bonding. These contact pads extend to the other end of the boat, where they are soldered to conductive wires. The other ends of these wires are threaded through a rubber vacuum cap for an EPR tube, and the resulting small holes around the wires in the cap are re-sealed with epoxy. The entire system of sample, boat, wires, and thread (henceforth known as the "substrate") is then loaded into an EPR tube and sealed using the vacuum cap.

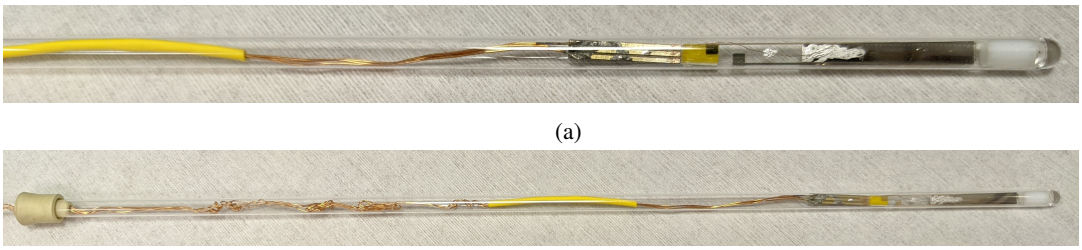

(a)

(b)

Fig. 4.1 **(a)** A single transistor attached to the sample boat. On the sample are visible the gold source and drain electrodes as well as the aluminium gate. The transistor electrodes are connected to the boat with aluminium wire bonds, and the sample itself is adhered with double-sided Kapton tape. The large amount of silver dag paint on the gate is to prevent the aluminium wire from disconnecting under thermal stress. **(b)** The full sample tube with substrate inside it. The wires leading from the sample to the rubber cap are clearly visible.

This leaves the ends of the wires out of the EPR tube, allowing us to connect them to the Keithley source unit.

The spectrometer setup is displayed in Figure 4.2. Sample tubes are slid into tube holders, which are positioned such that the bottom of the tube stands in the center of the microwave cavity and between the coils that produce the static, constant Zeeman field. This fixes the orientation of the excitation microwaves relative to the Zeeman field, meaning all measurements are considered perpendicular-mode EPR. The smaller coils on top of those that produce the Zeeman field produce the small modulation that allows for first-harmonic detection of the signal. A signal is detected by fixing the frequency of the microwave source and slowly sweeping the Zeeman field.

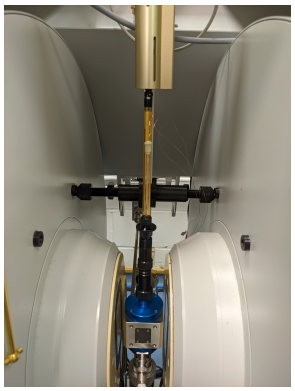

Fig. 4.2 A picture of a sample tube inside the EPR cavity. The large white cylinders on either side are the electromagnets that produce the Zeeman field, while the smaller cylinders on top of them produce the modulation field. The metallic blue holder is the Oxford cryostat.

4.2 The Microwave Path

During operation, microwaves traverse the path represented by the block diagram Figure 4.3. Point A is the source, where a Gunn diode produces microwave excitations. The diode is capable of producing gigahertz radiation up to 200 mW power, a range suitable for the EPR measurements described herein. The majority of microwaves produced at the source travel to point B in the diagram, the attenuator. Here, the power of incoming microwaves is finely tuned to ensure they properly match those desired by the experimenter. From this point, they travel to point C, a circulator, which directs these incoming microwaves to the sample cavity (D). While the exact details of the cavity will be discussed shortly, here it is sufficient to describe how the radiation interacts with the sample: largely, it doesn't. At least not

until the resonance condition (2.1) is met. When the condition is met, however, the sample becomes much more absorptive as spins are forced to flip. This manifests as a radiation signal emitted from the sample, which travels back into the circuit toward the circulator, and is then directed to a Schottky barrier diode (E). This diode acts as the detection mechanism, sending the voltage generated by the signal radiation to the spectrometer. This diode functions with optimal sensitivity when its current is 200 μA. To ensure this, a small portion of the source microwaves are sent to a reference arm (point F), which adds or subtracts to the signal radiation the microwave power needed to achieve 200 μA. A phase shifter is also located in the reference arm to ensure the phase of the supplemental radiation matches that of the signal.

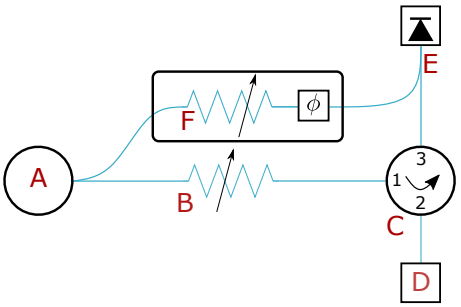

Fig. 4.3 A block diagram of the microwave bridge. Adapted from Jiang (2001).[50]

When operating at optimal sensitivity, the output of the Schottky diode is proportional to the square root of the microwave power. Thus, the signal resulting from the Lorentzian absorption function (2.29) has the slightly altered form

$$\mathcal{L}(B|\omega_{\mathrm{mw}},\rho) = \frac{B_{\mathrm{mw}}\chi_0\gamma B\omega_{\mathrm{mw}}}{\sqrt{1+\gamma^2 B_{\mathrm{mw}}^2 T_1 T_2}}\frac{1}{\pi\rho}\frac{\rho^2}{\rho^2+(\omega_{\mathrm{L}}-\omega_{\mathrm{mw}})^2}, \tag{4.1}$$

which of course slightly alters the Voigtian signal

$$\mathcal{V}(B|\omega_{\mathrm{mw}},B_v,\rho) = \int_{-\infty}^{\infty}\mathcal{G}(B'|B_v)\mathcal{L}(B-B'|\rho)dB'. \tag{4.2}$$

4.3 The Microwave Cavity; Determination of B_{mw}

To understand the influence of the microwave cavity on the signal, it is important to note that ESR samples are measured inside resonant cavities to enhance weak signals. This is possible because an electromagnetic wave at resonance inside a cavity is a standing wave, meaning its electric and magnetic components are entirely out of phase. We can thus place the sample at a position where the oscillating magnetic field is maximized and the oscillating electric field is minimized. The absorption signal, which depends on the magnitude of the magnetic component, is also maximized.

As mentioned, the sample is placed at the center of the cavity and the frequency of the radiation field is tuned until resonance is found. Thus, the microwave source sets both the radiation frequency, ω_{mw}, and the radiation power. However, the amplitude of the radiation field, B_{mw}, is also needed for computation of relaxation times and absolute number of spins. To determine this, we must note that some energy applied to the cavity will always be lost,* which corresponds to a reduction in B_{mw}. The ratio of energy stored in the cavity over one cycle of the radiation field to the energy lost in the same

*One source for loss is the generation of Eddy currents in the cavity walls, while a second is the absorption of microwaves by the sample itself.

cycle is known as the *q-factor*. Here its definition is equivalent to the ratio of the cavity's resonant frequency to the full-width-at-half-height of the resonance, a quantity recorded for each scan:[51]

$$Q = \frac{\omega_{\mathrm{mw}}}{\Delta\omega}. \tag{4.3}$$

The magnetic field amplitude then follows straightforwardly since the integrated absorption signals of paramagnetic materials scale directly with magnetic field amplitude and magnetic susceptibility. Thus, by measuring a known reference,* we find the following relationship between microwave power and amplitude at the center of the cavity as a function of q-factor:

$$B^0_{\mathrm{mw}} \equiv B_{\mathrm{mw}}(y = L/2) = \kappa\sqrt{QP_{\mathrm{mw}}} \qquad \kappa = 2.4069 \times 10^{-6}\ \mathrm{T}/\sqrt{\mathrm{W}}, \tag{4.4}$$

where L is the length of the cavity. Since the sample is only 3 mm wide, we neglect radial fluctuations in B_{mw}. For vertical fluctuations, Bruker software stores this functional form of B_{mw} as a ninth-degree polynomial. Using it, we can calculate the average magnetic field across the length of the sample:

$$B_{\mathrm{mw}}(Q, P_{\mathrm{mw}}) = \frac{1}{L}\int_0^L b(y) B^0_{\mathrm{mw}} \mathrm{d}y. \tag{4.5}$$

4.4 Zeeman Field Modulation

As mentioned at the beginning of this chapter, small modulation coils superimpose a small, oscillating magnetic field on top of the Zeeman field. A lock-in amplifier tuned to the modulation frequency then increases the resonance signal while also filtering out many sources of noise. Consequently, it is not the absorption signal that is recorded by the spectrometer, but rather the derivative of absorption with respect to the static field. Mathematically, this amounts to adding a term $B_{\mathrm{mod}}\sin(\omega_{\mathrm{mod}}t)$ to the Zeeman field B. Upon taking the derivative of this with respect to the modulation frequency, we see that the detected signal scales directly with the amplitude of the modulation field. This technique is therefore advantageous because it increases the signal-to-noise ratio; however, it does require correction for signal artifacts.

Both the peak-to-peak amplitude A_{pp} and linewidth B_{pp} of the derivative signal are functions of the chosen modulation amplitude, as shown in Figure 4.4. As shown in the right panel, in the absence of modulation the peak-to-peak linewidth is equal to the ratio $2\rho/\sqrt{3}$. In the left panel, we see that if the modulation amplitude is smaller than this value, the absorption signal scales almost linearly with B_{mod}. Beyond this point, however, the signal slowly decreases. This suggests setting the modulation amplitude equal to the true linewidth of the sample in the absence of modulation, i.e., $B_{\mathrm{mod}} = \Delta B^0_{\mathrm{pp}}$; yet, even before the decrease in signal amplitude, the observed linewidth $\Delta B_{\mathrm{pp}}(B_{\mathrm{mod}})$ is artificially broadened to an appreciable degree.[36] To preserve the true derivative spectrum, B_{mod} should be chosen so that is a

*For the experiments described here, we use a small amount of the organic 2,2-diphenyl-1-picrylhydrazyl (DPPH), which is a stable free-radical molecule.

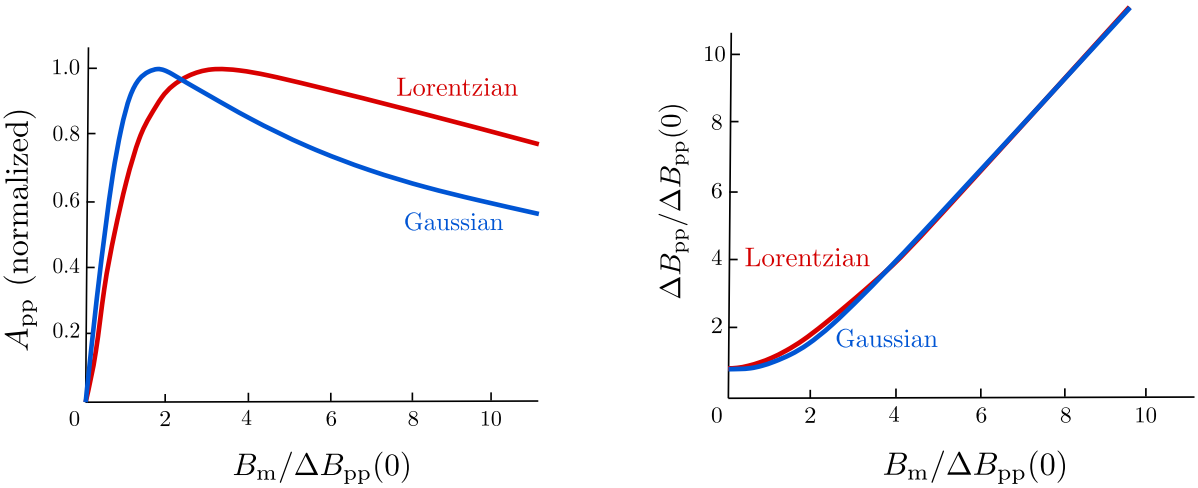

Fig. 4.4 fig: Normalized peak-to-peak amplitude (**left**) and relative linewidth (**right**) for first derivative Lorentzian and Gaussian curves as a function of modulation amplitude. $\Delta B_{pp}(0)$ is the linewidth in the absence of modulation. Reproduced from Slichter (1963).[38]

fraction of ΔB^0_{pp}. This is, unfortunately, not always possible, especially when the sample's absorption is weak. In that case, a large value of B_{mod} is needed and the artificial broadening must be corrected.

A routine in MATLAB to perform this correction is used for the data described herein. By exploiting the facts that the diode's response to the signal (including modulation) can be written as a Fourier transform of the signal, and that phase-sensitive detection has no time variance with the signal, it models the recorded spectrum $\mathcal{S}$ as a convolution between a modulation kernel and the absorption signal. The resultant signal therefore follows the form

$$\mathcal{S}(B|B_{mod},\omega_{mw},\rho) = \int_{-\infty}^{\infty} K_1(B|B_{mod})\mathcal{L}(B-B'|\omega_{mw},\rho)\mathrm{d}B' \tag{4.6}$$

where

$$K_n(B|B_{mod}) = i^n \int_{-\infty}^{\infty} J_n\left(\frac{B_{mod}B^*}{2}\right) e^{iBB^*}\mathrm{d}B^* \tag{4.7}$$

is defined by the nth order Bessel function. The harmonic K_1 is chosen specifically because that is the harmonic detected by the amplifier. If the spectral signal is in the Voigtian regime, this equation is modified to

$$\mathcal{S}(B|B_{mod},\omega_{mw},\rho,B_v) = \int_{-\infty}^{\infty} K_1(B|B_{mod})\mathcal{V}(B-B'|\omega_{mw},\rho,B_v)\mathrm{d}B'. \tag{4.8}$$

The above equations thus account for the modulation field and allow us to extract the true absorption function $\mathcal{L}$ or $\mathcal{V}$.

As long as $B_{mod} \leq \Delta B^0_{pp}$, these expressions are valid. Therefore, it is important when acquiring data to start with a small modulation amplitude and to slowly increase it until artificial broadening is

first observed. For more information regarding the theoretical background see the work by Hyde et al. (1990)[52]

4.5 Parameter Extraction

The true absorption signal that allows us to extract physically meaningful parameters is the Lorentzian

$$\mathcal{L}(B,|\omega_{\mathrm{mw}},\rho) = \frac{B_{\mathrm{mw}}\chi_0\gamma B\omega_{\mathrm{mw}}}{\sqrt{1+\gamma^2 B_{\mathrm{mw}}^2 T_1 T_2}}\frac{1}{\pi\rho}\frac{\rho^2}{\rho^2+(\omega_{\mathrm{L}}-\omega_{\mathrm{mw}})^2}, \tag{4.9}$$

with, in the case of a Voigtian signal, the B_{rms} of the Gaussian distribution of fields. By fitting it, we obtain the resonance position, the product T_1T_2, and B_{rms}. The extracted resonance position from such a fit will be an average of the principal components of $\mathbf{g}$, while averages of the components of $\mathcal{A}$ and $\mathcal{D}$ may be extracted by expressing T_1 and T_2 in terms of the coupling tensors, as described in Section 2.3. Because the lineshapes were derived from the model Hamiltonian (2.11) under the assumption that it is averaged in all directions, a fit to these curves reveals only some average of the principal components of the coupling tensors.

Actual fits were performed for the data herein by using the Levenberg–Marquardt algorithm to perform non-linear least-squares fitting.[53] In more general cases, where spectra cannot be fit to simple Lorentzian, Voigtian, or Gaussian curves, advanced fitting procedures may be used, such as starting with a model Hamiltonian, calculating the resulting energy levels, and determining the electronic transition energies using density functional theory. Though this was not done for this thesis, such a procedure could allow for all components of the coupling tensors to be estimated.

4.5.1 Spin counting

Integration of (4.9) with respect to γB yields

$$\mathscr{A} = \kappa\frac{B_{\mathrm{mw}}\chi_0\gamma B\omega_{\mathrm{mw}}}{\sqrt{1+\gamma^2 B_{\mathrm{mw}}^2 T_1 T_2}}. \tag{4.10}$$

(The factor κ is needed to ensure cavity-dependent calibration factors are included. These values are determined by the manufacturers of the measurement equipment used and are automatically included in all measurements. However, periodic calibrations are performed to ensure they do not drift.) If the power of the oscillating field is weak enough to satisfy $\gamma B_{\mathrm{mw}}^2 T_1 T_2 \ll 1$ then this gives a measure of χ_0 and, by the results of the previous section, the number of free spins N. Further, in this same limit, absorption grows with increasing microwave field strength. Physically this is because the probability per unit time of causing a spin to flip increases with B_{mw}: higher microwave powers cause more spins to absorb and more spins to radiate energy per unit time. As long as there remains a population imbalance, there will be a greater net absorption.[36] The effect of increasing the microwave field to higher powers (where the condition $\gamma B_{\mathrm{mw}}^2 T_1 T_2 \ll 1$ is no longer satisfied) is discussed in the following section.

Though Lorentzian and Gaussian curves can easily be identified by their lineshapes, it is important to not 'clip the wings' of these curves, i.e., to ensure recorded spectra capture even the outermost points of the curves. The reason for this is shown in Figure 4.5, where the percent error in the extracted number of spins is plotted as a function of the width of the spectrum, measured in number of peak-to-peak linewidths (S). For Lorentzian curves, we see that even a spectrum of width 20 peak-to-peak linewidths can result in almost 10% error in spin estimation, and more accurate values can only be obtained by going to very large acquisition ranges (30+ peak-to-peak linewidths). Gaussians, due to their narrower lineshape, permit small error estimates for spectra of only five peak-to-peak linewidth, but dropping below this value drastically increases error.

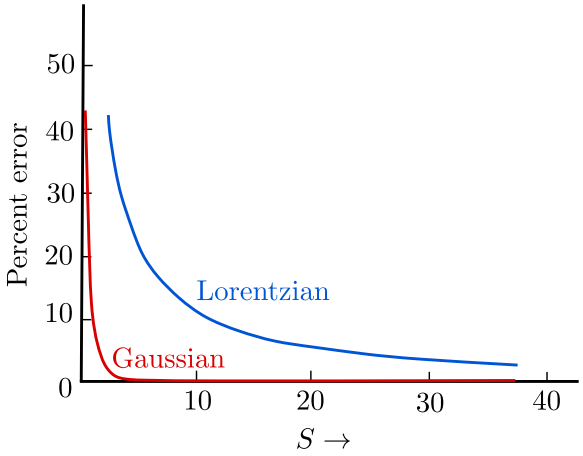

Fig. 4.5 The percent error obtained in spin counting when the first-derivative spectrum is truncated. S is the range of the spectrum measured in number of B_{pp}. Reproduced from Weil & Bolton (2007).[36]

4.5.2 Saturation vs. non-saturation measurements

As $\gamma B_{mw}^2 T_1 T_2$ becomes comparable to and exceeds unity, we see from (4.9) that the signal will begin to decrease. This occurs because the microwave field pushes the states toward equal populations: if more spins exist in one state than the other, there are also more spins leaving that state because the probabilities of the two transitions are equal. To remain unevenly populated, the higher-energy spins must have time to thermally relax by exchanging energy with the lattice. If they cannot then the field will drive the states toward equal populations, resulting in decreasing net absorption and eventually no signal whatsoever. This regime is known as the *saturation* regime.[34]

A second effect of saturation is an increase in the width of the signal, $\rho \equiv \sqrt{1+\gamma^2 B_{mw}^2 T_1 T_2}/\gamma T_2$. This is due to an increase (from faster spin-flipping) of the magnetic fields produced by dipoles throughout the sample. Different electrons experience different local variations and thus different effective magnetic fields. The result is a wider distribution of resonant frequencies. This is one example of linewidth broadening.

If a measurement is taken while the system is not saturated, the condition $\gamma^2 B_{mw}^2 T_1 T_2 \ll 1$ implies that one can only acquire g and T_2 from a fit. Physically this means that the speed with which the system relaxes hot spins (T_1^{-1}) is faster than the rate of excitation and measurement. On the other hand, driving the system to saturation allows one to obtain the product $T_1 T_2$. To find this saturation point, we *could* fit the peak-to-peak height of the signal as a function of microwave power, $H_{pp}(P_1)$ to a square-root dependence (see Section 2.2). However, an altogether more accurate measurement of relaxation times can be obtained by recording the spectrum $\mathcal{S}(B)$ over a range of microwave field powers and then fitting

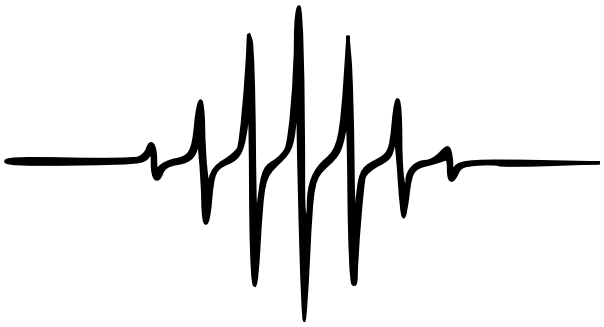

Fig. 4.6 A simulated EPR spectrum for one unpaired electron interacting with eight equivalent $I = 1/2$ nuclei. As additional nuclei are added, eigenstates become more and more degenerate. This is reflected in the relative intensities of the peaks observed. Reproduced from Weil & Bolton (2007).[36]

the full 2D dependence, $\mathcal{S}(B, B_{\mathrm{mw}})$. This yields the values T_1 and T_2 (as well as other parameters already mentioned).

It is worth mentioning that power saturation measurements are not challenging conceptually, but impose considerable time costs: Because T_1 is best fit by having a large range and high resolution of microwave powers, a four-minute scan for a single spectrum can translate to between one and two hours for a saturation measurement. This, coupled with temperature-dependent measurements, the need to increase integration times and numbers of scans, and the desire to repeat measurements to avoid random errors, can result in a single experiment taking three, four, or even five weeks (especially in the case of ambipolar measurements, where both polaron types are measured; see Chapter 5).

4.5.3 Resolution of hyperfine signals

If individual hyperfine signals can be resolved then the individual hyperfine couplings $\boldsymbol{\mathcal{A}}^n$ can be determined by the splittings in the signal. If they cannot be resolved (because the splittings are smaller than the linewidth of the Lorentzian), the signal is inhomogeneously broadened and resembles a Gaussian. It is only possible then to obtain the average coupling constant, $\overline{a}$. The half-width-at-half-maximum of the Gaussian is related to this mean coupling strength via

$$\Delta B_{1/2} = \frac{\overline{a}}{\sqrt{\mathcal{N}}}, \tag{4.11}$$

for an electron whose wavefunction spreads over $\mathcal{N}$ nuclei.[36] (See Subsection 2.1.2 for a discussion of why the linewidth narrows with delocalization of the electron.)

4.5.4 Error analysis

As described previously, the Levenberg–Marquardt algorithm is used in this thesis to perform non-linear least-squares fitting of Lorentzian and Voigtian curves to the data. As a result, errors of parameter estimates are obtained from the fitting procedure. The only significant source of experimental error comes from the exact placement of the sample inside the cavity due to the non-uniformity of the magnetic

field (see Section 4.3). To minimize this, all EPR samples were prepared such that the center of the FET accumulation layer would sit in the center of the microwave cavity when the sample sat at the bottom of the sample tube, and the sample tube at the bottom of the cavity. Thus, while it's possible that this alignment results in samples sitting slightly higher or lower than the exact center of the cavity, such error would be systematic and would only alter (slightly) the overall values of reported parameters; comparisons and trends as a function of temperature and applied voltage would still be valid.

4.6 Other Experimental Considerations

This section will review experimental parameters that do not directly affect parameter extraction, but do impact the shape of the spectral signal and are necessary to accurately obtain the data presented in this thesis.

4.6.1 Sample temperature

Sample temperature can affect both spectral intensity and linewidth. If the system is described by Boltzmann statistics, then the spectral intensity is modified via a change in the population of spin states with temperature. As stated in Subsection 2.1.3, this occurs in paramagnetic samples and the susceptibility in this case is Curie. Because this is an inverse law with temperature, spectra taken at the lowest temperature feasible are often those with the greatest signal-to-noise ratio. However, care must be taken when measuring at low temperatures, as experimental difficulties may arise. A few examples are that q-values can drop as moisture condenses in a cavity that may not be perfectly sealed from the atmosphere, charges may not be able to accumulate in FETs used for FI-ESR, and thermal heating at high microwave powers may be damaging to organic samples.

The spin-lattice relaxation time T_1 can have a strong dependence on temperature via its dependence on the fluctuations of local fields.* In such cases, the spectral linewidth is a strong function of sample temperature. It is thus sometimes necessary to measure at low temperatures to ensure sufficiently narrow linewidths (or, at the opposite extreme, measure at higher temperatures so that the linewidth is detectable for a given spectrometer).

4.6.2 Modulation frequency

Though rarely encountered as a problem, occasionally the modulation frequency applied to the field superimposed on the Zeeman field can distort the spectral line observed.[36] In general, as the modulation frequency approaches the linewidth (i.e., $\nu_{\text{mod}} \sim (g\mu_B/h)\Delta B_{\text{pp}}$), side-bands begin to appear in the spectral signal, and the intensity of these bands scales with the modulation amplitude. (See Figure 4.7 for an example of the development of these sidebands with increasing modulation amplitude.) Thus, even in cases where the lower limit of modulation is still too high for the given linewidth, it is still best to reduce the modulation amplitude as far as possible. This prevents the observed sidebands from

*In extreme cases, the relaxation time is inversely proportional to the seventh power of temperature.[54]

significantly distorting the spectrum, and such artifacts may be removed or rectified in post-processing. The situation of having a very narrow linewidth is encountered in Chapter 7, where we must lower both the modulation frequency and amplitude to observe the true spectral signal.

Fig. 4.7 The appearance of modulation sidebands in CaO as a result of over-modulating the signal. The true linewidth is 2.0 μT, while the modulation amplitude is, from left to right, 0.4, 2.0, and 5.0 μT. The modulation frequency is 100 KHz. Reproduced from Weil & Bolton (2007).[36]

Chapter 5

Spin Relaxation in Ambipolar Polymer OFETs

Ambipolar devices are those able to produce both electron and hole currents. For field-effect transistors, this definition requires that both electrons and holes can be injected into the channel. In theory, any organic semiconductor may be used to construct an ambipolar device by matching the work function of one electrode to the semiconductor's LUMO while matching the work function of the other to the HOMO. In practice, it is customary to refer to a material as 'ambipolar' if it can be used to produce an ambipolar device without using different metals for the source and drain contacts. These systems are preferable from a fabrication standpoint, but the resulting mismatch between the work function and either the LUMO or the HOMO will cause one type of polaron to produce an injection-limited current.* Nevertheless, several ambipolar materials offer well-balanced and high polaron mobilities with minimal device processing, making them desirable systems in which to compare polaron-dependent processes.

5.1 Introduction

Though ambipolar OFETs only came of notice in the early 2000s,[55–57] research into them has grown steadily over the past two decades.† Their advantage over inorganics is clearly demonstrated by two technologies: (1) the complementary inverter, where organics can offer simpler fabrication procedures (compared to inorganics, which often require fabrication via submicrometer-implantation of dopants), and (2) light-emitting field-effect transistors (since light emission in bulk silicon is inhibited by the indirect band gap).[58] In either case, these devices offer the low-cost, large-scale, flexible manufacturing afforded by organics combined with the multipurpose applicability of ambipolar systems.

At the advent of ambipolar OFETs, devices featuring π-conjugated conducting polymers composite with fullerene were desirable due their ease of solution processing.[55,59,60] Though it was long suspected that positive carriers in these systems were injected into the polymer and negative into the fullerene, the first definitive proof came from Marumoto et al. (2009) when they used FI-ESR to identify unique

*An *injection-limited current* is one in which the current flowing through a device is limited by the efficiency of the electrodes to inject charges. It should be compared to a *space-charge-limited current*, where the current is limited by the ability of the dielectric to transport injected charges.[12]

†As recorded by published articles counted by the Institute for Scientific Information Web of Science. Data updated from Zaumseil and Sirringhaus (2007).[58]

g-values in the positive and negative bias regimes.[26] Watanabe et al. (2009) then added to this work, ascribing unique ambipolar charge transport in similar devices.[61] Beyond this, FI-ESR has been used to estimate the spatial extent of polaron wavefunctions,[25,46] observe polaronic motional narrowing,[44,22,24,62] and study trapping mechanisms in OFETs.[24,46,47]

Recently, our group used FI-ESR to systematically study polaron spin dynamics in several high-mobility organic semiconductors.[15] By performing power-saturation measurements from 5 K to room temperature (see Subsection 4.5.2), we observed three regimes of spin relaxation. The first two, *inhomogeneous broadening* and *motional narrowing*, are predicted from the theory presented in Subsection 2.3.1, while the third requires an alternative explanation. By excluding inter-chain effects and simulating intra-chain dynamics of the polaronic wavefunction on picosecond timescales, we proposed a *spin-shuttling* model of relaxation in this regime, whereby reconfigurations of the wavefunction in response to nuclear vibrations cause spins to relax.

Here, we measure ambipolar systems in FI-ESR to systematically study relaxation dynamics as a function of temperature. These materials are useful because they allow for variation in the electronic wavefunction (via injection of either p- or n-type polarons) without changing the microstructure of the material. In other words, we are able to probe relaxation theories directly as a function of the wavefunction, without the need to compare across systems and account for structural and electronic differences. As an added benefit, the time required for simulations to compare against our results is reduced since many structural parameters remain the same for both polaron types.

This strategy (of comparing polarons in ambipolar systems) reveals here that polaron mobility remains an important factor in relaxation at all temperatures. We observe that, in transitioning from inhomogeneous broadening to motional narrowing regime, mobility is far more important than the extent of the wavefunction, and only in the high-temperature regime does the localization length of the wavefunction become significant. We hypothesize in that regime that, if relaxation is driven by wavefunction reconfiguration due to nuclear vibrations, then altering the wavefunction but retaining the same nuclear modes should manifest as different relaxation behavior. Thus, systems with similar radical cation and anion wavefunctions should display little difference between the relaxation behavior of polarons in the spin-shuttling regime, while spatially different radical wavefunctions should display more contrasting behavior.

5.2 Experimental Design

5.2.1 Systems measured

We consider three representative systems here, the chemical structures of which are shown in Figure 5.1. The first two — an anthracene-naphthalene derivative (AN) and a naphthalene-naphthalene derivative (NN) — are electron-deficient, conjugated polymers with completely fused backbone structures not containing any single-bond linkages;[63] both have been previously characterized by Xiao et al. (2021).[64*]

*In Xiao et al.'s work, note that AN is referred to as AN2 and NN as NN1.

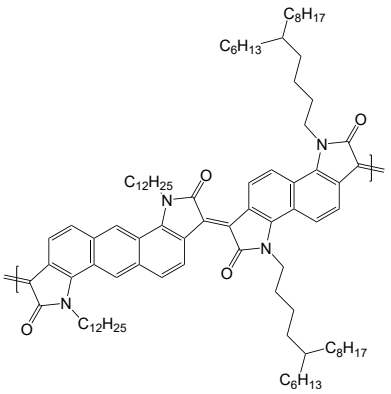

(a) AN

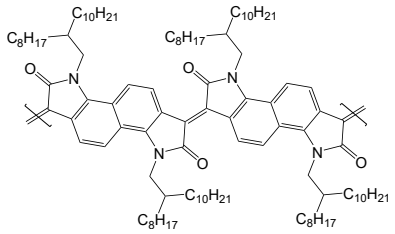

(b) NN

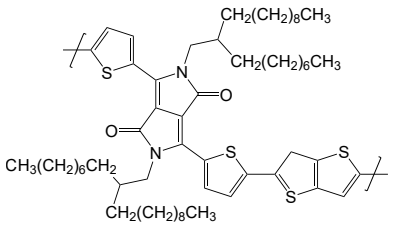

(c) DPPT-TT

Fig. 5.1 The ambipolar organic semiconductors used for this research. AN and NN are fused copolymers while DPPT-TT is a donor-acceptor system. See Xiao et al. (2021)[64] for characterization of the fused systems, and Chen et al. (2012)[65] for that of DPPT-TT.

In these systems, the double bond fusing the backbone results in an extremely rigid structure and rod-like conformation. Due to the high degree of symmetry across the bonding site in these systems, we hypothesize their electron and hole wavefunctions to be similar to one another.*† Though the structures are rigid, they are not completely flat due to steric repulsion between carbonyl oxygens and adjacent C-H groups, which results in both systems having a torsion angle of roughly 18° at the double bond. Though ambipolar transport was demonstrated for these polymers, only the electron regime was systematically studied due to injection issues for holes. In AN, electron mobility ranged from 0.4 to 0.8 cm^2/Vs (depending on molecular weight), while in NN the highest mobility achieved was 0.1 cm^2/Vs for high molecular weights, and was drastically lower for smaller molecular weights.

The third system — a diketopyrrolopyrrole derivative (DPPT-TT)[66] — is a donor-acceptor system, meaning a single molecule can be clearly divided into an electron-rich and electron-deficient moiety.[67] It is comprised of DPP, thieno[3,2-b]thiophene (TT), and a two thiophene moities in a single repeat unit. Though first identified as a hole-transport system, Chen et al. (2012)[65] demonstrated it as capable of ambipolar transport under optimized device fabrication. In particular, high annealing temperatures (> 200° C) improved the edge-on‡ packing of the system and thus facilitated charge transport in both holes and electrons, while solely electron transport was improved by even higher annealing temperatures

*To be clear, the polaron wavefunctions are similar to one another in AN, while the same is true in NN. They need not be similar across the two systems.

†Simulations of the polaron wavefunctions are currently in progress, but were not yet complete at the time of writing.

‡The system packed along the π-π direction in-plane and along the side-chain out-of-plane.

(320° C) and not plasma-cleaning gold contacts before spin-coating.* Via these fabrication methods, mobilities on the order of 1 cm^2/Vs were achieved for both polaron types.

In this chapter we show that the three regimes of spin relaxation are present for both types of polarons in all three systems. By relating charge transport measurements to FI-ESR spectra, we show that organic spin dynamics are driven primarily by charge motion at temperatures below roughly 150 K, independent of wavefunction localization. For higher temperatures, we show that wavefunction extent becomes the dominating factor, with spin-shuttling driven by nuclear torsion relaxing spins faster than charge transport can counteract this effect. We compare these observations to simulations on DPPT-TT, which show a clear difference in the localization of holes and electrons. We use this to identify in a DPPT-TT chain the exact site of torsion responsible for spin-shuttling, and we compare these results to those of the fused systems, where the similarity of the wavefunctions manifests as similar relaxation behavior.

5.2.2 Methods

Field-induced ESR measurements were performed on top-gate, bottom-contact FET devices: Fused-quartz plates (UQG Optics, FQP-5005) were cut to 40 mm x 40 mm squares with a diamond saw, then ridges of depth 0.3 mm were cut into one side of the glass along its full length at the 3 mm mark, 4.5 mm mark, 7.5 mm mark, 9 mm mark, etc. After cleaning, we used photolithography followed by metal evaporation to deposit interdigitated source and drain contacts with a total channel width and length of 243 mm and 0.1 mm, respectively. The odd layout of the electrodes is due to the narrow constraints of the ESR cavity coupled with the need for high carrier injection in order to detect a signal. A photograph of the contacts in a test device is shown in Figure 4.1.

Solutions of AN and NN were created by adding 10 g/l of polymer to trichlorobenzene and dissolving for 1 hour at 160° C. We heated the substrates at 150° C for five minutes, then spin-coated the solutions onto them at 1200 rpm for 6 minutes using hot glass pipettes (also heated at 150° C for five minutes). Immediately afterward we annealed the devices by placing them on a hot plate at 160° C for 5 minutes, then 250° for 30 minutes, then quenching them on the metal surface of the glovebox.

The solution of DPPT-TT was created by adding 10 g/l of material to dichlorobenzene and dissolving overnight at 80° C. Solutions were spin-coated at 1400 rpm for 60 seconds. Devices were then annealed at 320° C for 20 minutes, then quenched.

After polymer deposition, all devices had PMMA spin-coated onto them at 1400 rpm for 30 seconds, then were annealed at 80° C for 30 minutes. This method results in a PMMA layer that is 400 nm thick and has a dielectric constant of 3.6. PMMA is known to be suitable for ambipolar transport in polymer FETs because it has few electron-trapping groups.[58,68–70]

We finished fabrication by evaporating aluminium gates of thickness 30 nm over the active areas. Individual devices were separated from the 4 cm x 4 cm square by applying pressure along the length of

*Several possible explanations were suggested for the improvement in electron transport upon annealing, while the improvement from not plasma cleaning was attributed to a reduction of the electrode's work function.

the 0.3 mm indents. In some cases, it was helpful to first cut through the dielectric and polymer over the grooves using a scalpel. This prevented the dielectric from peeling off the gate upon device separation.

To perform FI-ESR measurements, a transistor was attached and wire-bonded to a substrate holder with source, drain, and gate connections. The device-and-boat combination was lowered into a tube appropriate for ESR measurements and sealed under nitrogen using a rubber cap. The electrode wires were punctured through the cap in order to connect to the voltage source, and the puncture sites were sealed with epoxy to preserve vacuum. (See Section 4.1 for more details of this setup.)

All EPR measurements were taken on a Bruker E500 spectrometer using a Bruker ER 4122SHQE cavity and an X-band microwave source. An Oxford Instruments ESR900 cryostat controlled by an Oxford Instruments Mercury iTC was used for temperature-dependent spectra, and a Keithley 2602b source unit was used for electrical characterization. CustomXepr, a Python package developed by Sam Schott,[15] was used to integrate data collected by these instruments and to automate measurements when desired.

5.2.3 Experimenter contributions

The author of this thesis proposed the original idea to study ambipolar systems as a test of wavefunction dynamics, fabricated the samples, recorded nearly all of the data, and analyzed the results. Sam Schott helped fine-tune the experimental design, assisted in collecting data when necessary, and provided useful input on data analysis. Mingfei Xiao provided training on the fabrication of AN and NN. David Beljonne and Vincent Lemaur did all of the computational work presented in Subsection 5.3.3. Henning Sirringhaus, of course, provided much useful insight in the experimental design and in the interpretation of the data.

5.3 Results & Analyses

5.3.1 Device characterization

To ensure sufficient balance between both polaron mobilities, we first performed electrical measurements to characterize the OFETs. Figure 5.2 shows the n- and p-type transfer curves and corresponding mobilities in all three systems at 290 K. In the top row, we see that n-type transfer performance in the fused systems is nearly ideal while p-type shows a higher threshold voltage and more ill-defined turn-on. In DPPT-TT, performance is nearly identical for both holes and electrons, each having nearly the same threshold voltage and turn-on. The bottom row of the figure shows the polaron mobilities in the three systems. In AN at 290 K, both electron and hole mobility are on the order of 0.1 cm^2/Vs, which can be compared to Xiao et al.'s reported value of 0.4-0.8 cm^2/Vs in electrons. (Mobilities for holes were not reported.) In NN, both polaron mobilities were about 0.01 cm^2/Vs, which is the expected value for electron mobility in NN.[64] In DPPT-TT, our observed mobilities were lower than those reported in Chen's work:[65] 0.1 vs. 1 cm^2/Vs for both holes and electrons. Though our values are lower than those under entirely optimized conditions, we emphasize that the ambipolar behavior is well balanced, thus

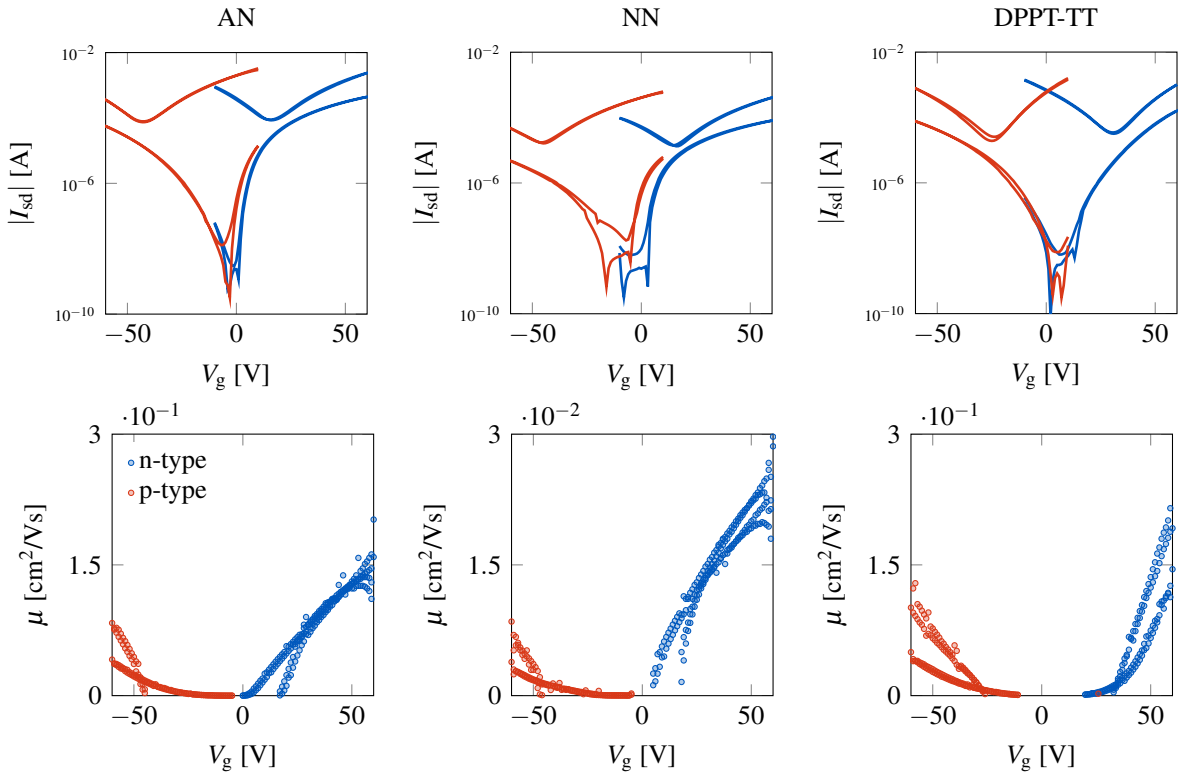

Fig. 5.2 Ambipolar transfer (**top row**) and mobility (**bottom row**) characteristics of AN, NN, and DPPT-TT at 290 K in both the linear and saturation regimes. Red corresponds to holes and blue to electrons. For clarity, mobilities before the turn-on voltage are not shown.

making the two polaron types comparable in our FI-ESR measurements. In all systems, n-type mobility is 2-3 times higher than p-type (at the same magnitude of gate voltage).

Relaxation times were recorded via the following procedure: At a given temperature we first measured the p-type spectra ($V_g = -60$ V), then measured the background signal ($V_g = 0$ V) if deemed necessary from initial test scans, then measured the n-type spectra ($V_g = 60$ V). Transfer and output curves were recorded before and after each ESR measurement to ensure device degradation was negligible over the scanning time. In order to avoid systematic error in ESR curves due to this p-type, background, then n-type ordering, we occasionally and randomly measured n-type data first or measured n-type performance in another device to compare. No differences were observed.

For AN and DPPT-TT at temperatures below 80 K, hole injection was so low that an ESR signal was not obtainable. (The minimum number of spins required is 10^{11}.) To overcome this, we recorded those spectra by injecting polarons at 150 K and then lowering the temperature to the required value to measure.* Consequently, FET curves are not available for these low temperatures, as recording these

*Since only holes presented this problem, it would have been possible to continue injecting electrons at each temperature step. However, because this research aims to compare the relaxation behavior of holes and electrons under otherwise equal conditions, we decided it would be best to keep measurement conditions the same between the two polaron types at each temperature.

would have emptied the accumulation layer of injected polarons. The problem occurred for NN below 120 K, so polarons in those scans were injected at 200 K.

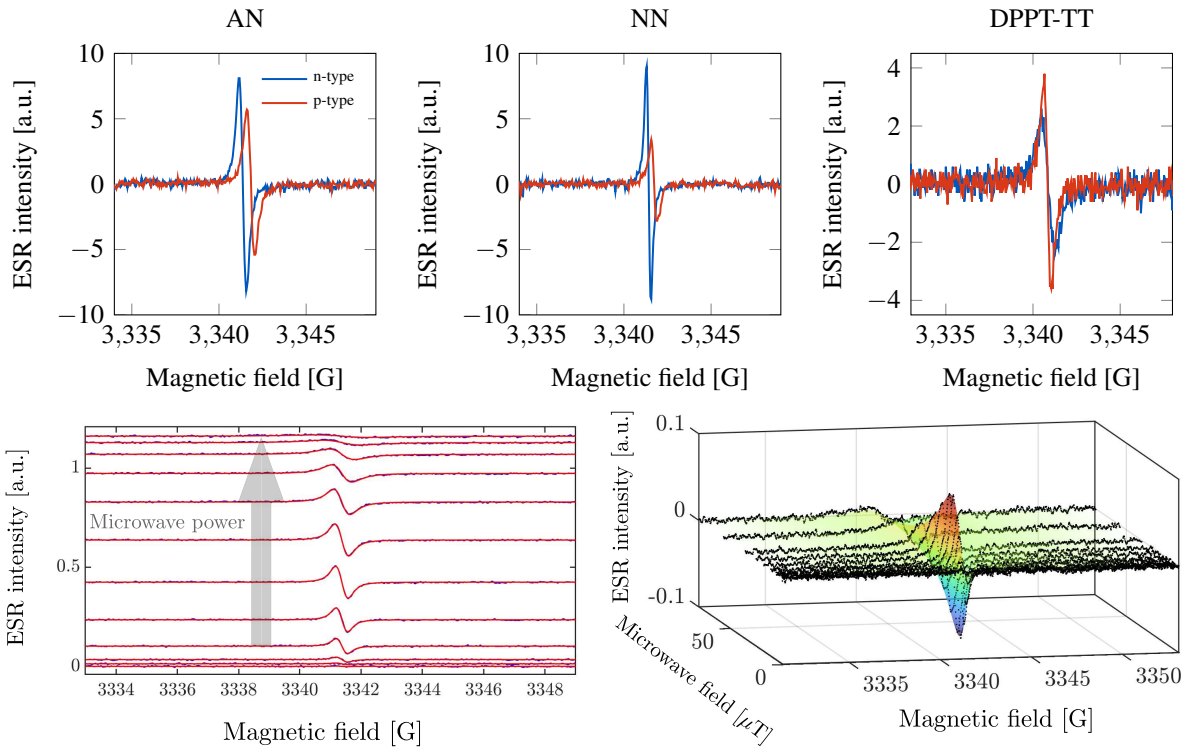

Fig. 5.3 **Top row:** Representative ESR spectra for holes and electrons in AN, NN, and DPPT-TT at 200 K. **Bottom left:** Stacked plots of the n-type spectra in AN at 200 K as a function of microwave power. **Bottom right:** The same data presented as a surface plot with the full 2D fit.

5.3.2 Relaxation dynamics

To extract relaxation times, power-saturation curves were recorded at each temperature step. (See Subsection 4.5.2 for the theory of these measurements.) Representative ESR spectra are shown for each system at 200 K in the top row of Figure 5.3. For all three systems, unique electron and hole signals were observed for positive and negative voltages, respectively. The resonance positions of these signals for electrons and holes, respectively, (and each with error ± 0.00005) are 2.00367 and 2.00335 in AN, 2.00367 and 2.00340 in NN, and 2.00385 and 2.00385 in DPPT-TT. It is important to note that these curves are only meant to show a typical signal for each sample. Relative spectra locations and size are not comparable since these are determined by measurement parameters, which may be modified between scans. In the bottom row on the left is a stacked plot depicting the evolution of the electron polaron in AN at 200 K as a function of microwave power; the black dots are individual data points while the red lines are fits. On the right is the same data depicted in a surface plot along with the full 2D fit.

The full temperature dependencies of both longitudinal and transverse relaxation times can be found in the top row of Figure 5.4. In accordance with Schott et al.'s work (2019),[15] the inhomogeneous

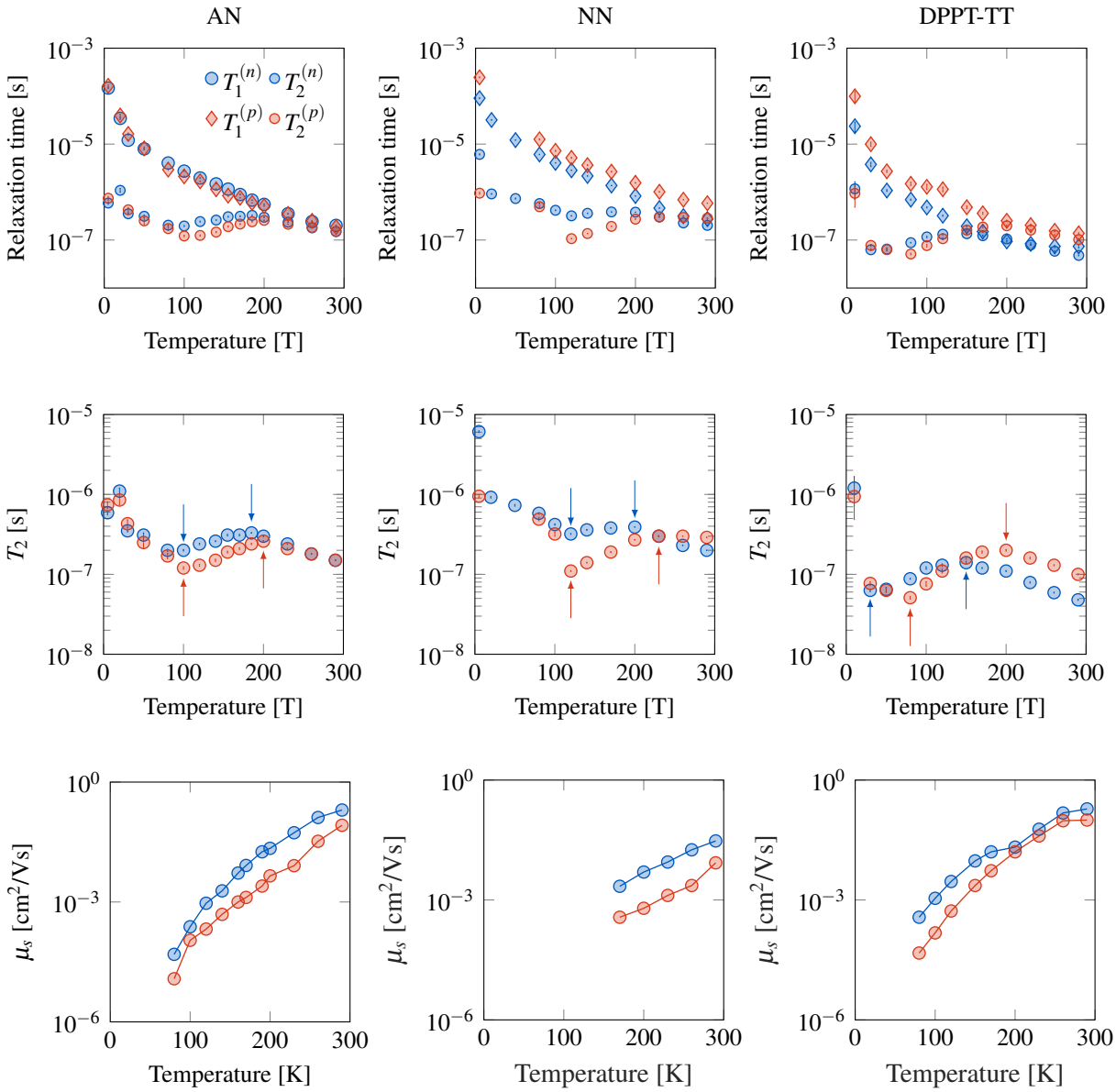

Fig. 5.4 **Top row:** Dependence of polaron mobility as a function of temperature in the three systems studied. **Middle row:** Dependence of only polaron T_2 on temperature. The red and blue dashed lines mark a transition in relaxation regime for holes and electrons, respectively. The first (per plot) marks the transition from inhomogeneous broadening to motional narrowing, and the second from motional narrowing to high-temperature relaxation. The T_2 data for AN and NN has previously been published.[64] **Bottom row:** Dependence of polaron mobility on temperature across the three different materials.

broadening, motional narrowing, and spin-shuttling regimes of relaxation are clearly visible in all three systems for both polaron types.* Because T_1 monotonically decreases with increasing temperature, only the behavior of T_2 in these systems differentiates between the relaxation regimes. We therefore show

*Also in accordance with Schott et al.'s work, and with Subsection 4.5.2, each T_1 and T_2 data point took roughly five hours to collect, meaning full plots were the result of weeks' worth of effort (after including test scans, repeats, and failures).

only T_2 vs. temperature in the center row of Figure 5.4. In the three figures, the different regimes are delineated by red and blue lines, of which there are two in each plot: one to mark the transition from inhomogeneous broadening to motional narrowing, and one for motional narrowing to high-temperature relaxation. In the fused systems, the transition from inhomogeneous broadening to motional narrowing occurs for both polarons at the same temperature: at 100 K in AN and at 120 K in NN. High-temperature relaxation, on the other hand, sets in slightly later for holes than for electrons: in AN, electrons transition at 180 K while holes transition at 200 K, and in NN electrons transition at 200 K while holes transition at 220 K. Finally, in DPPT-TT motional narrowing sets in at about 40 K for electrons and at 80 K for holes, while high-temperature relaxation sets in at about 150 K for electrons and at 200 K for holes. It is important to note that, though we honed in on specific temperature points to find regime crossings after performing initial, low-resolution sweeps, the regime crossovers presented here are accurate only within ± 15 K.

To interpret these results, it is necessary to examine both the charge-carrier mobility and (de)localization of polaronic wavefunctions. The charge-carrier mobility is plotted in the bottom row of Figure 5.4. We see that for all systems at all temperatures, electron mobility is higher than that of holes. This difference is about an order of magnitude in the fused systems while for DPPT-TT the mobilities are nearly equal above 200 K and begin separating at lower temperatures. At room temperature electron mobilities for all systems are about 0.1 cm^2/Vs, and drop four orders of magnitude as the temperature is lowered to 80 K. Due to aforementioned injection issues, FET curves below 80 K in AN and DPPTT-TT and below 120 in NN were not recorded.

Based on the theory presented in Subsection 2.1.2, it is possible to estimate the localization of the wavefunction by determining the hyperfine coupling constant from ESR measurements: If a Gaussian signal is observed, then its root-mean-square width is determined by the variance of local fields experienced by individual spins in the system. By extracting this parameter from fits, the average variance and thus average extent of the wavefunction can be calculated. This typically requires measuring at 5 K, where electrons are frozen in their local environments. Unfortunately, this method was not possible for the data presented here, as all curves remained Lorentzian even down to 5 K. Thus, the hyperfine coupling had to be calculated by alternative means.

As explained in Section 2.3, decoherence in the inhomogeneous broadening regime is described by

$$T_2' = \tau_c + \frac{1}{\gamma_e \mathcal{B}_{rms}} \left(1 + \frac{1}{\gamma_e \mathcal{B}_{rms}^2 \tau_c} \right), \tag{5.1}$$

and in the motional narrowing regime by

$$T_2' = \frac{1}{\gamma_e^2 \mathcal{B}_{rms}^2 \tau_c}, \tag{5.2}$$

where $\mathcal{B}_{rms}$ is the root-mean-square fluctuation of the local fields and τ_c is the characteristic timescale on which they fluctuate. In organic semiconductors in the low- and mid-temperature ranges, it is reasonable to equate τ_c to the inverse of charge motion frequency and to take the local field fluctuations

	AN		NN		DPPT-TT	
	n	p	n	p	n	p
Crossover temperature [K]	100	100	120	120	30	80
Corresponding T_2' [ns]	204	125	339	108	63.3	52.0
Extracted $\mathcal{B}_{\text{rms}}$ [G]	0.84	1.40	0.54	1.62	2.70	3.28

Table 5.1 Crossover temperature, corresponding decoherence time (T_2'), and extracted $\mathcal{B}_{\text{rms}}$ at the point of crossover from inhomogeneous broadening to motional narrowing.

as resulting from local hyperfine fields.[15] Then, the crossover from inhomogeneous broadening to motional narrowing results from a shortening of τ_c (which is an increase in the motion frequency) due to the temperature-activated motion of charges. At this crossover point, both expressions must accurately give T_2^*, thus allowing one to combine them to calculate $\mathcal{B}_{\text{rms}}$. This procedure was done for both polaron types in all three systems. The calculated values are shown in Table 5.1. We see there that in all system holes have a larger $\mathcal{B}_{\text{rms}}$ than electrons. Because $\mathcal{B}_{\text{rms}}$ scales as $1/\sqrt{\mathcal{N}}$, where $\mathcal{N}$ is the number of nuclei over which a wavefunction is spread, this indicates that holes are more localized than electrons in the systems studied. (Refer to (2.17) of Subsection 2.1.2.*) As will be mentioned later in this chapter, this conclusion is supported by simulations in DPPT-TT. Further, the relatively small $\mathcal{B}_{\text{rms}}$ values in AN and NN may be due to the fact that polarons are able to delocalize over relatively large distances in these fused systems.[63] (However, this is only a hypothesis, as direct polaron localization lengths for AN and NN have yet to be calculated.) Finally, it is a point of curiosity that the system with the highest degree of symmetry, NN, also has the largest difference between electron and hole hyperfine field strength (0.54 G vs. 1.62 G). Additional experiments and simulations are likely required to understand this.

With mobility and hyperfine data presented, we are now in a position to interpret the relaxation times displayed in Figure 5.4. In AN, the equal onset of motional narrowing for polarons is explained by the small difference in their respective mobilities around the crossover temperature: Below 100 K, both electrons and holes hop relatively slowly, meaning they don't experience enough hyperfine field fluctuations (per unit time) to average-out local differences between other electrons (or holes); only after 100 K are their mobilities high enough to ensure a motionally narrowed resonance. For DPPT-TT, there is over an order-of-magnitude difference in polaron mobilities at 100 K, and this difference increases with decreasing temperature. Thus, because electrons are so much more mobile than holes in this regime, their motion is rapid enough to average-out local differences at much lower temperatures than holes.

As originally proposed by Schott et al.,[15] the decrease of T_2 at high temperatures can be explained by a spin-shuttling model of relaxation. In this regime, active vibrational molecular modes shuttle

*A potential point of concern is that (2.17) was introduced in the context of an inhomogeneously broadened signal, and the signals presented here remain Lorentzian even at 5 K. However, we note that the $\mathcal{B}_{\text{rms}}$ values here are not extracted by fitting the individual spectra, but instead from equations (5.1) and (5.2). Consequently, they correctly describe the local field fluctuations in the absence of motion. In other words, the $\mathcal{B}_{\text{rms}}$ values here are those that *would give rise to the inhomogeneously broadened signal* if carrier motion were completely frozen. As a result, they remain valid for (2.17).

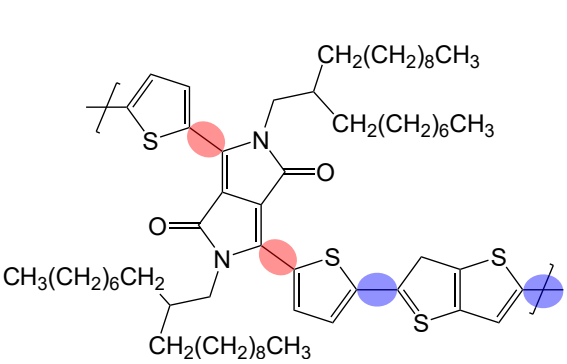

(a)

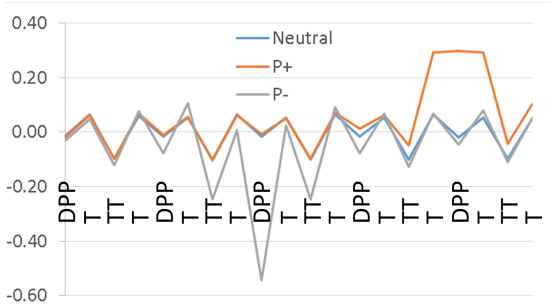

(b)

Neutral	0.1°	26.3°	26.1°	0.1°	0.1°	26.1°	26.1°	0.1°	0.1°	26.1°	26.2°	0.1°	0.1°	26.1°	26.2°	0.1°	0.1°	26.0°	29.0°
Cation	0.1°	26.4°	26.2°	0.1°	0.1°	26.2°	26.1°	0.1°	0.1°	26.3°	26.5°	0.2°	0.1°	23.1°	1.0°	0.0°	0.1°	1.0°	24.7°
Anion	0.1°	25.6°	23.7°	0.1°	0.0°	0.4°	0.0°	0.0°	0.0°	0.1°	0.3°	0.0°	0.1°	22.8°	23.5°	0.2°	0.1°	24.9°	29.0°

(c)

Fig. 5.5 **(a)** The DPPT-TT molecule with DPP-T and T-TT sites of torsion highlighted in translucent red and blue, respectively. **(b)** The localization of the radical cation and anion wavefunctions simulated for a chain of five repeat units. **(c)** The angles of torsion at DPP-T (red) and T-TT (blue) links calculated for a chain of five monomers. The table starts from a DPP-T link, followed by T-TT, TT-T, and T-DPP, then repeats for the remaining four monomers. Values are shown for the neutral polymer, radical cation, and radical anion. The boxed regions show where the radical cation and anion wavefunctions are localized on the chain.

electronic wavefunctions back-and-forth along the molecular backbone many times before a single hopping event, and each shuttling event presents an opportunity for relaxation. Motional narrowing is no longer sufficient to average-out local differences in magnetic environments. In this regime the spatial location and extent of the wavefunction is critical: highly localized wavefunctions will be heavily affected if they are localized primarily around the site of torsion, and will barely be affected if they are located away from the site. To examine whether this is a reasonable explanation for the data presented in Figure 5.4, it is necessary to examine the polaron wavefunctions. Such data does not yet exist for AN and NN, but the fused structures should yield relatively similar wavefunctions and thus similar onsets of spin-shuttling — as observed. For DPPT-TT, we now turn to simulations of its charge-transport parameters.

5.3.3 Simulations on DPPT-TT

The theoretical work in this section was performed by David Beljonne and Vincent Lemaur at the University of Mons. Details of their work on this system can be found in Chaudhari et al. (2017).[71]

Figure 5.5(a) shows the possible sites of torsion in DPPT-TT (red ovals are DPP-T bonds and blue T-TT bonds). Figure 5.5(b), the localization lengths of the polaron wavefunctions are shown for a simulation of five repeat monomers. We see that the radical cation is delocalized over a single DPP unit and its two connected thiophene units, while the radical anion is delocalized over a single DPP unit and its two next-neighbor thiophene units. Moreover, these simulations show that holes have a

shorter delocalization length than electrons, which matches our prediction of the wavefunction spread as determined by hyperfine coupling strengths: electrons are calculated to have a $\mathcal{B}_{\text{rms}}$ of 2.70 G while that of holes is 3.28 G. Though these simulations don't show the *evolution* of the wavefunction in response to torsion,* (which is the cause of spin relaxation according to the spin-shuttling model) they do seem to agree with our results. We argue that spin-shuttling relaxation sets in later for holes because the hole wavefunction is localized away from torsional sites that drive relaxation. From Figure 5.5 we see that the radical cation is localized primarily over a DPP unit and its nearest neighbor thiophene unit, which does include the DPP-T torsional site but not the T-TT site. This should be compared to the electron wavefunction, the bulk of which is located on a DPP unit, but spreads over the nearest thiophene units and onto the thiophene-thiophene units. (See the bottom panel of the figure.) Thus, the electron wavefunction sees all torsional sites to some degree, while the hole wavefunction sees only a DPP-T link. We therefore hypothesize that spin relaxation in the spin-shuttling regime is driven primarily by torsion at the T-TT bonds.

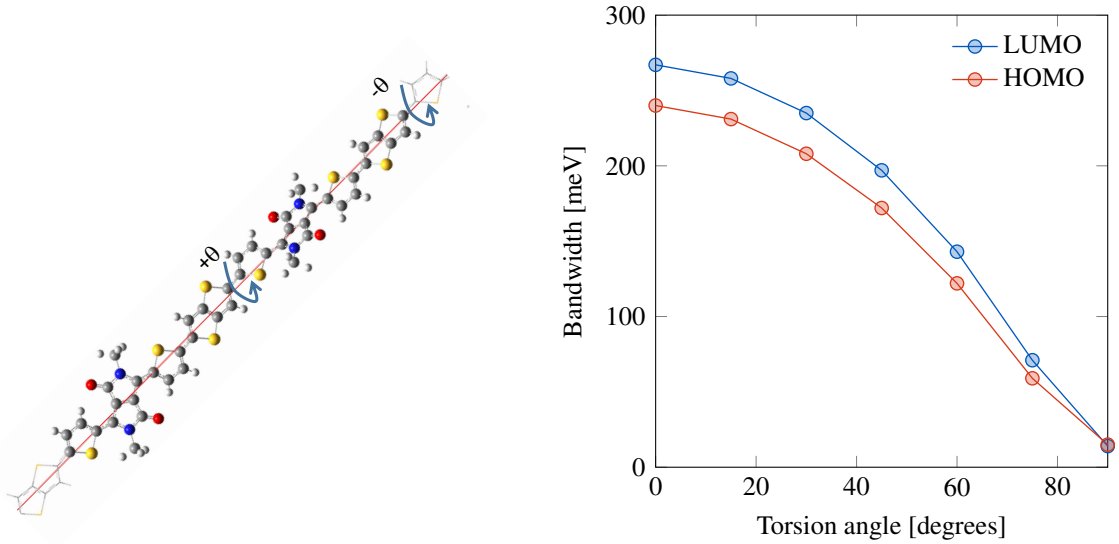

(a) (b)

Fig. 5.6 HOMO and LUMO bandwidths vs. torsion angle in DPPT-TT. **(a)** Two DPPT-TT monomers selected from a simulated pentamer. The sites of torsion considered are the T-TT links. **(b)** The HOMO and LUMO bandwidths plotted as a function of torsion angle for the TT-T link. For all torsion angles, electrons have a larger bandwidth — thus suggesting a higher mobility.

To investigate the impact of the T-TT link on dynamics in more detail, we calculated the bandwidths of the frontier orbitals for increasing torsion. Figure 5.6(b) shows the HOMO and LUMO bandwidths as a function of θ at the T-TT link. From 0 to 90°, electrons have a higher bandwidth than holes, although this difference is greatest at small angles and decreases as θ increases; both bandwidths naturally decrease as torsion increases. (The left panel of the same figure shows two monomers from a simulated chain of five. The T-TT link under consideration is marked.) The internal reorganization energies for

*Such simulations were in progress at the time of writing this thesis, but were unfortunately not finished in time.

	λ_+ [meV]	λ_- [meV]
Monomer	86	57
Pentamer	71	60

(a)

Dimer	t_{HOMO} [meV]	t_{LUMO} [meV]
1	12.1	32.5
2	0.04	0.01
3	27.5	75.7

(b)

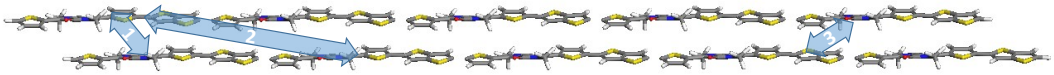

(c)

Fig. 5.7 **(a)** The internal reorganization energy of an electron and hole in DPPT-TT simulated for a monomer and a pentamer. In all cases, the electron has a lower energy barrier to reorganization. **(b)** The transfer integrals for dimers between two DPPT-TT pentamers. Values are nearly equal or larger for electrons than holes. **(c)** The locations of the dimers considered for the transfer integrals.

holes and electrons (computed for a monomer and pentamer) are shown in Figure 5.7(a), while the transfer integrals for dimers between two simulated pentamers are shown for the HOMO and LUMO in Figure 5.7(b). (Figure 5.7(c) shows exactly where these dimers are located along the DPPT-TT chains.) Not only do electrons have smaller barriers to reorganization than holes, but also have greater transfer integrals on average.* These observations, combined with the fact that electrons have a larger bandwidth over all torsion angles, suggest that electrons are more mobile than holes. These calculations provide theoretical support for our reported measures of mobility and, as a consequence, hopping frequency.

5.4 Discussion

In this chapter we measured ambipolar systems in FI-ESR to study the interplay of wavefunction localization, polaron mobility, and spin relaxation in organic semiconductors. By comparing electron and hole wavefunctions in two fused systems (where polaron wavefunctions should be similar to each other and double linkages promote rigid chains, thus creating less thermal disorder) to donor-acceptor systems (where polaron wavefunctions are expected to differ more from one another), we clarified the extent to which different relaxation regimes are modulated by wavefunction localization and by charge transport characteristics.

In all three systems we observed the three regimes of relaxation commonly seen in organic polymers: inhomogeneous broadening, motional narrowing, and high-temperature relaxation (which we attribute to torsion-induced spin-shuttling). In the two fused systems (AN and NN), motional narrowing set in at the same temperature for both holes and electrons, while in DPPT-TT electrons displayed a motionally narrowed signal at much lower temperatures than holes. This observation is readily understood when the differences in polaron mobilities across the model systems are considered: in the fused systems, polaron

*For dimer 2 the hole has a larger transfer integral, but the values here are so small for both polaron types that they are offset by those of dimer 1 and 3.

mobilities are nearly equal at low temperatures (thus meaning motional narrowing sets in for both at the same temperature), while in DPPT-TT there is over an order-of-magnitude difference in electron and hole mobility below 150 K. Thus, the transition from inhomogeneous broadening to motional narrowing is largely unaffected by wavefunction localization.*

Previous work on spin relaxation in organic semiconductors has mainly been confined to the motional narrowing regime — where the EPR linewidth is narrowed by the fast motion of charge transport — and the inhomogeneous broadening regime — where charge transport is too slow to narrow the linewidth. Though a breakdown of the motional narrowing theory at relatively high temperatures (> 150 K, e.g.) had been observed previously, Schott et al.[15] first offered a potential explanation for the increase in linewidth: as higher temperatures allow molecules to access torsional modes between linked units, the picosecond-fast reorganization of electron wavefunctions in response to nuclear torsion drives spin relaxation. Here we provided a systematic test of this theory by using three ambipolar systems, two of which are fused systems and the other a donor-acceptor molecule. This choice of materials allows us to compare spin relaxation as a function of wavefunction delocalization around torsional sites.

In transitioning from motional narrowing to high-temperature relaxation, all three systems show a difference in onset between holes and electrons: around 20 K in the fused systems and 50 K in DPPT-TT. Through an estimation of delocalization length of holes vs. electrons (calculated from hyperfine coupling strengths and confirmed by simulations), we attribute these onsets to the spread of polaron wavefunctions: in all three systems holes are not only more localized than electrons, but are localized away from specific sites of torsions; they are thus less affected by torsion than electrons, and therefore higher temperatures (resulting in higher torsional amplitudes) are needed to effect the same magnitude of relaxation. Though we await molecular dynamic simulations to support this, preliminary simulations on DPPT-TT are promising: calculations show that electrons are more mobile than holes, are indeed more delocalized than holes, and specifically are localized at different torsional sites than holes. Thus, it is these sites that are likely responsible for relaxation in DPPT-TT. We hope similar simulations on the fused systems to be complete in the near future.

*To be clear, here we suggest that there is not a strong direct correlation. Indirectly, wavefunction localization affects mobility, which in turns modulates relaxation.

CHAPTER 6

ELECTRICALLY DETECTED MAGNETIC RESONANCE IN AMBIPOLAR POLYMERS

Field-induced electron spin resonance is a powerful probe into the dynamics of charges injected into electronic and spintronic devices. However, as it stands, the insights it provides are limited to the bulk, static properties of the system, such as relaxation and coherence times, motion frequencies, and hopping distances. To fully take advantage of the field-effect transistor architecture, one can measure the resonance properties of a device under operation (i.e., with a source-drain current flowing). Such a measurement is known as *electrically detected magnetic resonance*, or EDMR. In this chapter, EDMR measurements are used to identify the source of spin-dependent electrical currents in devices under operation.

6.1 Introduction

The principles of an EDMR measurement are quite similar to those of FI-ESR: A microwave field is applied at a given frequency to provide the energy required for resonance. A DC magnetic field is then swept, and resonance occurs when the energetic difference between the spin states matches that of the microwave field. The difference from standard ESR measurements is that the device is under operation during the measurement.* Rather than measuring the absorption of the magnetic field due to resonance, the current flowing through the device is monitored as the field swept. Therefore, an EDMR signal appearing at the fields required for ESR resonance reflects a change in current due to a changing spin population. In this way, EDMR allows us to probe the spin-dependent physics of device operation. It is a particularly sensitive technique because it detects only those spins which are relevant to device operation (unlike ESR, which detects all spins in the system).

EDMR measurements have been used extensively to study spin-dependent phenomena in semiconductor devices. While most of this effort has focused on inorganics, significant headway has been made studying organics. In solar cells, for example, EDMR has been used to (1) show that, in donor-acceptor blended systems, photocurrents result from p-type polarons in the donor and n-type polarons in the

*In the case of FETs, this means a current is flowing between the source and drain electrodes.

acceptor;[72] (2) distinguish between bipolar polaron-pair recombination and unipolar bipolaron hopping;[73*] (3) uniquely identify the spectral features of charge-transfer and triplet-exciton states.[74] Beyond that, EDMR has been used to measure the exchange, dipolar,[75] and hyperfine[76] coupling strengths of the paramagnetic centers in spin-dependent transport.

As the primary charge carriers in disordered organics, polarons are naturally of tremendous interest in EDMR studies. While oppositely charged polarons combine to form or dissociate from excitons, those of the same charge can bind together to form bipolarons. These pairs have been proposed as an explanation for various phenomena in organic devices, such as the efficiency of OLEDs and organic magnetoresistance.[77] A particular point of controversy is the attribution of spin-dependent electrical currents in organic solar cells to spin-dependent bipolaron formation. In their model, Behrends et al. (2010)[78] propose that an EDMR signal originates from the interaction of a trapped polaron with an incoming mobile polaron of the same charge: if the two polarons have the same spin then the mobile polaron cannot move to the trap site, thus inhibiting charge transport. This is evidenced by the fact that device current improves under resonance of a low microwave field, which occurs because the field rotates only one member of the spin pair, thus allowing the two spins to break their singlet configuration and subsequently move past one-another. At higher fields, both members rotate equally, thus "locking-in" the singlet state and preventing charge transport. Boehme and Lupton (2013), however, demonstrate that qualitatively similar signals would result from polaron-pair recombination, a process they rightfully point out is non-negligible in many organic semiconducting devices.[79]

It is the aim of the experiments described here to elucidate these spin-dependent current phenomena. To do so, ambipolar devices are measured. Their utility is that, through careful manipulation of the source-drain and gate voltages, the device can be swept from one unipolar regime (e.g., the n-type), through the recombination regime, and finally to the other unipolar regimes (e.g., the p-type). Doing so should give a clear evolution of the EDMR spectrum, wherein bipolaron signatures appear only in the unipolar regimes and a superposition of unipolar bipolaron and bipolar signatures appear in the recombination regime.

6.2 Operational Regimes of Ambipolar OFETs

The current-voltage behavior of these devices can be modeled by successive applications of the standard OFET equations.[58] To do so, it is helpful to examine Table 6.1, which shows how the regime of device operation changes as a function of drain and gate voltage.[†] Beginning with $V_d = 0$ and increasing the gate voltage, charges begin to accumulate across the channel $V_d > V_{th}^e$. Applying a small (positive) drain voltage will cause the accumulated electrons to flow, and the device will be in the *electron-only,*

*A note on the terminology used here is important since there is not consistency across the literature: A polaron pair refers to two polarons that are coupled but do not occupy the same orbital. The two polarons may be of the same charge (bipolar polaron pair) or of different charges (unipolar polaron pair). In either case, these pairs are typically short-lived because the polarons quickly move to occupy the same orbital. The result is then known as a bipolaron if they are of the same charge or an exciton if they are different.

†For simplicity, the table assumes that the source electrode is kept at zero volts.

linear regime so long as the drain voltage remains small compared to the effective gate voltage, i.e., $V_d < V_g - V_{th}^e$. Increasing the drain voltage to the point past which this condition is violated will cause the device to operate in the *electron-only, saturation regime* due to the pinch-off point created at the drain. By continuing to increase the gate voltage further, eventually the difference between the drain and gate will be large enough to overcome the barrier to hole injection, and holes will be injected from the drain into the channel. This, the *ambipolar regime*, is defined by the equations $V_g > V_{th}^e$ and $V_d > V_g - V_{th}^h$; both currents will be in the saturation regime. From this point, decreasing the gate voltage will eventually result in $V_g < V_{th}^e$, which stops electrons from being injected into the channel from the source; this is the *hole-only saturation regime*. Finally, once the gate voltage is negative enough to overcome the barrier to hole injection, holes will be injected nearly uniformly into the channel and the device will operate in the *hole-only linear regime*.

Regime		Condition(s)		$\lvert I_{sd}\rvert$
Electron-only	Linear	$V_g > V_{th}^e$	$V_d < V_g - V_{th}^e$	$\frac{Wc}{L} V_d \mu_e \left[(V_g - V_{th}^e) - \frac{V_d}{2}\right]$
	Saturation	$V_g > V_{th}^e$	$V_g - V_{th}^e < V_d < V_g - V_{th}^h$	$\frac{Wc}{2L} \mu_e (V_g - V_{th}^e)^2$
Ambipolar	Saturation	$V_g > V_{th}^e$	$V_d > V_g - V_{th}^h$	$\frac{Wc}{2L} \left\{ \mu_e (V_g - V_{th}^e)^2 + \mu_h \left[V_d - (V_g - V_{th}^h)\right]^2 \right\}$
Hole-only	Saturation	$V_g < V_{th}^e$	$V_d > V_g - V_{th}^h$	$\frac{Wc}{2L} \mu_h \left[V_d - (V_{th}^h)\right]^2$
	Linear	$V_g < V_{th}^e$		$\frac{Wc}{L} \mu_h \left\{ V_d \left[V_d - (V_g - V_{th}^h)\right] - \frac{V_d^2}{2} \right\}$

Table 6.1 The different operating regimes, defining conditions (in terms of voltage differentials), and resulting source-drain currents in ambipolar OFETs.

6.3 Experimental Design

6.3.1 Methods

The material system chosen for these measurements was the anthracene-naphthalene copolymer introduced in the previous chapter. The EPR data there acts as a reference for the EDMR data presented here. The chemical structure of AN is shown in Figure 6.1.

EDMR measurements were performed on top-gate, bottom-contact FET devices: Fused-quartz plates (UQG Optics, FQP-5005) were cut to 40 mm x 40 mm squares with a diamond saw, then ridges of depth 0.3 mm were cut into one side of the glass along its full length at the 3 mm mark, 4.5 mm mark, 7.5 mm mark, 9 mm mark, etc. After cleaning, we used photolithography followed by metal evaporation to deposit interdigitated source and drain contacts with a total channel width and length of 243 mm and 0.1 mm per device, respectively. The odd layout of the electrodes is due to the narrow constraints of the ESR cavity coupled with the need for high carrier injection in order to detect a signal. Using this method, each quartz plate yields eight FETs. A picture of a device with the same layout is shown in Figure 4.1.

Solutions of AN were created by adding 10 g/l of polymer to trichlorobenzene and dissolving for 1 hour at 160° C. We heated the substrates at 150° C for five minutes, then spin-coated the solution

onto them at 1200 rpm for 6 minutes using hot glass pipettes (also heated at 150° C for five minutes). Immediately afterward we annealed the samples by placing them on a hot plate at 160° C for 5 minutes, then 250° for 30 minutes, and finally quenching them.

After polymer deposition we spin-coated PMMA at 1400 rpm for 30 seconds, then annealed at 80° C for 30 minutes. This method results in a PMMA layer that is 400 nm thick and has a dielectric constant of 3.6. We finished fabrication by evaporating aluminium gates of thickness 30 nm over the active areas.

Individual devices were separated from the 4 cm x 4 cm square by applying pressure along the length of the 0.3 mm indents. In some cases, it was helpful to first cut through the dielectric and polymer over the grooves using a scalpel. This prevented the dielectric from peeling off the gate upon device separation.

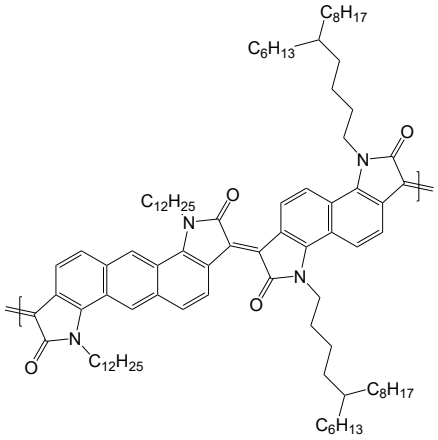

Fig. 6.1 The chemical structure of AN. Reprinted from Chapter 5.

To perform EDMR measurements, a transistor was attached and wire-bonded to a substrate holder with source, drain, and gate connections. The sample-and-holder combination was then slid into a Wilmad Suprasil EPR tube (Sigma-Aldritch product no. Z5674XX) and sealed under nitrogen. The sample was then loaded into an Oxford Instruments ESR900 cryostat, which was controlled by an Oxford Instruments Mercury iTC. EDMR measurements were taken on a Bruker E500 spectrometer using a Bruker ER 4122SHQE cavity and an X-band microwave source, and a Keithley 2602b source unit was used for electrical characterization. CustomXepr, a Python package developed by Sam Schott, was used to integrate the above-mentioned instruments and automate measurements when desired.[15]

6.3.2 Experimenter contributions

Professor Jan Behrends of Freie Universität Berlin initiated contact to begin this collaboration. In addition to proposing the original idea, he also provided EDMR training, equipment, facilities, and insight. The author — in equal contribution with Sam Schott — helped design the experiment, fabricated devices, recorded data, and analyzed results. Henning Sirringhaus provided insight in the interpretation of results.

6.4 Results & Analyses

The basic principle of an EDMR measurement requires that spin-polarized ensembles of charge carriers interact with each other in the electrical current. This means that charge carriers must encounter each other before spin polarization is lost, *i.e.*, before time T_1 elapses. Thus, both long spin-diffusion lengths and long longitudinal relaxation times are favorable in EDMR measurements.

6.4.1 Detection of bipolaron-inhibited and recombination currents

The left panel of Figure 6.2 shows the dependence of T_1 on temperature in AN, and the right panel shows that of mobility. Though it is evident that measurements at low temperatures would give long T_1 values, this regime would also result in low spin-diffusion lengths due to the immobility of charges. The best balance of T_1 and λ_d is instead obtained when both mobility and longitudinal relaxation time are reasonably long. This occurs at the maximum of the motional narrowing regime, which is around 200 K for both holes and electrons.

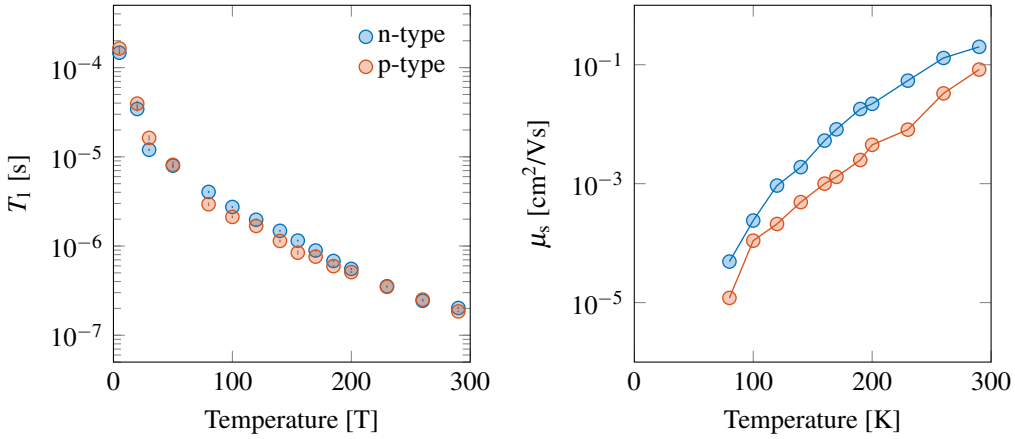

Fig. 6.2 The dependence of T_1 (**left**) and mobility (**right**) on temperature in AN.

Because EDMR is a measurement of the change of device current (ΔI), it scales with the magnitude of the applied current. Thus, to properly compare EDMR signals across a range of drain and gate voltages, it is necessary to either keep the applied current constant across measurements or to normalize against the applied current ($\Delta I/I$). For our first series of measurements, we swept through different regimes of device operation (as determined by Table 6.1) under a constant applied current of 4 μA. The V_g vs. V_d curves required to maintain these currents are depicted in Figure 6.3(a). On each plot the $V_g = V_{th}^h$ line, the $V_g = V_{th}^e$ line, and the $V_d = V_g - V_{th}^h$ and $V_d = V_g - V_{th}^e$ lines are shown in gray dashed lines. By the conditions of Table 6.1, these delineate the regimes of device operation as the gate voltage is swept from left to right. As labeled in the plot, these are linear hole-only, saturation hole-only, ambipolar, no theoretical solution,* and linear electron-only. The black dots on the curve depict where EDMR scans were recorded.

In Figure 6.3(b) are shown the transfer curves as gate voltage is swept for varying values of source-drain voltage. The black dots correspond to the same points at which EDMR scans were recorded. Again, it is clear that the different regimes of device operation are swept through.

The recorded EDMR curves are shown in Figure 6.3(c).† A clear EDMR signal was observed in every regime except linear electron-only. For all other curves, the same Lorentzian contribution —

*This regime occurs between the $V_g = V_{th}^h$ and $V_d = V_g - V_{th}^e$ lines.

†Note that only the applied gate voltages are shown for these curves. The corresponding source-drain voltages are found from the V_g vs. V_d curves.

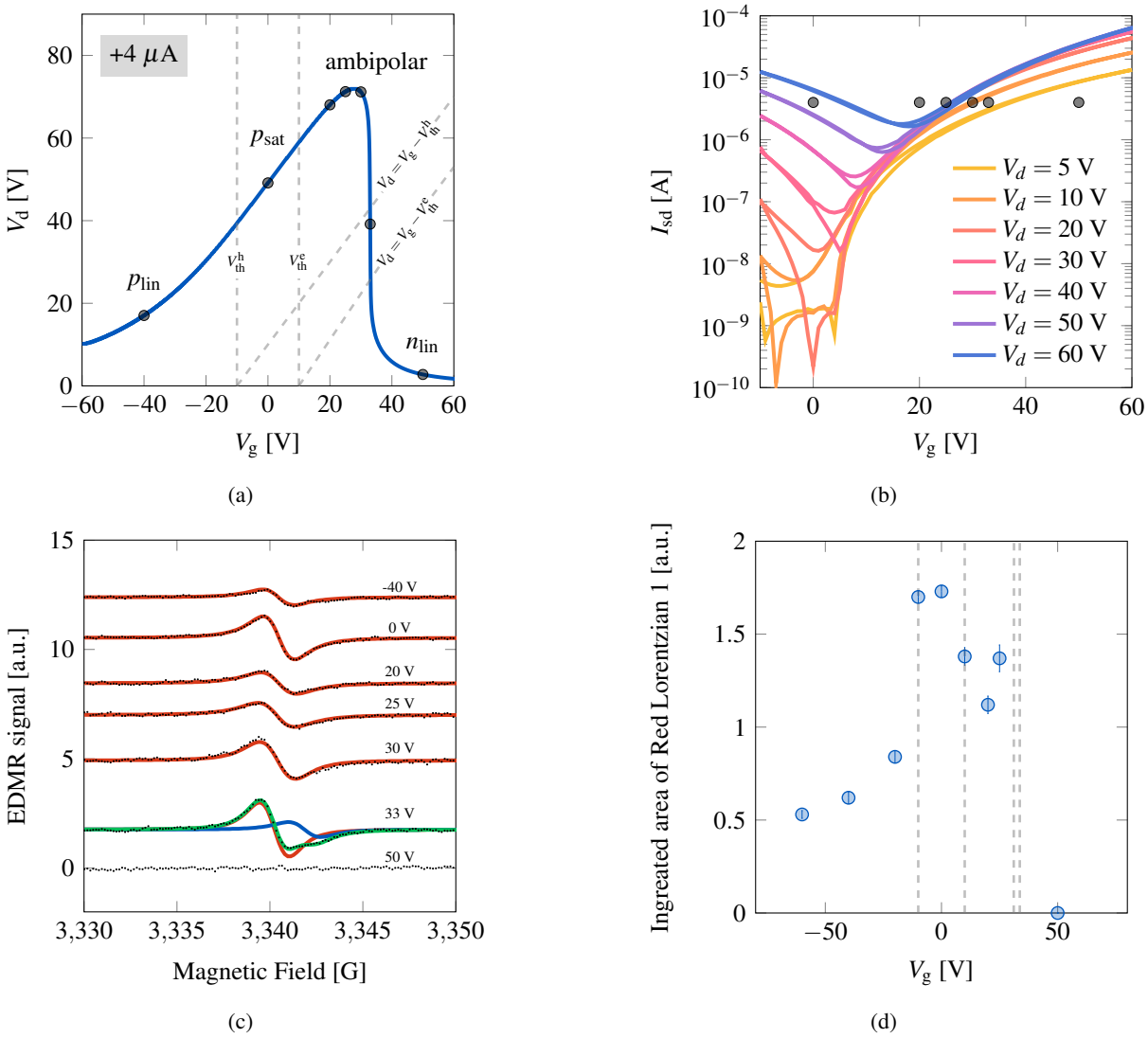

Fig. 6.3 At 200 K: **(a)** Measured drain voltage as a function of gate voltage while driving a constant current of 4 μA through the FET. The different regimes of device operation are divided by the conditions delineated in Table 6.1. Black dots indicate gate voltages at which an EDMR scan was recorded. **(b)** Transfer curves for the device taken at increasing source-drain voltage. Black dots again depict the values at which EDMR curves were recorded. **(c)** EDMR spectra recorded at various gate voltages. Each spectrum corresponds to one black dot on the plots in the upper row. The red trace is one Lorentzian, the blue a second, and the green a combined fit. **(d)** Integrated area of the red Lorentzian as a function of gate voltage. The dashed lines refer to the same regimes of device operation as listed in the top left panel.

shown in red and with a g-factor of 2.00335 $\pm$ 0.00005 and a peak-to-peak linewidth ranging from 1.27 to 1.60 G — was present. Though this was a sufficient fit for most of the spectra, one curve in the ambipolar regime required a second Lorentzian contribution for a proper fit: this is the blue curve in the $V_g = 33$ V spectrum. (The green curve is the combined fit.) The g-factor for that Lorentzian is 2.0022 G and its peak-to-peak linewidth 0.12 G. The integrated area of the red Lorentzian in each spectrum is shown in the bottom right panel of this figure.

To identify these two contributions, we first note that the linear electron-only regime is the sole regime for which no signal is observed. At the opposite extreme however, the linear hole-only regime displays a clear EDMR signal even at -70 V, where no electrons are present. These observations suggest that the red Lorentzian is produced by a current containing only p-type polarons. To confirm this, we recorded EPR scans simultaneously with the EDMR scans for -60 V and 50 V, the spectra for which are shown in the Figure 6.4. In the left panel, we see that the EPR curve produced for $V_g = -60$ V in an operational device is the same as seen in a device with $V_{sd} = 0$.* More importantly, the corresponding EDMR signal shares the same resonance position as the EPR signal, but has a wider linewidth (0.2 G vs. 1.7 G). This suggests that the spin species producing the signal is the same as in EPR (p-type polarons) but has a greater distribution of g-factors. This observation agrees with bipolaron-inhibited transport: In this model, a mobile polaron occasionally is prevented from moving to a new site because the new site contains a trapped polaron whose spin matches that of the mobile polaron. Sweeping through resonance produces an EDMR signal because the microwave field flips one of the two polarons, thus allowing them to occupy the same orbital. The distribution of g-factors of the mobile polarons will be relatively narrow due to motional narrowing (see Subsection 2.3.1), but that of the trapped polarons will be wider. Thus, as the field sweeps, it will encounter the g-factors of the trapped polarons first. Because each EDMR event requires only one of the two polarons to flip, a signal will be produced in this region. In other words, it is the wider distribution of g-factors that sets the width of the EDMR signal.

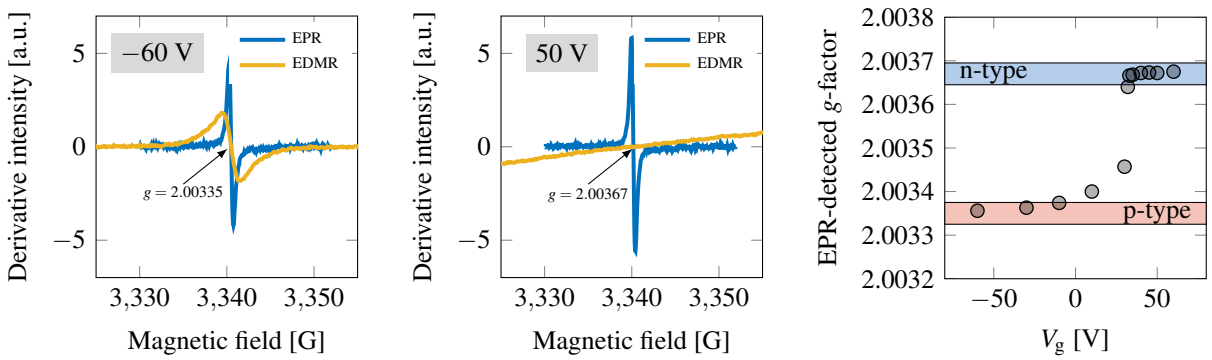

Fig. 6.4 **(a)** The EPR and EDMR signals of a device with $I_{sd} = 4\ \mu$A and $V_g = -60$ V at 200 K. The resonance positions of the two signals overlap, though the linewidth of the EDMR signal is larger: (0.2 G vs. 1.7 G). **(b)** The same comparison for $V_g = 50$ V. No EDMR signal is observed in this regime. **(c)** The gate-voltage dependence of the EPR g-factor for a device running at 4 μA. The ranges of g-values observed for pure p- and n-type signals are shaded in red and blue, respectively.

The integrated area of the red Lorentzian — shown in Figure 6.3(d) — also supports the bipolaron-inhibited transport model. Its value increases slowly as the device is swept through the linear p-type regime, sharply maximizes as it enters the saturation p-type regime, decreases slightly in the ambipolar regime, then disappears in the linear n-type regime. That the signal is maximized in the saturation

*That data is presented in the previous chapter.

regime can be understood from the OFET theory introduced in Section 3.1: In the saturation regime, the charge density at any point in the channel is lower (than in the linear regime). As a result, polarons have fewer percolation pathways through which they can travel, thus making them more likely to encounter trap states. The bipolaron-inhibited-transport signal is still present in the ambipolar regime, but slightly decreased since some mobile p-type polarons recombine with n-type polarons.

In the middle panel of the same figure, we see that the EPR curve for $V_g = 50$ V is the same in an operational device as in one with $V_{sd} = 0$; this confirms that electrons are injected into the channel. However, in this instance an EDMR signal is not observed, again suggesting that the bipolaron-inhibited transport occurs only for p-type polarons. Further, the right panel of the figure shows the shift of the EPR-detected g-factor with gate voltage in an operational device. We can see from it that the EPR signal shifts from purely p-type to n-type as the gate voltage is swept along the V_g vs. V_d curve. This shows that the presence of both polarons in the channel has a demonstrable effect on resonance position, which is then reflected in EDMR. Because our observed EDMR signal in the pure p-type domains does not show this shift, it is unlikely to arise from a recombination current.

The second contribution in the ambipolar regime shows a linewidth on the order of EPR-detected linewidths for both n- and p-type signals (0.2 G), which is expected of a recombination signal from two equally narrow spin distributions. To confirm that the signal is only present in the ambipolar regime, we took a second set of measurements for a constant current of -4 μA. The V_g vs. V_d curve and the EDMR curves are shown in Figure 6.5. Figure 6.6 shows the full fits of the +4 μA and -4 μA recombination signals.

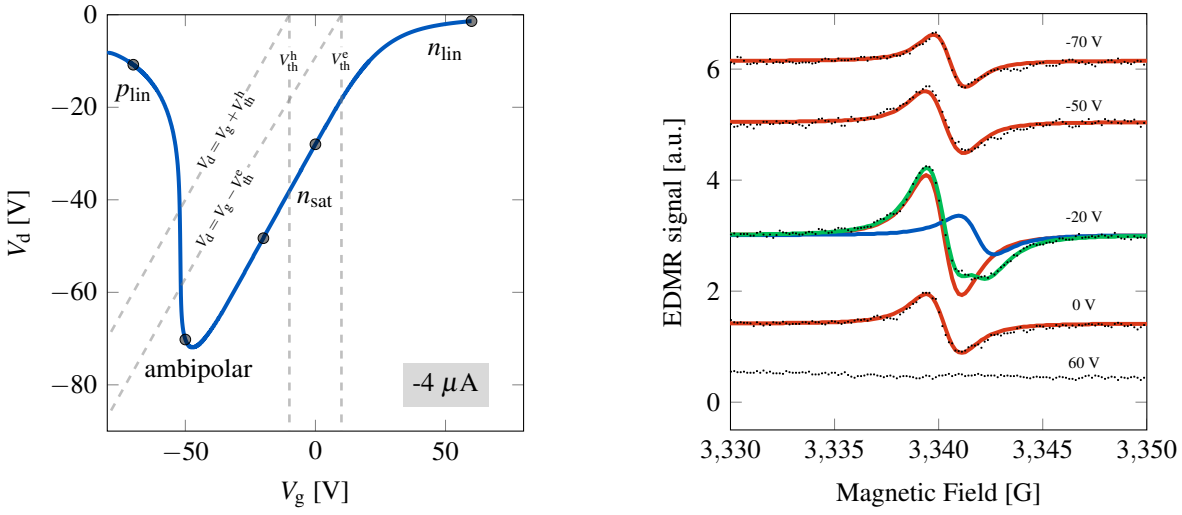

Fig. 6.5 **(a)** The V_g vs. V_d curve for a constant current of -4 μA. Different regimes of device operations are determined by the conditions from Table 6.1. Black dots are points at which EDMR curves were recorded. **(b)** Corresponding EDMR spectra. Red traces we assign to a bipolaron-inhibited current, blue to a recombination current, and green to their combined fit.

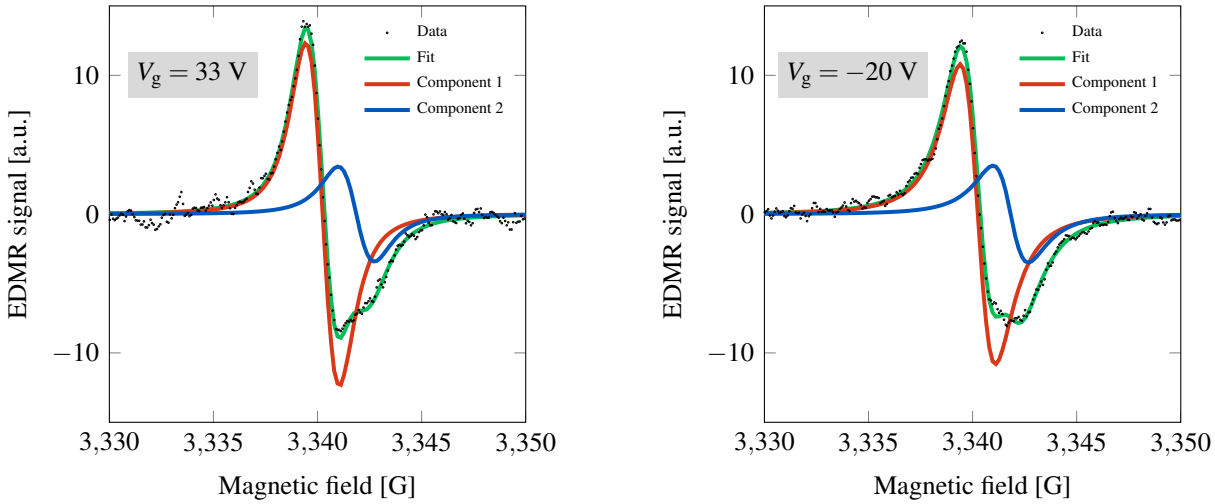

Fig. 6.6 **(a)** The EDMR spectrum of a device with $I_d = +4\mu$A, $V_g = 33$ V, and $V_d = 39.2$ V. The red trace we attribute to bipolaron-inhibited transport, the blue to a recombination current, and the green to their combined fit. **(b)** The corresponding spectrum and fit for a device with $I_d = -4\mu$A, $V_g = -20$ V, and $V_d = -48.3$ V.

In the case of -4 μA, the electron-only saturation regime was swept through, and there an EDMR signal was observed. Fitting reveals the g-factor to be 2.00367, which is within error for the n-type g-factor recorded by EPR. We therefore propose that this signal corresponds to bipolaron-inhibited transport in electrons. Interestingly, though the argument that fewer percolation paths exist for polarons in the saturation regime explains why a signal is observable there, it does not explain why no signal is observable in the linear regime (as shown in Figure 6.3(c)). To explain this, we note from EPR measurements (reported in the last chapter) that electrons have larger delocalization distances than holes and are more mobile. Thus, in the linear regime they are more able (than holes) to take advantage of the percolation paths that exist and thus have a smaller (non-observable) EDMR signal. A signal only develops when electrons become less able to explore these paths, such as in the case of saturation).

6.4.2 Temperature dependence of the bipolaron-inhibited signal

To better understand the p-type bipolaron signal, we measured its temperature dependence well outside the ambipolar regime. To determine a suitable gate voltage at which to record the measurements, we first recorded V_g vs. V_d curves for the temperature range required; those are displayed in Figure 6.7(a). As can be seen, the overall shape of the plot is consistent across changes in temperature. There is a slight variation in intensity and position, but this evolution is not solely due to temperature: lower currents had to be used at lower temperatures to prevent the device from being damaged.* Regardless, $V_g = -10$ V remained near the hole-only, linear/saturation boundary, making it suitable for measurements. A more

*Values chosen were 100 nA at 70 K, 10 μA at 190 K, and 20 μA at 210 and 270 K.

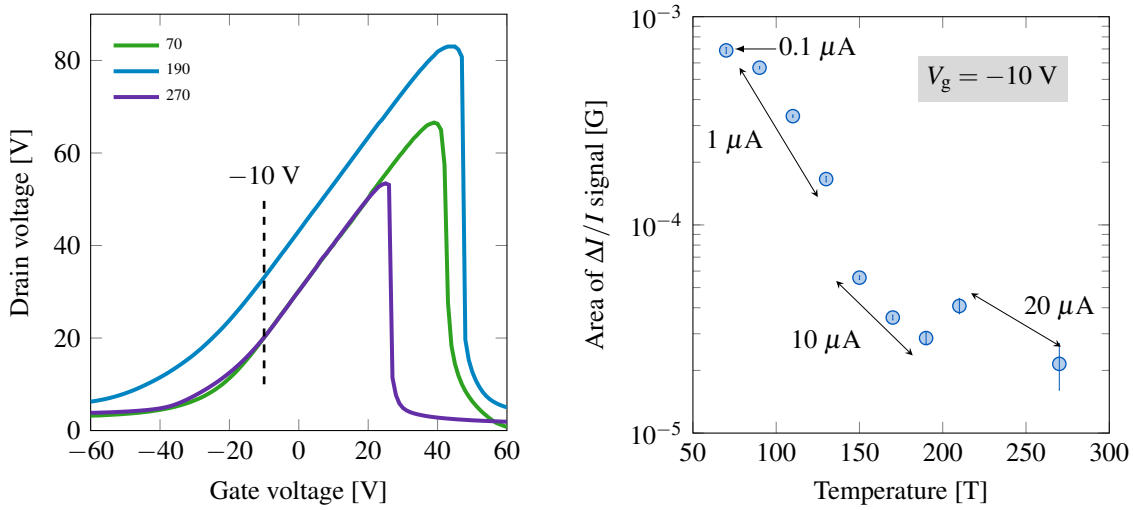

(a) (b)

Fig. 6.7 **(a)** V_g vs. V_d curves for constant currents of 0.1 μA at 70 K, 10 μA at 190 K, and 20 μA at 290 K. **(b)** Temperature dependence of the area of the normalized current in the EDMR signal at $V_g = -10$ V. The applied current for each temperature range is displayed near the data points.

extreme value was not chosen in order to prevent the device from degrading as a result of high applied voltages at lower temperatures.

Figure 6.7(b) shows the evolution of the area of the normalized EDMR signal. Almost monotonically with temperature, the area of the normalized signal decreases from 70 K all the way to 260 K. This indicates fewer spin species participating in the spin-affected current. While a qualitatively similar behavior is observed in EPR signals, it is important to note that the origin is not the same: The area of an integrated EPR signal typically follows the Curie dependence $\sim 1/T$, which is a result of the Boltzmann distribution of states, $\sim \exp[-\varepsilon_k/k_B T]$.* Specifically, as temperature is lowered the material becomes more spin-polarized because the thermal energy isn't large enough to bridge the gap between the split spin states. This results in each resonance event flipping more spins and therefore producing a stronger signal. In EDMR however, spin-flips alone do not cause a signal, but rather they effect some change in the measured current that is detected as a signal.† The decay of the EDMR signal here likely reflects fewer trap states (due to elevated temperatures) inhibiting polaron transport. This is in stark contrast to the expected behavior of a recombination signal, wherein the number of available n-type carriers for recombination should increase with temperature due to a lowering of the threshold voltage for injection.

*See (4.10) with χ_0 given by (2.22).

†In the extreme of very low temperatures, charge transport is completely inhibited, thus preventing any current from flowing and therefore producing no EDMR signal. This is opposite to EPR signals, in which low temperatures typically produce much stronger signals.

6.5 Discussion

A major question of interest in the field of spintronics is the extent to which spin-dependent phenomena are involved in charge transport. Previous work suggested that pulsed EDMR signals are attributable to spin blockades formed between like-spin, like-charge polarons, but later efforts showed that the signals observed are equally attributable to recombination currents. Even in unipolar systems, where charge transport is achievable by only one polaron type, the HOMO or LUMO is accessible enough that minority carriers can be injected into the channel.* Though this is a small number relative to the majority carrier, each recombination event would occur between one majority and one minority signal, thus giving both polarons equal importance in the EDMR signal.

By measuring an ambipolar device through all regime of operation, we hope to have clarified the origin of these signals. Comparison of spectra through the p-type linear & saturation, n-type linear & saturation, and ambipolar regimes shows the presence of two Lorentzian contributions. The first is attributed to bipolaron-inhibited transport due to its resonance position, linewidth, and temperature dependence, while the second is likely a recombination signal due to its resonance position and linewidth. Bipolaron-inhibited transport was observed in the saturation regime for both polaron types, but only in the linear regime for hole injection. We attribute this to the fact that polaron charge distribution is smaller at any point in the channel in the saturation regime (vs. the linear regime), thus making travel via percolation more difficult. As a result, polarons are more likely to encounter traps, which manifests as an EDMR signal. No signal is observed in the linear electron-only regime likely because the high mobility and delocalization of the electron wavefunction (as determined in the previous chapter) significantly lowers the probability that mobile electrons encounter trapped electrons.

To corroborate these observations, future work should focus on measuring unipolar systems in which n-type injection is nearly impossible, such as triarylamine-based systems (e.g., PTAA or TFB). In these, minority carrier injection should be so low that recombination currents wouldn't be detectable in EDMR, while bipolaron-inhibited signals would still be clearly visible. This would allow for a more clear distinction between the recombination and bipolaron-inhibited signals observed here.

*Due to the difficulty in handling n-type materials, it's typically the case that unipolar systems are p-type and that the minority carrier is the electron.

CHAPTER 7

SPIN RELAXATION IN ION-GEL-GATED RUBRENE SINGLE CRYSTALS

While the previous two chapters examined relaxation dynamics in comparatively disordered systems, this chapter focuses on crystalline organics. Due to differences in their energetic landscapes and microstructure, these materials often present with different regimes of charge transport — regimes which are similar to that of inorganic semiconductors. Changes in charge transport naturally lead to changes in spin transport, and thus these systems are interesting from a spintronics standpoint as well. In this chapter, we present ESR measurements on a model small-molecule, crystalline system gated with an ion gel to explore different regimes of relaxation dynamics. In contrast to previous measurements on other molecular and polymer semiconductors, we observe very long spin relaxation times — on the order of microseconds — from 15 to 290 K. This is enabled by motional narrowing induced by the rapid transient localization motion of carriers. We also observe the onset of spin-spin dipolar interactions at carrier concentrations approximately greater than $3\times10^{12}\text{cm}^{-2}$.

7.1 Introduction

Rubrene holds the distinction of having the highest mobility among the organic semiconductors, achieving a value of 20-40 cm^2/Vs when in its single crystal form.[80–82] Understandably, this has garnered much attention over the past two decades, both for modeling it as a system by which to compare other organics and in fully understanding the microscopic mechanisms that allow for such inimitable performance. In rubrene and other molecular crystals, charge transport can be interpreted via the theory of transient localization, which describes the effects of dynamic disorder in the electronic structure due to thermal lattice vibrations: charge carriers transiently localize in their dynamic landscape on timescales shorter than typically 100 femtoseconds, but undergo diffusive motion on longer timescales as the molecular lattice evolves.[11] Though the theory is concerned primarily with predictions of *charge* transport (such as a mobility that decreases with increasing temperature — just as in inorganic, band systems), its implications for spin transport are naturally of interest. After all, numerous studies have already used FI-ESR — a direct probe of spins — to establish intricate links between charge and spin dynamics in organic FETs.[45,22,47,25,26,62,24,44,23,46,35,15,83,84,42,85,49,41,86,87,48,88]

Recent work on the thiophene-based molecular crystal C10-DNBDT-NW observed a momentum-scattering relaxation mechanism that limited spin lifetimes to fewer than 100 nanoseconds at room temperature.[89] The mechanism, known as Elliot-Yafet relaxation, is common in inorganics due to the electronic band transport of charges, and shares characteristics similar to the high-temperature relaxation observed in less-ordered polymeric systems.[15] Specifically, though the relaxation pathways in C10-DNBDT-NW and other molecular semiconductors differ from those in conjugated polymers (momentum vs. spatial scattering), they result in a similar decrease in relaxation times with increasing temperature. At the same time, the two types of organic semiconductors have also both been shown to exhibit motional narrowing in the intermediate temperature regime.[15,45,22,47,24,44,23] In either case (molecular crystals vs. conjugated polymers), the intermediate- and high-temperature relaxation mechanisms are at odds: While spatial/momentum scattering shortens relaxation times, motional narrowing increases them by allowing fast-moving charges to average-out local variations in magnetic field environments. Because both mechanisms often occur within the same system, and because both link charge motion to spin relaxation, the question naturally arises of what type of charge transport is most conducive to long spin lifetimes, or, in other words, how can scattering be reduced and motional narrowing enhanced in order to achieve long relaxation times even at room temperature?

Regardless of the detailed mechanisms at play, the scattering/high-temperature relaxation processes observed in both C10-DNBDT-NW and in conjugated polymers are modulated by spin-orbit interactions.* Therefore, to reduce the strength of spin-orbit couplings and achieve longer spin lifetimes, it is interesting to investigate pure hydrocarbon-based molecules — such as rubrene single crystals — where these interactions are weak. However, temperature-dependent FI-ESR measurements in molecular crystals are often experimentally challenging: large crystals are required in order to inject the minimum number of spins detectable in ESR, yet such large crystals have a tendency to break under thermal strain. Here, we use ion gels as a gate dielectric to solve this problem. By using them in lieu of the traditional silicon oxide or polymer dielectrics, capacitances on the order of 1-100 μFcm^{-2} are achievable,[90–95] and this corresponds to injection efficiencies of up to 10^{14} charges/cm^2 at low applied voltages ($\sim$ 1 V) — well above the ESR detection threshold even for a crystal with an area of approximately one square millimeter.

In this chapter, we report a systematic study of spin relaxation times in rubrene single crystals as a function of gate voltage and temperature to probe charge and spin dynamics. We show that, at relatively low carrier concentrations (below approximately 2.5×10^{19} cm^{-3}), relaxation is determined entirely by the fast transient localization of spins in their individual ionic potential wells, and that this leads to surprisingly long spin lifetimes: on the order of microseconds from 4 K all the way to room temperature. At higher carrier concentrations, however, we observe a slight shortening of spin lifetimes, which we ascribe to an onset of spin-spin interactions.

*In the case of momentum scattering, spin-orbit coupling allows electrons to change their spin state when moving within the band structure. In the case of spatial scattering, spin-orbit coupling mixes spin states of π- and σ-orbitals, meaning transfer integrals become spin-dependent.

7.2 Experimental Design

7.2.1 Methods

Rubrene single crystals were grown by the physical vapor transport method[96] using a horizontal tube furnace. Rubrene powders (from Sigma-Aldrich) were placed in a ceramic boat that was then loaded into a quartz tube and placed at the center of the furnace (the hottest region). With a furnace temperature of 290° C and an argon gas flow rate of 50 sccm, rubrene single crystals were collected after a growth time of 10-20 hours. Only those crystals with molecularly smooth surfaces (judged by eye based on previous experience) were used for device fabrication. See Figure 7.1(c) for an optical image of a crystal grown under identical conditions to the ones used here.

The top of Figure 7.1(a) shows a schematic of the device structure used. Two parallel gold electrodes (gold rectangles) were evaporated onto one side of a 40 x 3 mm^2 fused-quartz plate (UQG Optics, FQP-5005) (translucent blue-grey rectangle). A single rubrene crystal (orange rectangle) of approximate dimensions 10 x 1 mm^2 was gently placed onto the glass so as to overlay with one of the electrodes, then affixed with a small drop of silver paint. A thin slice of an ion gel composed of the ionic liquid 1-Butyl-1-methylpyrrolidinium bis(trifluoromethylsulfonyl)imide ([BMP][TFSI]) and the polymer Poly(vinylidene fluoride-co-hexafluoropropylene) (PVDF-HFP) (translucent grey rectangle) was then placed onto the device so that it connected the top of the rubrene to the second electrode. This created a capacitance architecture. We chose this design because it allowed us to measured a single, as-large-as-possible rubrene crystal inside the cavity and protected the devices from degradation under thermal stress. Of course, it presented the disadvantage that we were unable to directly measure FET mobilities during the ESR measurements. To address this and show that our results are generalizable to thin-crystal devices as well, we fabricated electric double-layer transistors (EDLTs) with the same materials and under identical processing conditions to obtain comparable FET mobility measurements. These measurements, which were limited to room temperature, are presented in Figure 7.5.

The bottom of Figure 7.1(a) shows an actual capacitance device that was measured. The sample is attached to the sample holder via double-sided Kapton tape. The three contact strips on the holder are clearly visible, as are the soldering joints that affix the wires that lead to the Keithley 2602B SourceMeter. Note that, due to the device architecture, only two of the three contact pads were used; these were wire-bonded to the two electrodes on the device. The silver dag was used to prevent the wire from breaking off (due to thermal strain) the contact pads and/or the electrodes. The small piece of silver dag on the rubrene was needed to adhere the rubrene to the substrate because the adhesion between only the substrate and the rubrene was not sufficient.

The device was loaded into the spectrometer setup as follows: After affixing the sample to the sample holder, the contact pads of the sample were wire-bonded to the contact strips of the holder using aluminium thread. The sample-and-holder combination was then slid into a Wilmad Suprasil EPR tube (Sigma-Aldritch, product no. Z5674XX) and sealed under nitrogen. The sample was then loaded into an Oxford Instruments ESR900 cryostat, which was controlled by an Oxford Instruments Mercury iTC.

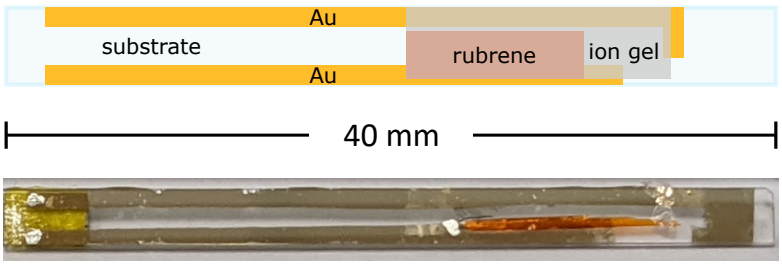

(a)

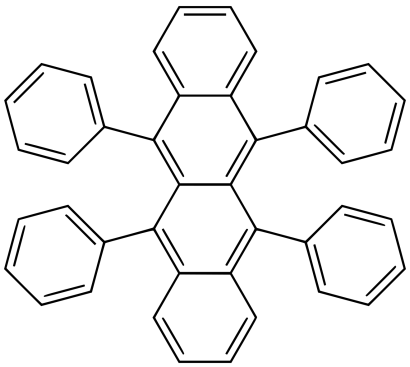

(b)

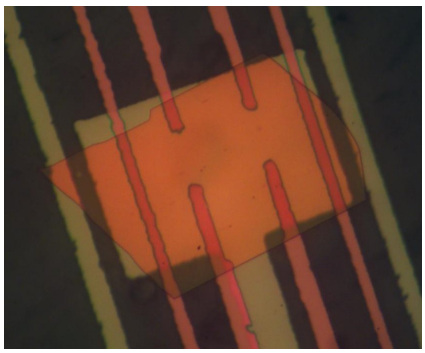

(c)

Fig. 7.1 **(a)** A schematic of the capacitor architecture (top) and an image of an actual device (bottom). In the schematic, the gold rectangles are electrodes, the orange rectangle rubrene, the dark grey rectangle the ion gel, and the large, translucent blue rectangle the substrate. **(b)** The chemical structure of rubrene. **(c)** An optical image of a rubrene crystal used for our EDLT measurements. The sample was grown under conditions identical to those used for our capacitor devices.

ESR measurements were taken on a Bruker E500 spectrometer using a Bruker ER 4122SHQE cavity and an X-band microwave source, and a Keithley 2602b source unit was used for electrical characterization. CustomXepr, a Python package developed by Sam Schott, was used to integrate the above-mentioned instruments and automate measurements when desired.[15]

7.2.2 Experimenter contributions

The author designed the experiment, helped fabricate devices, collected data, and analyzed and interpreted results. Xinglong Ren, in equal contribution, helped design the experiment, designed most of the devices, and analyzed and interpreted data. Sam Schott provided useful insights in the interpretation of the data, and Henning Sirringhaus helped design the experiment and interpret the data.

7.3 Results & Analyses

A typical resonance signal is shown in Figure 7.2(a). Based on previous work, the extracted g-factor of 2.0024 confirms injection of hole polarons from the rubrene into the channel.[47,87,84] Initial measurements showed a very narrow peak-to-peak linewidth of approximately 0.05 G, meaning artifactless spectra

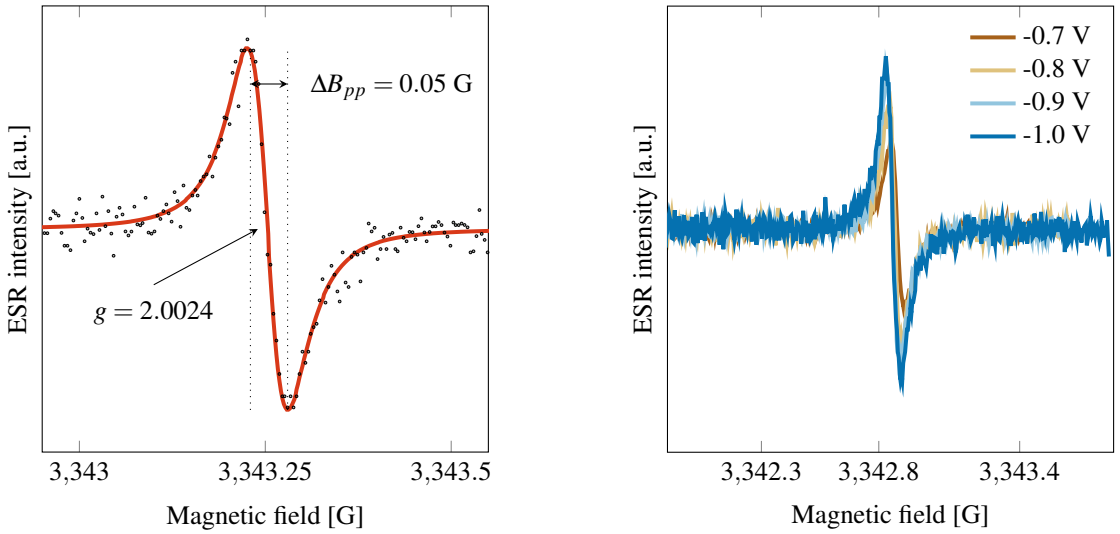

Fig. 7.2 **(a)** A representative ESR spectrum at bias voltage -1.2 V and temperature 290 K. **(b)** The evolution of the observed ESR signal with increasing gate voltage.

could only be obtained by measuring with a modulation amplitude of 0.02 G and a modulation frequency of 50 kHz (see Section 4.4 and Subsection 4.6.2, respectively). Because the injection efficiency of ion gels varies with sample dimensions, the minimum voltage at which a signal could be observed varied across samples; the range of observed minimum values was +0.4 V to -0.6 V.

Though the double-integrated intensity of the spectra (and therefore number of injected spins) grew with the magnitude of bias voltage applied (shown in Figure 7.2(b)), we do not report data for gate voltages $V_g < -1.5$ V. This because we observed a second ESR resonance signal develop in preliminary samples when measuring at high gate voltages. Because we ascribe this to an electrochemical process involving the rubrene and the ions in the ionic liquid and/or other electrochemical species, we believed such a process could interfere with spin lifetimes. Thus, we only recorded measurements in which we were sure no such reaction took place.

7.3.1 Fast transport: the dependence of relaxation times on temperature

Transverse (T_2) and longitudinal (T_1) relaxation times were measured via the method of power saturation (representative spectra are shown in Figure 7.3(a) for a sample at room temperature and -1.0 V; see Subsection 4.5.2). Figure 7.3(b) and Figure 7.3(c) show the extracted relaxation times for a device held at -1.5 V and at -0.4 V respectively, while those of a third device are shown in Appendix D. Plotted in all three figures are T_1, T_2, and the coherence time, $T_2' \equiv (1/T_2 - 1/2T_1)^{-1}$. We see that relaxation times are remarkably long: on the order of microseconds across the entire temperature range, including room temperature. In all samples, T_2 is slightly shorter than T_1 and increases monotonically with increasing temperature. T_1 exhibits a similar temperature dependence, except at very low temperatures and near room temperature, where it may decrease slightly.

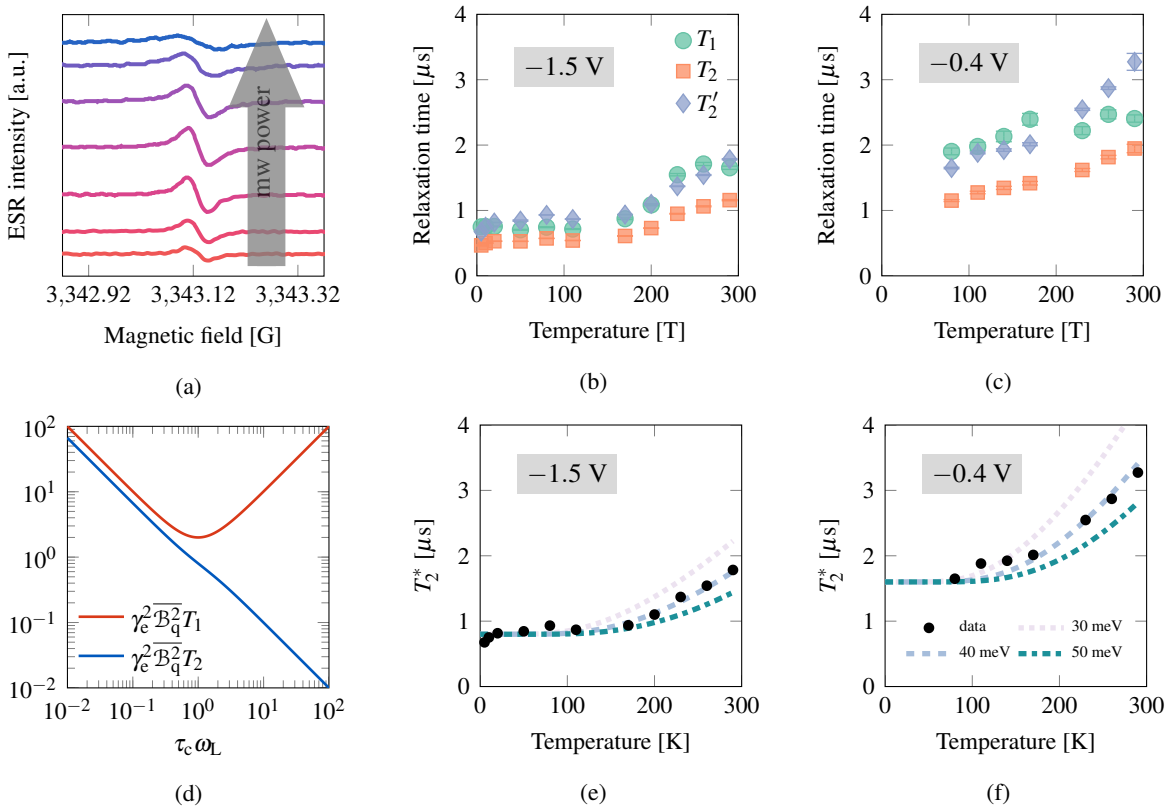

Fig. 7.3 **(a)** Power saturation measurements recorded at -1.0 V and 290 K. The extracted T_1 and T_2 are plotted in **(b)** for a rubrene ion-gel-gated capacitor at -1.5 V and in **(c)** for a second device at -0.4 V. **(d)** Normalized T_1 and T_2 as a function of correlation time in the motional narrowing regime according to (7.1). (Adapted from Slichter (1963).[38]) **(e)** and **(f)** Calculated coherence times for the -1.5 V and -0.4 V condition alongside estimated values using the functional form of ν from (7.2) with different activation energies (30, 40, and 50 meV).

This behavior differs starkly from that observed in our recent FI-ESR studies on high-mobility conjugated polymers. First, in those systems we observed orders-of-magnitude changes in T_1 and T_2 as a function of temperature. As a result, T_1 typically approached one microsecond only below 150 K, while T_2 often required us to go below 50 K. Second, while T_2 did show an increase with temperature in the conjugated polymers, this motional narrowing effect was observable only between roughly 100 and 200 K, quite different than the entire temperature range covered here. Finally, and perhaps most significantly, T_1 here *increases* rather than decreases with temperature — directly opposite to not only the behavior observed in our polymer systems, but also to that observed in the recent FI-ESR study on thin films of C10-DNBDT-NW gated by a polymer dielectric.[89] Consequently, our room-temperature spin relaxation times are 10-100 times longer than in typical polymer systems or in C10-DNBDT-NW, and 1000 times longer than in many inorganic systems[97–99] or graphene.[100]

Though the increase in T_2 with temperature is a well-known effect of motional narrowing, the corresponding increase in T_1 has not been observed before in organic semiconductors. To understand this remarkable behavior, we note from Subsection 2.3.1 that the behavior of T_1 and T_2 in the motional

narrowing regime (as predicted by the Redfield equations) is

$$\begin{aligned}\frac{1}{T_1} &= \gamma_e^2\left(\overline{\mathcal{B}_x^2}+\overline{\mathcal{B}_y^2}\right)\frac{\tau_c}{1+\omega_L^2\tau_c^2}\\ \frac{1}{T_2} &= \frac{1}{2T_1}+\gamma_e^2\overline{\mathcal{B}_z^2}\tau_c\\ \frac{1}{T_2'} &\equiv \frac{1}{T_2}-\frac{1}{2T_1}=\gamma_e^2\mathcal{B}_{rms}^2\tau_c,\end{aligned} \tag{7.1}$$

Figure 7.3(d), which is identical to Figure 2.9 from Chapter 2 but reproduced here for quick reference, illustrates schematically how this T_1 and T_2 vary as a function of the correlation time (normalized by the Larmor frequency). We see that T_1 relaxation is most effective when the correlation time matches the Larmor period, and becomes less effective as the correlation increases or decreases. This is simply because spin-flips require a change of energy with the lattice, and therefore must be induced by a photon of energy ω_L (just like in resonance experiments).* T_1 is minimized when the correlation time equals the period of the Larmor field, i.e., $\tau_c = 1/\omega_L$, and increases as τ_c moves away from this value. Because τ_c is interpreted as the inverse hopping frequency, an increase in temperature essentially corresponds to moving from right to left in Figure 7.3(d) for systems in which transport is temperature-activated. In our previous experiments on temperature-activated polymers, we were in the regime to the right of the minimum, where we observed a decrease in T_1 and an increase in T_2 as we increased temperature. However, in our ion-gel-gated rubrene crystals, in which charge transport is also activated with temperature,[101] the microscopic charge motion seems to be sufficiently fast that we can enter the regime to the left of the minimum, where both T_1 and T_2 increase as the charge motion becomes faster at higher temperatures.

While this qualitative behavior matches that of the data, we can also examine how well the equations quantitatively predict it by plotting T_2^* from (7.1) as a function of temperature. To do so, we must determine $\mathcal{B}_{rms}$ and $\tau_c(T)$. The former can be approximated by noting that, according to Figure 7.3(d), the minimum in T_1 occurs when $\tau_c = 1/\omega_L$, which is approximately 17 ps in this case. The minimum can be seen in the data for the $V_g = -1$ V and -1.5 V plots at around 100 K, where $T_2^* = 0.95\,\mu$s (from $1/T_2 - 1/2T_1$). We therefore have at 100 K that $(0.95\ \mu\text{s})^{-1} = \gamma_e^2\mathcal{B}_{rms}^2 \times$ 17 ps, which yields $\mathcal{B}_{rms} \approx 1.4$ G.

To now determine $\tau_c(T)$, we recall from Subsection 2.3.1 that it can be interpreted as the inverse hopping frequency ν in the regime of motional narrowing (which is the regime of relaxation in the data from approximately 15 to 269 K). The Einstein relation for drift then relates mobility and hopping frequency via $\mu = q\overline{R}^2\nu/k_BT$, where $\overline{R}$ is the average hopping distance. Further, charge motion in ion-gel-gated transistors is thermally activated, following specifically the Arrhenius expression

*T_2, meanwhile, can be relaxed by spin-flips (though each flip is only half as effective here), or by pure decoherence. Motional narrowing occurs when faster charge motion reduces the correlation time, thus allowing all spins to sample the same magnetic environment on average and therefore increasing the spin lifetime. As a result, the hopping frequency ν is typically interpreted as the inverse correlation time in this regime.[15]

$\propto \exp[-E_A/k_B T]$.[102,103] From these two relations, we find the temperature dependence of the hopping frequency and, by its inverse, the correlation time: $\nu(T) \propto T\exp[-E_A/k_B T]$.

For most temperatures, this provides a reasonable estimate of T_*' as a function of temperature via (7.1). However, we also include an additional constant (i.e., temperature-independent term) in the fitted expression. This is reflecting the contribution from the fast local motion of carriers due to transient localization, which is superimposed on the slower hopping of charges between local regions defined by the potentials created by the ions on the surface of the rubrene crystal. Assuming that its contribution is independent of temperature is an approximation and a refined analysis should take the actual temperature dependence of transient localization motion into account. However, in comparison, the thermally activated term, which is meant to reflect mainly the transport of charges between different local traps within ionic potentials, is expected to dominate the temperature dependence. We therefore write

$$T_2' = A \times T\exp\left[\frac{-E_A}{k_B T}\right] + C. \tag{7.2}$$

The T_2's resulting from this expression (via Figure 3.3) are plotted with the data in Figure 7.3(e) and Figure 7.3(f) for three different values of E_A. For the plots, we absorbed γ_e and $\mathcal{B}_{rms}$ into the constants of proportionality. For the -1.5 (main text), -0.4 (main text), and -1.0 V (Appendix D) curves, the values of best fit were $A = 17$, 26, and 73 ns, and $C = 0.8$, 1.8, and 0.9 μs, respectively.

We see from this figure that an activation energy of 40 meV fits the data well (though the fits are sensitive to constants of proportionality), which is a reasonable estimate based off the work of Xie et al. (2014) on ion-gel-gated rubrene.[103] This demonstrates that the Redfield model well explains the *increase* in T_1 with temperature. To our knowledge, this is the first observation of this behavior in organic semiconductors.

We now discuss how we are able to achieve this relaxation behavior in our system, and why our results differ from those previously reported by us on conjugated polymers[15] and by Tsurumi et al. (2017) on C10-DNBDT-NW.[89] Addressing the conjugated polymers first, we note that the highest mobility polymer system, the indacenodithiophene-co-benzothiadiazole copolymer IDT-BT, had an estimated motion frequency in the motional narrowing regime of 10 GHz. Comparing this value to $1/\omega_L \approx 17$ ps, we conclude that it would need to be 100 times larger to reach the T_1 minimum. Because the measured mobility (at 150 K) for IDTBT was 0.1 cm^2/Vs, this suggests that mobilities on the order of 10 cm^2/Vs are necessary to achieve this. While we do not record such high bulk mobilities on an electric double-layer transistor (EDLT, see below), we note that such high mobilities are not unreasonable at the local scale, where charge motion should be similar to that of rubrene single crystals without ions. In other words, our estimates of mobility in the EDLT are measurements of long-range transport, which are likely to be affected by electrostatic potential fluctuations created by ions in the gel. The measured mobility values may greatly underestimate local transport. It is this local transport, however, that our relaxation times reflect.

Turning to the crystalline systems that contain relatively heavy sulfur atoms,[89] we note there that Elliot-Yafet scattering is driven by the spin-orbit interaction. Here, in our ion-gel-gated rubrene, not only

is the strength of spin-orbit coupling weaker, but the presence of long-range electrostatic potentials means we do not enter the delocalized, band-like transport regime required for Elliot-Yafet relaxation. Our interpretation is that the very weak spin relaxation in our systems reflects effective motional narrowing induced by fast transient localization of the carriers at the local level, i.e. within the local regions to which motion is confined by the long-range electrostatic potential fluctuations induced by the ions. The main effect of temperature is that it allows charges to leave these local regions, therefore making motional narrowing even more effective. This interpretation is consistent with the motion frequencies in Figure 7.3(e) and Figure 7.3(f) becoming constant, but remaining high at temperatures below 100 K.

7.3.2 Spin-spin interactions: the dependence of T_2 on bias voltage

We next investigated the behavior of T_2 with gate voltage at 290 K. The top row of Figure 7.4 shows the dependence of the transverse relaxation time (inversely proportional to the peak-to-peak linewidth) on bias voltage for three devices. The microsecond-long relaxation times ($\sim 1\ \mu$s) at room temperature are consistent with Takahashi et al.'s (2013) work[84] and the data presented in the previous section. In all devices we observed a distinct peak of T_2 as a function of bias voltage. Though the difference between the longest relaxation time (at the peak) and that of the smallest observable signal is small (their ratio is typically 1.1), the behavior is both reproducible and outside the bounds of measurement error. We make the case that it is attributable to the onset of spin-spin dipolar interactions, which result in increased spin relaxation at high carrier concentrations.

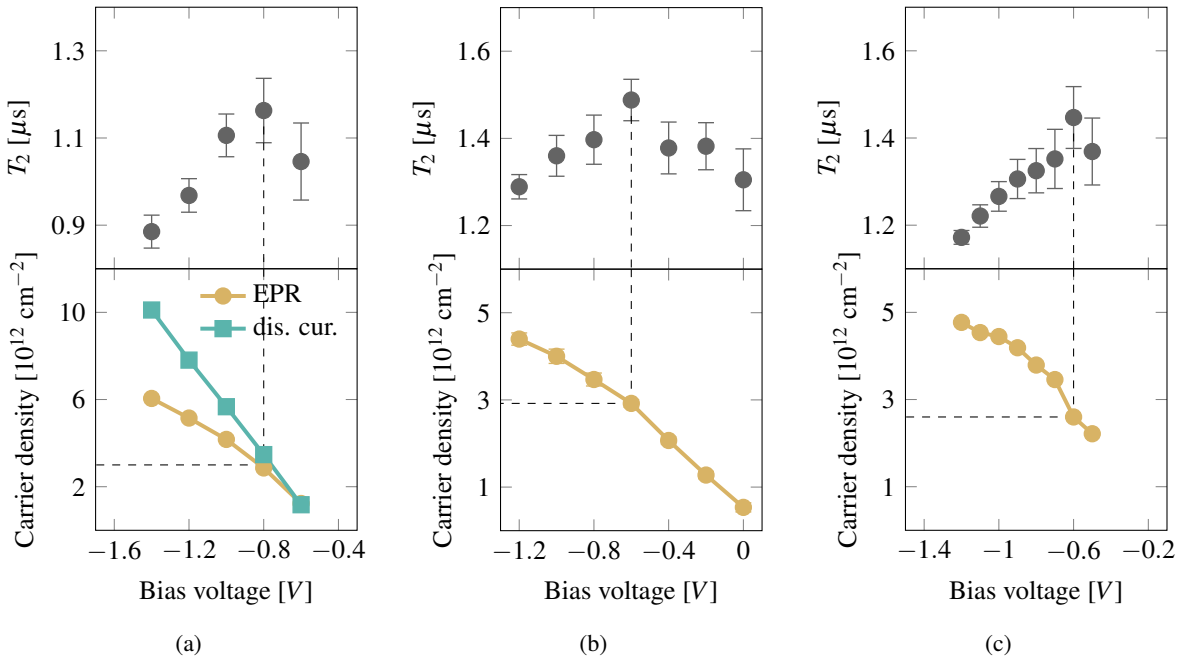

Fig. 7.4 T_2 and carrier density vs. gate voltage in three devices (top). Because all lineshapes were Lorentzian and the signal was not saturated, T_2 was calculated from the inverse of the half-width-at-half-height $\Delta B_{1/2}$ of the ESR signal. For device **(a)**, both the ESR-extracted carrier concentration and that of the displacement current are shown. A maximum in T_2 occurs at an area concentration of about 3×10^{12} spins/cm^2.

In the lower row of Figure 7.4 we show the corresponding plots of carrier concentration for the same three devices. In the right two, the number of spins calculated from EPR is plotted (see Subsection 4.5.1), while in the leftmost column we plot both the EPR-extracted carrier concentration and that of the displacement current. (Measurements of the displacement current are taken by recording an I_g vs. V_g curve for different sweep rates, integrating the result, and dividing by the sweep rate.[104,103]) Across all three samples we observe an increase of carrier concentration with more negative bias voltages. More importantly, we see that the peak in T_2 corresponds to a carrier concentration just under 3.0 $\times 10^{12}$ charges/cm^2: 2.86, 2.29, and 2.92 $\times 10^{12}$ charges/cm^2 in device 1, 2, and 3, respectively.* Though values of the displacement-current-extracted carrier concentration diverge from those of EPR at more extreme voltages, they coincide at this value. We attribute the divergence to an overestimate by the displacement current method due to increased gate leakage at higher gate voltages, or to an underestimate of the ESR-extracted value due to anti-aligned spin pairs at high carrier concentrations.

Before proposing a model to explain these results, we show here that the Redfield equations from the previous section are insufficient. Of course, because T_1 and T_2 begin to decrease at 290 K (where the data presented in this section was recorded) in the -1.5 V and -1.0 V devices, it may be unfair to expect the Redfield equations to be accurate here. However, the -0.4 V device still shows a peak in T_2 at room temperature, while T_1 may be increasing within error. Because the observed peaks in T_2 shown in Figure 7.4 occur before -1.0 V, we make the comparison against the Redfield equations to be thorough.

From the expression for T_2 in (7.1), it is clear that a process creating a peak in hopping frequency would be required to explain a peak in the transverse relaxation time. If there were such a process it might also be reflected in the measured mobility at the same carrier concentration. To test for this possibility in our devices, we performed electrical and ESR measurements on a rubrene single crystal EDLT that was fabricated under conditions similar to those used for our capacitance devices. For the dielectric we used the same ion gel, and for the gate we used platinum electrodes on a polyethylene terephthalate (PET) substrate. Figure 7.5(a) shows the resulting transverse relaxation time and spin concentration (per unit area) as a function of gate voltage. For this device we see that the peak in T_2 occurs at $V_g = -0.3$ V, which corresponds to a carrier concentration of 2.5×10^{12} cm^{-2}. However, the corresponding transfer characteristics of the EDLT (Figure 7.5(b)) shows no peak in the current I_{sd} around this value. Moreover, by extracting mobilities from this data via

$$\mu = \frac{L}{W}\frac{I_d}{qN_{spin}V_d} \tag{7.3}$$

(where L and W are the channel length and width, respectively),[104] we show in the inset that there is also not a peak in μ around this voltage. We therefore conclude that a peak in the hopping frequency is not responsible for the peak in T_2 under changing gate voltage. We do note that a peak in conductance and mobility has been observed in similar EDLT devices previously,[101] but this occurred only at carrier concentrations significantly higher than used here (greater than 10^{13} cm^{-2}).

*We assume a thickness of 1 nm for the accumulation layer, meaning the corresponding volume concentrations are on the order of 10^{19} charges/cm^3.

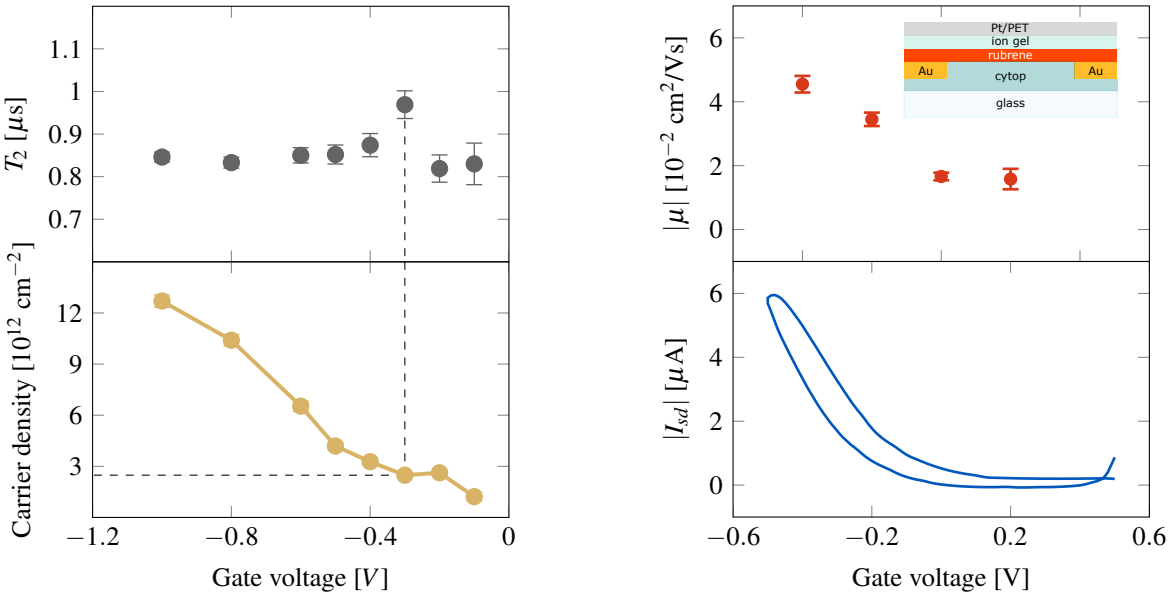

(a) (b)

Fig. 7.5 Measurements on a rubrene EDLT. **(a)** Top: T_2 vs. applied gate voltage; a peak in T_2 is observed at $V_g = -0.2$ V. Bottom: The extracted spin concentration (per unit area) at the same voltage values. **(b)** The transfer curve (bottom, $V_\mathrm{d} = -0.1$ V) and corresponding mobilities (top) of the same device before ESR scans were taken. Mobilities are only reported at gate voltages for which we estimated the number of spins via ESR. Inset: a schematic of the EDLT architecture.

7.3.3 Modeling the dipolar interaction

As an alternative explanation, we propose that the peak in T_2 is caused by the onset of spin-spin dipolar interactions. For a simple order-of-magnitude estimate of whether such interactions may be observable at these carrier concentrations, and for an understanding of the factors to which the dipolar interaction may be sensitive, we make use of a model developed by Abragam (1961).[54]

To begin, we recall from the theory derived in Subsection 2.3.1 that the 'fast fluctuations' regime gives the following master equation to describe the evolution of the density matrix under some perturbing Hamiltonian $\mathcal{H}$

$$\frac{\mathrm{d}\rho'_{nn'}}{\mathrm{d}t} = \sum_{m,m'} R_{nn'mm'} \exp\left[\frac{i(E_n - E_{n'} - E_m + E_{m'})t}{\hbar}\right] \rho'_{mm'}, \tag{7.4}$$

where the explicit form of the Hamiltonian is included in the components $R_{nn'mm'}$.*

In that section, the form of the Zeeman interaction was assumed for the perturbing Hamiltonian, i.e., $\mathcal{H} \propto \mathbf{S} \cdot \mathbf{B}$. Here, we propose instead to assume the form of the dipolar interaction. Rather than writing it classically in Cartesian coordinates, we note that, most generally, any spin-spin interaction can be

*Though the exact theoretical derivation is important, it is not expounded upon the text in order to avoid confusing the reader. For the keen bean: the Hamiltonian is explicitly written in the correlation functions $G_{nmn'm'}(\tau)$ (see (2.45)), $G_{nmn'm'}(\tau)$ is explicitly written in the spectral densities $J_{nn'mm'}(\omega)$ (see (2.46)), and $J_{nn'mm'}(\omega)$ is explicitly written in the we're-running-out-of-names-for-all-these-terms $R_{nn'mm'}$ (see (2.49)).

expressed in terms of two operators: one that acts on the relative position of the two spins involved, and a second that acts on their spin components. Because we are concerned with interactions between two spins, these two operators are tensors of the second rank. We thus label the lattice operator $F_k^{(2)}$ and the spin operator $\mathscr{S}_k^{(2)}$, where we have chosen to work in spherical harmonic coordinates rather than Cartesian ones, meaning the index k runs over linear combinations of the Cartesian components. (See Appendix C for a review of the spherical tensor basis, as well as conversions between the Cartesian and spherical basis.) The perturbing Hamiltonian is then written as

$$\mathcal{H}_1 = \sum_k F_k^{(2)} \mathscr{S}_k^{(2)}. \tag{7.5}$$

Abragam showed that, after evaluating over the spin coordinates,* the longitudinal and transverse relaxation times are directly proportional to the components of the position function $F_k^{(2)}$. Selecting a form for the position function, Abragam considered the case of liquid and gas nuclear magnetic resonance, wherein spin-carrying molecules translate past each other and undergo a diffusive process described by a diffusion current density. For our work here, we note that the polarons accumulated in FI-ESR are subject only to drift processes unless a source-drain voltage is applied. We therefore choose our diffusive process to be described by the diffusion current density $\mathbf{j}$,

$$\mathbf{j} = qD\nabla n, \tag{7.6}$$

where q is the fundamental electric charge, n is the carrier density, and D the diffusion constant. We note that the diffusion coefficient is that of charge carriers/spins and can be expressed in terms of the carrier mobility using the Einstein relation $D = \mu k_B T/q$. Based on our measurements of the bulk mobility in the EDLT, we estimate the hole mobility to be between 0.01 and 0.1 cm^2/Vs. We attribute this low value in our devices (compared to the work of Xie and Frisbie (2011)[104]) to an increased access resistance from the crystal thickness due to the top-gate, bottom-contact architecture used. (See the discussion below regarding why our mobility in this section is lower than that used in Subsection 7.3.1.)

Abragam's analysis on rigid spheres in NMR assumed a minimum distance of approach d equal to twice the radius of the spheres. Here, we crudely take this minimum distance to be defined by the spatial extent of the hole wavefunction, i.e., two holes may touch, but do not overlap. Referring to the work of Giannini and Blumberger (2022),[105] who used quantum-classical nonadiabatic molecular dynamics to estimate polaron mobilities and inverse participation rates (IPRs) in several organic semiconductors, we estimate the 1D polaron delocalization length (and thus minimum distance of approach) in rubrene to be approximately 5-6 nm. The spectral density consequently loses its dependence on ω because it is so

*Again, the details are omitted in the main text to avoid unnecessarily confusing the reader. They are as follows: The Bloch equations are recovered by finding the dynamics of magnetization, which are dictated by the time evolution of the density matrix (see (2.34)). The time evolution of the density matrix is found via equation (7.4), which includes the Hamiltonian through $R_{nn'mm'}$ (see the previous footnote). Thus, 'Abragam showed' means that he went through all of that effort and simplified.

small, and we thus have for the relaxation times

$$\begin{aligned}\frac{1}{T_1} &= \frac{3}{2}\frac{\mu_0^2}{16\pi^2}\gamma^4\hbar^2 S(S+1)\frac{16\pi}{45}\frac{n}{dD} \\ \frac{1}{T_2} &= \frac{\mu_0^2}{16\pi^2}\gamma^4\hbar^2 S(S+1)\frac{8\pi}{15}\frac{n}{dD}.\end{aligned} \tag{7.7}$$

Using the values $n = 2.8 \times 10^{19}$ spins/cm^3, $d = 5$ nm, and $T = 290$ K, as well as a range of mobility between 0.01 and 0.1 cm^2/Vs, we obtain an estimate for T_2 between 33 and 330 μs. The model therefore overestimates T_2 by 1-2 orders of magnitude. Given its simplicity, this may not be unreasonable. Estimating the minimum distance is complicated by the rapid temporal fluctuations of the charge wavefunctions, which is a process characteristic of the transient localization regime, but neglected in the model. Furthermore, the diffusion in our system is restricted to two dimensions in the accumulation layer rather than three — as assumed in the model — and this is likely to lead to an underestimate of the rate at which spins experience close encounters. The peak in T_2 can be explained by noting that it increases with the minimum distance of approach (via weaker dipolar interactions) and polaron mobility (via increased motional narrowing), while it decreases with carrier concentration (via more frequent dipolar interactions). At low bias, mobility increases sharply with voltage, and this leads to more effective motional narrowing of the linewidth with increasing gate voltage. At higher bias, however, the increased carrier concentration pushes charges closer together, thus resulting in them being relaxed by dipolar coupling more strongly. It is the interplay between this gate-voltage dependence of mobility and carrier concentration that leads to the observed peak.

Finally, we wish to discuss the use of a relatively low mobility here (between 0.01 and 0.1 cm^2/Vs) versus a higher mobility ($\sim$ 10 cm^2/Vs) in Subsection 7.3.1 to explain the temperature-dependent data. When considering the case of relaxation driven by local fluctuations due to the hyperfine interaction, a single electron need not leave its local region, which in the case of our ion-gel-gated devices is defined by the ionic potentials. Within a single potential well, an electron can sample — by means of transient localization — many different hyperfine fields. Though this high-frequency motion is not reflected in device mobility measurements — which are limited by the processes that involve escaping from local potential wells defined by the ions — they enable effective motional narrowing and *are* captured by ESR measurements. Thus, the motion frequency relevant for hyperfine-driven relaxation is this faster, local hopping. In the case of relaxation by dipolar coupling, however, the picture changes, as a polaron must leave its local potential in order to interact with a neighboring spin. In this case, it is therefore the lower device mobility that is relevant.

7.4 Discussion

We have presented a systematic study of the spin relaxation of charge carriers in ion-gel-gated rubrene single crystals. These devices exhibit remarkably long spin lifetimes — on the order of microseconds — from 15 K all the way to 290 K. We showed that such extraordinary behavior is possible because charges

are able to move quickly enough that they avoid relaxation by transverse fields. Interestingly, though this occurs at all gate voltages measured, it seems most effective at lower voltages, where relaxation times are nearly independent of temperature down to at least 80 K. We hypothesize that larger voltages impose larger energetic fluctuations experienced by charge carriers on the surface of the crystal, a possibility consistent with previous observations on rubrene EDLTs. To our knowledge, this is the first observation in organic semiconductors of this regime where T_1 and T_2 increase in tandem as charge motion becomes faster. Due to the fast hopping frequency required, it may come as no surprise that rubrene is the first system in which it has been detected.

By measuring the evolution of the linewidth with gate voltage at room temperature, we reproducibly observed a peak in T_2 when injected carrier concentrations were approximately just below 3×10^{12} charges/cm^2. By adapting Abragam's model for translational diffusion in fluid NMR, we explained this as due to an interplay between a gate-voltage-dependent carrier mobility and a spin-spin interaction resulting from high carrier concentrations. Of particular note is that relaxation driven by these dipolar interactions is modulated by slow inter-ionic-potential transport, while relaxation driven by local hyperfine fields is modulated by the fast transient localization motion occurring within each potential well.

Our work provides new insight into the spin relaxation physics of high-mobility molecular crystals with low spin-orbit coupling. It demonstrates that exceptionally long spin relaxation times are achievable even at room temperature in a regime in which fast transient localization motion of spins gives rise to effective motional narrowing.

CHAPTER 8

CONCLUSION

Though the subject of organic spintronics is still young, a great deal of research has already revealed new, exciting, and impactful physics in the field. Spintronics on its own offers technical advances such as reduced heat waste and non-volatile memory in the form of magnetic random-access memory (MRAM) and quantum computing. Organics, on the other hand, offer low-cost and large-scale manufacturing, flexible circuitry, and functional tunability. The great advantage when combining them, as we have shown in this thesis, is the deep, intimate relationship between charge and spin dynamics. Resulting in a host of spin-related transport phenomena — the anomalous Hall effect, the spin Hall effect, the inverse spin Hall effect, the quantum Hall effect, and organic magnetoresistance, just to name a few — the charge-spin interplay in these systems has implications for device design for spin valves, spin optics, and classical and quantum computing. Of course, a few laboratory prototypes have already shown these devices to be viable, so from that perspective the remaining work may simply seem to be a matter of engineering. However, this is not the case, as further development requires not just large-scale manufacturing, but also an understanding of bulk, surface, and interface effects that may not be present in proof-of-concept devices. The field is still young, and much research remains before we will see organic spintronic technology as part of everyday life.

Spintronics aside, the charge-transport relationship in these systems allows for a better understanding of charge transport in organic semiconductor devices. Because each charge also carries a spin, we are able to use spin-based measurements to probe both micro- and macroscopic charge dynamics. The utility here is that many electrical characterization techniques are limited to measurements of the bulk, thus missing the fundamental processes that may be occurring on smaller scales and yet have implications for device performance. Field-effect transistors and diodes are two examples of devices that are used in everyday technology and for which spin-based measurements have identified microscopic phenomena affecting macroscopic performance. Photovoltaics is another interesting field, as there not only is charge transport relevant, but spin-based processes fundamentally alter device performance. Special care must be taken when selecting organics for those devices, emphasizing the importance of both charge and spin equally.

Regardless of the application(s), common characteristics of a ‘good’ organic spintronics semiconductor include long spin lifetimes, long spin-diffusion lengths, and modest (if not high) charge mobility.

All three of these processes have been subject to much research, yet they still are not completely understood. Even charge mobility, which has been studied for decades, has competing models that are highly dependent on the system under consideration. Spin lifetimes and spin diffusion, on the other hand, are comparatively more difficult to study, as the mutability of spins gives only short time frames and length scales at which to work. It is naturally of interest to extend these, but before being able to do so we must study them in detail to understand the underlying physics at play. To seek to perform an in-depth characterization of all three phenomena (spin relaxation, spin diffusion, and spin-charge transport) would likely be beyond the scope of a single thesis, and so here we have focused on spin relaxation and transport in general. With respect to the former, much research has already well characterized relaxation and low and intermediate temperatures, yet processes occurring at room temperature — where technology is most likely to operate — remains unexplored; there, we seek not only to understand what processes drive relaxation, but also how we can lengthen spin lifetimes in ideal systems. With respect to the latter, we need to fully identify which spin-dependent electrical processes are relevant in devices under operation, and how they may be modulated to enhance performance.

In an effort to answer these (implied) questions, Chapter 2 and Chapter 3 presented a thorough review of spin resonance experiments and how they can be leveraged to study organic semiconductors. To show how microscopic phenomena may appear in bulk measurements, we focused in particular on the direct transformation from terms in a Hamiltonian to fitting parameters in a spectral signal. We emphasized how initial assumptions are important in understanding observed signals, thus setting the stage for experimental interpretation. Then, to ensure the reader fully understands the care that must be exercised in processing data, Chapter 4 discussed the experimental challenges encountered and procedures involved to properly extract meaningful physics from magnetic resonance experiments.

In Chapter 5 we directly addressed the question of spin relaxation at high temperatures. By using ambipolar systems, we showed exactly how the electron wavefunction is driven to relax by thermally activated nuclear torsion. In fused systems, where the electron and hole wavefunctions are relatively similar, we observed a near-equal onset of spin-shuttling relaxation at high temperatures. In a donor-acceptor system, however, where the two wavefunctions are quite dissimilar, we observed the hole wavefunction undergoing this relaxation at a much higher temperature than its hole counterpart. By comparing our ESR measurements to simulations of charge transport in this system, we identified the most likely link whose torsion drives relaxation. By examining the extent and location of the hole wavefunction, for which spin-shuttling relaxation onsets at a relatively high temperature (200 K), we demonstrated how careful molecular design may lead to reduced relaxation and thus improved device performance. Future work, of course, needs to expand on this research, as our results are not quite direct evidence. Though we showed a difference in relaxation onset and correlated it to wavefunction location, we did not modify the torsional dynamics of the relaxation-driving sites identified, nor were we able to provide simulations of wavefunction localization in the fused systems. These would provide clearer evidence for the case of spin-shuttling, and would likely provide deeper insight into the physics at play.

Chapter 6 moved to the question of spin-dependent charge transport. Though the phenomenon of organic magnetoresistance has been observed for decades, the underlying mechanisms are still debated.

Two popular theories are that of bipolaron-inhibited transport and recombination transport. Though it's possible that both are valid to some degree, the question is to what extent each may be present in different systems, and which structural (electronic or mechanical) parameters are most relevant for each. We answered this by using ambipolar systems, which allowed us to modulate the charge dynamics of the device under operation. By sweeping through different regimes of transport, we showed that both bipolaron-inhibited and recombination signals are observable, though their relative strength is dependent on charge density and wavefunction extent. We observed that holes, which are relatively more localized and undergo slower transport, give EDMR signals regardless of charge density. Electrons, on the other hand, give EDMR signals only when charge density is low, suggesting that the spread of the wavefunction allows it to travel via many percolation paths and therefore avoid blocking sites. Though we found quite strong evidence for the bipolaron-inhibited signal, uniquely identifying the recombination signal was more challenging. Interesting, despite observing it only when the transistor operated in the recombination regime, the signal's g-factor was far removed from that of both electrons and holes. Future work should examine this process in more detail, and it would also be insightful to study in more detail the interplay between charge density, wavefunction extent, and mobility and other systems.

In Chapter 1 we returned to the phenomenon of relaxation — this time in a model system for charge transport: rubrene. After better understanding the processes driving relaxation at high temperatures, both from our work in Chapter 5 and other recent research, we sought to study a system in which high charge transport could be achieved alongside long relaxation times. Because rubrene possesses low spin-orbit coupling and a highly ordered structure that allows for transient localization, it provided the ideal environment in which to work. Remarkably, by gating it with an ion-gel, we minimized the band-like transport typically seen in crystalline molecular systems, which, as a result, reduced the scattering relaxation typically present while retaining a high enough mobility for effective motional narrowing. As a result, we observed microsecond-long relaxation times at room temperature, incredibly stable relaxation times from 5 K to room temperature, and relaxation times that *increased* rather than decreased with temperature. Perhaps of even more interest for some is that we observed the onset of relaxation induced by the spin-spin dipolar interaction, which is typically not observed in organic semiconductors. Though our model to explain this observation is crude, it sets the foundation for more research. Future work should focus in detail on how wavefunction dynamics on femtosecond timescales influence dipolar couplings, and how these may drive relaxation. In addition, it would also be useful to identify the exact means by which the ion-gel is able to reduce band-like transport enough to prevent high-temperature relaxation, yet still maintain transport fast enough to permit motional narrowing. We currently ascribe this to local potential wells created by the ions in the gel, but a more developed understanding would clearly make the link from local transient localization within a well to hopping between wells.

The use of organic-spintronics-based devices in everyday life still remains a long way off. Several major physical processes still remain poorly understood, and even those that are understood can be better leveraged for device applications. In an effort to make progress here, this thesis focused on clarifying spin relaxation in organic semiconductors, as well as spin-dependent transport. We have characterized

both in detail, and exploited the unique physics of a model system to achieve incredibly long relaxation times even at room temperature. Of course, there is always work to be done, and so we have also hoped to have laid the groundwork for future research studying organic semiconductor via magnetic resonance.

REFERENCES

[1] Market Research Future, "Global Organic Electronics Market by Material, Application and Region: Industry Analysis and Forecast 2020-2026," market research report, Market Research Future, US, 2020.

[2] N. S. Hush, "An Overview of the First Half-Century of Molecular Electronics," *Annals of the New York Academy of Sciences*, vol. 1006, no. 1, pp. 1–20, 2003.

[3] B. Raikes, "Where's the Display Market Headed?," *Information Display*, vol. 36, no. 5, pp. 34–38, 2020.

[4] Fortune Business Insights, "Organic Solar Cells Market Size, Share and COVID-19 Impact Analysis, By Application (Building Integrated Photovoltaic {BIPV}, Portable Electronics, Defense Application, Conventional Solar, and Others), and Regional Forecast, 2020-2027," FBI101555, Fortune, US, 2019.

[5] A. Moliton and R. C. Hiorns, "The origin and development of (plastic) organic electronics," *Polymer International*, vol. 61, no. 3, pp. 337–341, 2012.

[6] J. K. Borchardt, "Developments in organic displays," *Materials Today*, vol. 7, pp. 42–46, Sept. 2004.

[7] S. Kunić and Z. Šego, "OLED technology and displays," in *Proceedings ELMAR-2012*, pp. 31–35, Sept. 2012.

[8] C.-H. Kim and I. Kymissis, "Graphene–organic hybrid electronics," *Journal of Materials Chemistry C*, vol. 5, no. 19, pp. 4598–4613, 2017.

[9] H. Sirringhaus, "25th Anniversary Article: Organic Field-Effect Transistors: The Path Beyond Amorphous Silicon," *Advanced Materials*, vol. 26, no. 9, pp. 1319–1335, 2014.

[10] S. Himmelberger and A. Salleo, "Engineering semiconducting polymers for efficient charge transport," *MRS Communications*, vol. 5, pp. 383–395, Sept. 2015.

[11] S. Fratini, D. Mayou, and S. Ciuchi, "The Transient Localization Scenario for Charge Transport in Crystalline Organic Materials," *Advanced Functional Materials*, vol. 26, pp. 2292–2315, Apr. 2016.

[12] A. Köhler and H. Bässler, *Electronic Processes in Organic Semiconductors*. Wiley-VCH, 2015.

[13] P. Dirac, *The Principles of Quantum Mechanics*. The International Series of Monographs on Physics, Oxford University Press, fourth ed., 1958.

[14] M. A. Baldo, D. F. O'Brien, Y. You, A. Shoustikov, S. Sibley, M. E. Thompson, and S. R. Forrest, "Highly efficient phosphorescent emission from organic electroluminescent devices," *Nature*, vol. 395, p. 4, 1998.

[15] S. Schott, U. Chopra, V. Lemaur, A. Melnyk, Y. Olivier, R. Di Pietro, I. Romanov, R. L. Carey, X. Jiao, C. Jellett, M. Little, A. Marks, C. R. McNeill, I. McCulloch, E. R. McNellis, D. Andrienko, D. Beljonne, J. Sinova, and H. Sirringhaus, "Polaron spin dynamics in high-mobility polymeric semiconductors," *Nature Physics*, vol. 15, pp. 814–822, Aug. 2019.

[16] S. Tehrani, J. Slaughter, M. Deherrera, B. Engel, N. Rizzo, J. Salter, M. Durlam, R. Dave, J. Janesky, B. Butcher, K. Smith, and G. Grynkewich, "Magnetoresistive random access memory using magnetic tunnel junctions," *Proceedings of the IEEE*, vol. 91, pp. 703–714, May 2003.

[17] S.-S. Li, G.-L. Long, F.-S. Bai, S.-L. Feng, and H.-Z. Zheng, "Quantum computing," *Proceedings of the National Academy of Sciences*, vol. 98, pp. 11847–11848, Oct. 2001.

[18] J. S. Meena, S. M. Sze, U. Chand, and T.-Y. Tseng, "Overview of emerging nonvolatile memory technologies," *Nanoscale Research Letters*, vol. 9, p. 526, Sept. 2014.

[19] D. Sun, K. J. van Schooten, M. Kavand, H. Malissa, C. Zhang, M. Groesbeck, C. Boehme, and Z. Valy Vardeny, "Inverse spin Hall effect from pulsed spin current in organic semiconductors with tunable spin–orbit coupling," *Nature Materials*, vol. 15, pp. 863–869, Aug. 2016.

[20] W. Wagemans, P. Janssen, A. J. Schellekens, F. L. Bloom, P. A. Bobbert, and B. Koopmans, "The Many Faces of Organic Magnetoresistance," *SPIN*, Mar. 2012.

[21] S. Watanabe, K. Ando, K. Kang, S. Mooser, Y. Vaynzof, H. Kurebayashi, E. Saitoh, and H. Sirringhaus, "Polaron spin current transport in organic semiconductors," *Nature Physics*, vol. 10, pp. 308–313, Apr. 2014.

[22] S.-i. Kuroda, S. Watanabe, K. Ito, H. Tanaka, H. Ito, and K. Marumoto, "Electron Spin Resonance of Charge Carriers in Organic Field-Effect Devices," *Applied Magnetic Resonance*, vol. 36, p. 357, Oct. 2009.

[23] H. Matsui, D. Kumaki, E. Takahashi, K. Takimiya, S. Tokito, and T. Hasegawa, "Correlation between interdomain carrier hopping and apparent mobility in polycrystalline organic transistors as investigated by electron spin resonance," *Physical Review B*, vol. 85, Jan. 2012.

[24] H. Matsui and T. Hasegawa, "Direct Observation of Field-Induced Carrier Dynamics in Pentacene Thin-Film Transistors by Electron Spin Resonance Spectroscopy," *Japanese Journal of Applied Physics*, vol. 48, p. 04C175, Apr. 2009.

[25] K. Marumoto, S.-i. Kuroda, T. Takenobu, and Y. Iwasa, "Spatial Extent of Wave Functions of Gate-Induced Hole Carriers in Pentacene Field-Effect Devices as Investigated by Electron Spin Resonance," *Physical Review Letters*, vol. 97, p. 256603, Dec. 2006.

[26] K. Marumoto, T. Sakamoto, S.-i. Watanabe, H. Ito, and S.-i. Kuroda, "Electron Spin Resonance Observation of Gate-Induced Ambipolar Charge Carriers in Organic Devices," *Japanese Journal of Applied Physics*, vol. 46, pp. L1191–L1193, Dec. 2007.

[27] E. Tiesinga, P. J. Mohr, D. B. Newell, and B. N. Taylor, "Values of Fundamental Physical Constants," in *NIST Chemistry WebBook, NIST Standard Reference Database Number 69, Eds. P.J. Linstrom and W.G. Mallard*, Gaithersburg MD, 20899: National Institute of Standards and Technology, May 2019.

[28] J. J. Sakurai, *Modern Quantum Mechanics*. Addison-Wesley Publishing Company, revised edition ed., 1994.

[29] J. Harriman, *Theoretical Foundations of Electron Spin Resonance*. New York, New York: Academic Press, Inc., 1978.

[30] L. L. Foldy and S. A. Wouthuysen, "On the Dirac Theory of Spin 1/2 Particles and Its Non-Relativistic Limit," *Physical Review*, vol. 78, pp. 29–36, Apr. 1950.

[31] H. A. Bethe and E. E. Sapeter, *Quantum Mechanics of One- and Two-Electron Systems*. Germany: Springer-Verlag OHG, 1957.

[32] Z. V. Chraplyvy, "Reduction of Relativistic Two-Particle Wave Equations to Approximate Forms. II," *Physical Review*, vol. 92, pp. 1310–1355, Dec. 1953.

[33] G. E. Pake, *Paramagnetic Resonance: An Introductory Monograph*. Frontiers in Physics, W. A. Benjamin Inc., 1962.

[34] F. Gerson and W. Huber, *Electron Spin Resonance Spectroscopy of Organic Radicals*. Germany: Wiley-VCH, 2003.

[35] A. S. Mishchenko, H. Matsui, and T. Hasegawa, "Distribution of localized states from fine analysis of electron spin resonance spectra of organic semiconductors: Physical meaning and methodology," *Physical Review B*, vol. 85, Feb. 2012.

[36] J. A. Weil and J. R. Bolton, *Electron Paramagnetic Resonance*. John Wiley & Sons, Inc., second ed., 2007.

[37] L. Landau and E. Lifshitz, *Statistical Physics, Part 1*, vol. 5 of *Course of Theoretical Physics*. Pergamon Press, third ed., 1970.

[38] C. P. Slichter, *Principles of Magnetic Resonance*. Harper & Row Publishers, 1963.

[39] A. Zangwill, *Modern Electrodynamics*. Cambridge University Press, 2012.

[40] J. Olivero and R. Longbothum, "Empirical fits to the Voigt line width: A brief review," *Journal of Quantitative Spectroscopy and Radiative Transfer*, vol. 17, pp. 233–236, Feb. 1977.

[41] H. Tanaka, S.-i. Watanabe, H. Ito, K. Marumoto, and S.-i. Kuroda, "Direct observation of the charge carrier concentration in organic field-effect transistors by electron spin resonance," *Applied Physics Letters*, vol. 94, p. 103308, Mar. 2009.

[42] H. Tanaka, M. Hirate, S.-i. Watanabe, K. Kaneko, K. Marumoto, T. Takenobu, Y. Iwasa, and S.-i. Kuroda, "Electron spin resonance observation of charge carrier concentration in organic field-effect transistors during device operation," *Physical Review B*, vol. 87, Jan. 2013.

[43] M. C. J. M. Vissenberg and M. Matters, "Theory of the field-effect mobility in amorphous organic transistors," *Physical Review B*, vol. 57, pp. 12964–12967, May 1998.

[44] H. Matsui, T. Hasegawa, Y. Tokura, M. Hiraoka, and T. Yamada, "Polaron Motional Narrowing of Electron Spin Resonance in Organic Field-Effect Transistors," *Physical Review Letters*, vol. 100, Mar. 2008.

[45] S. Kawamura, A. Wakamatsu, S.-i. Kuroda, T. Takenobu, and H. Tanaka, "Microscopic observation of highly mobile charge carriers in organic transistors of semicrystalline conducting polymers," *Japanese Journal of Applied Physics*, vol. 57, p. 02CA04, Dec. 2017.

[46] H. Matsui, A. S. Mishchenko, and T. Hasegawa, "Distribution of Localized States from Fine Analysis of Electron Spin Resonance Spectra in Organic Transistors," *Physical Review Letters*, vol. 104, Feb. 2010.

[47] K. Marumoto, N. Arai, H. Goto, M. Kijima, K. Murakami, Y. Tominari, J. Takeya, Y. Shimoi, H. Tanaka, S.-i. Kuroda, T. Kaji, T. Nishikawa, T. Takenobu, and Y. Iwasa, "Microscopic mechanisms behind the high mobility in rubrene single-crystal transistors as revealed by field-induced electron spin resonance," *Physical Review B*, vol. 83, p. 075302, Feb. 2011.

[48] S.-i. Watanabe, H. Tanaka, H. Ito, S.-i. Kuroda, T. Mori, K. Marumoto, and Y. Shimoi, "Direct determination of interfacial molecular orientations in field-effect devices of P3HT/PCBM composites by electron spin resonance," *Organic Electronics*, vol. 12, pp. 716–723, Apr. 2011.

[49] H. Tanaka, A. Wakamatsu, M. Kondo, S. Kawamura, S.-i. Kuroda, Y. Shimoi, W.-T. Park, Y.-Y. Noh, and T. Takenobu, "Microscopic observation of efficient charge transport processes across domain boundaries in donor-acceptor-type conjugated polymers," *Communications Physics*, vol. 2, pp. 1–10, Aug. 2019.

[50] J. Jiang and R. Weber, "Elexys E500; EPR Spectrometer User's Manual Basic Operations," Apr. 2001.

[51] C. P. Poole, *Electron Spin Resonance; A Comprehensive Treatise on Experimental Techniques*. United States of America: John Wiley & Sons, Inc., second ed., 1983.

[52] J. S. Hyde, M. Pasenkiewicz-Gierula, A. Jesmanowicz, and W. E. Antholine, "Pseudo field modulation in EPR spectroscopy," *Applied Magnetic Resonance*, vol. 1, p. 483, Dec. 1990.

[53] H. P. Gavin, "The Levenberg-Marquardt algorithm for nonlinear least squares curve-fitting problems." presentation, 2020.

[54] A. Abragam, *The Principles of Nuclear Magnetism*. Amen House, London, E.C.4: Oxford University Press, 1961.

[55] E. J. Meijer, D. M. de Leeuw, S. Setayesh, E. van Veenendaal, B.-H. Huisman, P. W. M. Blom, J. C. Hummelen, U. Scherf, and T. M. Klapwijk, "Solution-processed ambipolar organic field-effect transistors and inverters," *Nature Materials*, vol. 2, pp. 678–682, Oct. 2003.

[56] R. Schmechel, A. Hepp, H. Heil, M. Ahles, W. Weise, and H. von Seggern, "Light-emitting field-effect transistor: Simple model and underlying functional mechanisms," in *Organic Field Effect Transistors II*, vol. 5217, pp. 101–111, SPIE, Nov. 2003.

[57] R. Chesterfield, C. Newman, T. Pappenfus, P. Ewbank, M. Haukaas, K. Mann, L. Miller, and C. Frisbie, "High Electron Mobility and Ambipolar Transport in Organic Thin-Film Transistors Based on a Pi-Stacking Quinoidal Terthiophene," *Advanced Materials*, vol. 15, no. 15, pp. 1278–1282, 2003.

[58] J. Zaumseil and H. Sirringhaus, "Electron and Ambipolar Transport in Organic Field-Effect Transistors," *Chemical Reviews*, vol. 107, pp. 1296–1323, Apr. 2007.

[59] T. B. Singh, S. Günes, N. Marjanović, N. S. Sariciftci, and R. Menon, "Correlation between morphology and ambipolar transport in organic field-effect transistors," *Journal of Applied Physics*, vol. 97, p. 114508, June 2005.

[60] S. Cho, J. Yuen, J. Y. Kim, K. Lee, and A. J. Heeger, "Ambipolar organic field-effect transistors fabricated using a composite of semiconducting polymer and soluble fullerene," *Applied Physics Letters*, vol. 89, p. 153505, Oct. 2006.

[61] S. Watanabe, H. Tanaka, H. Ito, K. Marumoto, and S. Kuroda, "ESR studies of ambipolar charge carriers in metal–insulator–semiconductor diodes of regioregular poly(3-hexylthiophene)/PCBM composites," *Synthetic Metals*, vol. 159, pp. 893–896, May 2009.

[62] H. Matsui and T. Hasegawa, "Field-Induced ESR Spectroscopy on Rubrene Single-Crystal Field-Effect Transistors," *MRS Proceedings*, vol. 1154, pp. 1154–B08–04, 2009.

[63] A. Onwubiko, W. Yue, C. Jellett, M. Xiao, H.-Y. Chen, M. K. Ravva, D. A. Hanifi, A.-C. Knall, B. Purushothaman, M. Nikolka, J.-C. Flores, A. Salleo, J.-L. Bredas, H. Sirringhaus, P. Hayoz, and I. McCulloch, "Fused electron deficient semiconducting polymers for air stable electron transport," *Nature Communications*, vol. 9, p. 416, Jan. 2018.

[64] M. Xiao, R. L. Carey, H. Chen, X. Jiao, V. Lemaur, S. Schott, M. Nikolka, C. Jellett, A. Sadhanala, S. Rogers, S. P. Senanayak, A. Onwubiko, S. Han, Z. Zhang, M. Abdi-Jalebi, Y. Zhang, T. H. Thomas, N. Mahmoudi, L. Lai, E. Selezneva, X. Ren, M. Nguyen, Q. Wang, I. Jacobs, W. Yue, C. R. McNeill, G. Liu, D. Beljonne, I. McCulloch, and H. Sirringhaus, "Charge transport physics of a unique class of rigid-rod conjugated polymers with fused-ring conjugated units linked by double carbon-carbon bonds," *Science Advances*, vol. 7, p. eabe5280, Apr. 2021.

[65] Z. Chen, M. J. Lee, R. Shahid Ashraf, Y. Gu, S. Albert-Seifried, M. Meedom Nielsen, B. Schroeder, T. D. Anthopoulos, M. Heeney, I. McCulloch, and H. Sirringhaus, "High-Performance Ambipolar Diketopyrrolopyrrole-Thieno[3,2-b]thiophene Copolymer Field-Effect Transistors with Balanced Hole and Electron Mobilities," *Advanced Materials*, vol. 24, no. 5, pp. 647–652, 2012.

[66] Y. Li, S. P. Singh, and P. Sonar, "A High Mobility P-Type DPP-Thieno[3,2-b]thiophene Copolymer for Organic Thin-Film Transistors," *Advanced Materials*, vol. 22, no. 43, pp. 4862–4866, 2010.

[67] X. Wan, C. Li, M. Zhang, and Y. Chen, "Acceptor–donor–acceptor type molecules for high performance organic photovoltaics – chemistry and mechanism," *Chemical Society Reviews*, vol. 49, no. 9, pp. 2828–2842, 2020.

[68] H. Bronstein, Z. Chen, R. S. Ashraf, W. Zhang, J. Du, J. R. Durrant, P. Shakya Tuladhar, K. Song, S. E. Watkins, Y. Geerts, M. M. Wienk, R. A. J. Janssen, T. Anthopoulos, H. Sirringhaus, M. Heeney, and I. McCulloch, "Thieno[3,2- *b*]thiophene-Diketopyrrolopyrrole-Containing Polymers for High-Performance Organic Field-Effect Transistors and Organic Photovoltaic Devices," *Journal of the American Chemical Society*, vol. 133, pp. 3272–3275, Mar. 2011.

[69] Z. Chen, H. Lemke, S. Albert-Seifried, M. Caironi, M. M. Nielsen, M. Heeney, W. Zhang, I. McCulloch, and H. Sirringhaus, "High Mobility Ambipolar Charge Transport in Polyselenophene Conjugated Polymers," *Advanced Materials*, vol. 22, no. 21, pp. 2371–2375, 2010.

[70] M. C. Gwinner, S. Khodabakhsh, H. Giessen, and H. Sirringhaus, "Simultaneous Optimization of Light Gain and Charge Transport in Ambipolar Light-Emitting Polymer Field-Effect Transistors," *Chemistry of Materials*, vol. 21, pp. 4425–4433, Oct. 2009.

[71] S. R. Chaudhari, J. M. Griffin, K. Broch, A. Lesage, V. Lemaur, D. Dudenko, Y. Olivier, H. Sirringhaus, L. Emsley, and C. P. Grey, "Donor–acceptor stacking arrangements in bulk and thin-film high-mobility conjugated polymers characterized using molecular modelling and MAS and surface-enhanced solid-state NMR spectroscopy," *Chemical Science*, vol. 8, no. 4, pp. 3126–3136, 2017.

[72] F. Kraffert, R. Steyrleuthner, C. Meier, R. Bittl, and J. Behrends, "Transient electrically detected magnetic resonance spectroscopy applied to organic solar cells," *Applied Physics Letters*, vol. 107, p. 043302, July 2015.

[73] A. J. Kupijai, K. M. Behringer, F. G. Schaeble, N. E. Galfe, M. Corazza, S. A. Gevorgyan, F. C. Krebs, M. Stutzmann, and M. S. Brandt, "Bipolar polaron pair recombination in polymer/fullerene solar cells," *Physical Review B*, vol. 92, Dec. 2015.

[74] B. Z. Tedlla, F. Zhu, M. Cox, J. Drijkoningen, J. Manca, B. Koopmans, and E. Goovaerts, "Understanding Triplet Formation Pathways in Bulk Heterojunction Polymer:Fullerene Photovoltaic Devices," *Advanced Energy Materials*, vol. 5, no. 2, p. 1401109, 2015.

[75] F. Kraffert, D. Bahro, C. Meier, M. Denne, A. Colsmann, and J. Behrends, "Transport-related triplet states and hyperfine couplings in organic tandem solar cells probed by pulsed electrically detected magnetic resonance spectroscopy," *Journal of Magnetic Resonance*, vol. 282, pp. 10–17, Sept. 2017.

[76] D. R. McCamey, K. J. van Schooten, W. J. Baker, S.-Y. Lee, S.-Y. Paik, J. M. Lupton, and C. Boehme, "Hyperfine-Field-Mediated Spin Beating in Electrostatically Bound Charge Carrier Pairs," *Physical Review Letters*, vol. 104, p. 017601, Jan. 2010.

[77] P. A. Bobbert, T. D. Nguyen, F. W. A. van Oost, B. Koopmans, and M. Wohlgenannt, "Bipolaron Mechanism for Organic Magnetoresistance," *Physical Review Letters*, vol. 99, p. 216801, Nov. 2007.

[78] J. Behrends, A. Schnegg, K. Lips, E. A. Thomsen, A. K. Pandey, I. D. W. Samuel, and D. J. Keeble, "Bipolaron Formation in Organic Solar Cells Observed by Pulsed Electrically Detected Magnetic Resonance," *Physical Review Letters*, vol. 105, p. 176601, Oct. 2010.

[79] C. Boehme and J. M. Lupton, "Challenges for organic spintronics," *Nature Nanotechnology*, vol. 8, pp. 612–615, Sept. 2013.

[80] V. Podzorov, E. Menard, A. Borissov, V. Kiryukhin, J. A. Rogers, and M. E. Gershenson, "Intrinsic Charge Transport on the Surface of Organic Semiconductors," *Physical Review Letters*, vol. 93, p. 086602, Aug. 2004.

[81] V. Podzorov, E. Menard, J. A. Rogers, and M. E. Gershenson, "Hall Effect in the Accumulation Layers on the Surface of Organic Semiconductors," *Physical Review Letters*, vol. 95, p. 226601, Nov. 2005.

[82] I. N. Hulea, S. Fratini, H. Xie, C. L. Mulder, N. N. Iossad, G. Rastelli, S. Ciuchi, and A. F. Morpurgo, "Tunable Fröhlich polarons in organic single-crystal transistors," *Nature Materials*, vol. 5, pp. 982–986, Dec. 2006.

[83] Y. Shimoi, K. Marumoto, and S. Kuroda, "Theoretical ESR g Values in Rubrene and Oligoacenes: Implication to Molecular Orientation at Interfaces in Organic FETs," *Molecular Crystals and Liquid Crystals*, vol. 566, pp. 33–37, Nov. 2012.

[84] Y. Takahashi, M. Tsuji, Y. Yomogida, T. Takenobu, Y. Iwasa, and K. Marumoto, "Electron Spin Resonance Study of Organic Interfaces in Ion Gel-Gated Rubrene Single-Crystal Transistors," *Applied Physics Express*, vol. 6, p. 041603, Mar. 2013.

[85] H. Tanaka, M. Kozuka, S.-i. Watanabe, H. Ito, Y. Shimoi, K. Takimiya, and S.-i. Kuroda, "Observation of field-induced charge carriers in high-mobility organic transistors of a thienothiophene-based small molecule: Electron spin resonance measurements," *Physical Review B*, vol. 84, Aug. 2011.

[86] Y. Tanaka, K. Kinashi, K. Kono, W. Sakai, and N. Tsutsumi, "Electron spin resonance and photoelectron yield spectroscopic studies for photocarrier behavior in photorefractive polymeric composites," *Organic Electronics*, vol. 68, pp. 248–255, May 2019.

[87] M. Tsuji, N. Arai, K. Marumoto, J. Takeya, Y. Shimoi, H. Tanaka, S.-i. Kuroda, T. Takenobu, and Y. Iwasa, "Electron Spin Resonance Study of Interface Trap States and Charge Carrier Concentration in Rubrene Single-Crystal Field-Effect Transistors," *Applied Physics Express*, vol. 4, p. 085702, July 2011.

[88] S.-i. Watanabe, K. Ito, H. Tanaka, H. Ito, K. Marumoto, and S.-i. Kuroda, "Electron Spin Resonance Observation of Gate-induced Charge Carriers in Organic Field-effect Devices Fabricated on Silicon Substrates," *Japanese Journal of Applied Physics*, vol. 46, p. L792, Aug. 2007.

[89] J. Tsurumi, H. Matsui, T. Kubo, R. Häusermann, C. Mitsui, T. Okamoto, S. Watanabe, and J. Takeya, "Coexistence of ultra-long spin relaxation time and coherent charge transport in organic single-crystal semiconductors," *Nature Physics*, vol. 13, pp. 994–998, Oct. 2017.

[90] H. Shimotani, H. Asanuma, J. Takeya, and Y. Iwasa, "Electrolyte-gated charge accumulation in organic single crystals," *Applied Physics Letters*, vol. 89, p. 203501, Nov. 2006.

[91] J. D. Yuen, A. S. Dhoot, E. B. Namdas, N. E. Coates, M. Heeney, I. McCulloch, D. Moses, and A. J. Heeger, "Electrochemical Doping in Electrolyte-Gated Polymer Transistors," *Journal of the American Chemical Society*, vol. 129, pp. 14367–14371, Nov. 2007.

[92] S. Ono, S. Seki, R. Hirahara, Y. Tominari, and J. Takeya, "High-mobility, low-power, and fast-switching organic field-effect transistors with ionic liquids," *Applied Physics Letters*, vol. 92, p. 103313, Mar. 2008.

[93] S. H. Kim, K. Hong, W. Xie, K. H. Lee, S. Zhang, T. P. Lodge, and C. D. Frisbie, "Electrolyte-Gated Transistors for Organic and Printed Electronics," *Advanced Materials*, vol. 25, no. 13, pp. 1822–1846, 2013.

[94] A. Goldman, "Electrostatic Gating of Ultrathin Films," *Annual Review of Materials Research*, vol. 44, pp. 45–63, July 2014.

[95] S. Z. Bisri, S. Shimizu, M. Nakano, and Y. Iwasa, "Endeavor of Iontronics: From Fundamentals to Applications of Ion-Controlled Electronics," *Advanced Materials*, vol. 29, no. 25, p. 1607054, 2017.

[96] C. Kloc, P. G. Simpkins, T. Siegrist, and R. A. Laudise, "Physical vapor growth of centimeter-sized crystals of α-hexathiophene," *Journal of Crystal Growth*, vol. 182, pp. 416–427, Dec. 1997.

[97] T. Kimura, Y. Otani, T. Sato, S. Takahashi, and S. Maekawa, "Room-Temperature Reversible Spin Hall Effect," *Physical Review Letters*, vol. 98, p. 156601, Apr. 2007.

[98] D. J. Hilton and C. L. Tang, "Optical Orientation and Femtosecond Relaxation of Spin-Polarized Holes in GaAs," *Physical Review Letters*, vol. 89, p. 146601, Sept. 2002.

[99] S. P. Dash, S. Sharma, R. S. Patel, M. P. de Jong, and R. Jansen, "Electrical creation of spin polarization in silicon at room temperature," *Nature*, vol. 462, pp. 491–494, Nov. 2009.

[100] H. Idzuchi, A. Fert, and Y. Otani, "Revisiting the measurement of the spin relaxation time in graphene-based devices," *Physical Review B*, vol. 91, p. 241407, June 2015.

[101] Y. Xia, W. Xie, P. P. Ruden, and C. D. Frisbie, "Carrier Localization on Surfaces of Organic Semiconductors Gated with Electrolytes," *Physical Review Letters*, vol. 105, p. 036802, July 2010.

[102] H. T. Yuan, M. Toh, K. Morimoto, W. Tan, F. Wei, H. Shimotani, C. Kloc, and Y. Iwasa, "Liquid-gated electric-double-layer transistor on layered metal dichalcogenide, SnS2," *Applied Physics Letters*, vol. 98, p. 012102, Jan. 2011.

[103] W. Xie, S. Wang, X. Zhang, C. Leighton, and C. D. Frisbie, "High Conductance 2D Transport around the Hall Mobility Peak in Electrolyte-Gated Rubrene Crystals," *Physical Review Letters*, vol. 113, p. 246602, Dec. 2014.

[104] W. Xie and C. D. Frisbie, "Organic Electrical Double Layer Transistors Based on Rubrene Single Crystals: Examining Transport at High Surface Charge Densities above 10^{13} cm $^{-2}$," *The Journal of Physical Chemistry C*, vol. 115, pp. 14360–14368, July 2011.

[105] S. Giannini and J. Blumberger, "Charge Transport in Organic Semiconductors: The Perspective from Nonadiabatic Molecular Dynamics," *Accounts of Chemical Research*, vol. 55, pp. 819–830, Mar. 2022.

APPENDIX A

DERIVATION OF THE LORENTZIAN LINESHAPE

The energy absorbed by the sample per unit time depends on its magnetization via

$$P = \frac{\mathrm{d}}{\mathrm{d}t}\mathcal{H} = -\frac{\mathrm{d}}{\mathrm{d}t}\sum_m \boldsymbol{\mu}_m \cdot \mathbf{B} = -V\frac{\mathrm{d}}{\mathrm{d}t}\mathbf{M}\cdot\mathbf{B}, \tag{A.1}$$

while the rate of change of the magnetic moment of a single species follows from the Heisenberg equation of motion as

$$i\hbar\frac{\mathrm{d}}{\mathrm{d}t}\boldsymbol{\mu} = [\boldsymbol{\mu},\mathcal{H}] = -i\hbar g\mu_B\boldsymbol{\mu}\times\mathbf{B}. \tag{A.2}$$

This would suggest

$$\frac{\mathrm{d}\mathbf{M}}{\mathrm{d}t} = -g\mu_B\mathbf{M}\times\mathbf{B}, \tag{A.3}$$

which matches the classical result. However, this differential equation does not account for the observed decay of bulk magnetization. We know from that there is some preferred z-magnetization in the presence of $\mathbf{B}_0$. Thus if the system moves out of equilibrium it will have a tendency to return to M_z^0. The amount of time this requires is known as the *spin-lattice relaxation time*, T_1, because the z-aligned spins can only change by exchanging energy with the molecular lattice. The transverse components of magnetization, M_x and M_y, are zero on average in $\mathbf{B}_0$, and there must thus be a characteristic timescale for the system to return to this state. This is known as the *transverse relaxation time*, T_2.

With these phenomenological additions, the magnetization equations of motion are

$$\frac{\mathrm{d}\mathbf{M}}{\mathrm{d}t} = -g\mu_B\mathbf{M}\times\mathbf{B} - \mathbf{T}\cdot(\mathbf{M} - M_z^0\hat{\mathbf{z}}) \tag{A.4}$$

where

$$\mathbf{T} \equiv (1/T_2, 1/T_2, 1/T_1). \tag{A.5}$$

These are known as the *Bloch equations*[38]. If we include in **B** only a static magnetic field, the sample will reach M_z^0 and stop absorbing energy. We must present a constant driving force to move the system out of equilibrium. This is normally done with a magnetic field that oscillates perpendicular to the static field. We shall take the field to be oriented along the x-axis and we shall write it as the sum of two oppositely rotating fields:

$$\mathbf{B}_1 = B_{\mathrm{mw}}\eta(\cos\omega_{\mathrm{mw}}t, \sin\omega_{\mathrm{mw}}t, 0) + B_{\mathrm{mw}}\lambda(\cos\omega_{\mathrm{mw}}t, -\sin\omega_{\mathrm{mw}}t, 0). \tag{A.6}$$

In a frame rotating with this field, the components of magnetization are

$$\begin{aligned} M^- &= M_x\cos\omega_{\mathrm{mw}}t + M_y\sin\omega_{\mathrm{mw}}t \\ M^+ &= -M_x\sin\omega_{\mathrm{mw}}t + M_y\cos\omega_{\mathrm{mw}}t \\ M^z &= M_z, \end{aligned} \tag{A.7}$$

and the Bloch equations are[29]

$$\begin{aligned} \frac{dM^-}{dt} &= M^+(\omega_{\mathrm{mw}} - \omega_{\mathrm{L}}) - \frac{M^-}{T_2} + \lambda B_{\mathrm{mw}}M^z\sin 2\omega_{\mathrm{mw}}t \\ \frac{dM^+}{dt} &= -M^-(\omega_{\mathrm{mw}} - \omega_{\mathrm{L}}) - \frac{M^+}{T_2} + \lambda B_{\mathrm{mw}}M^z\cos 2\omega_{\mathrm{mw}}t + M^z\eta B_{\mathrm{mw}} \\ \frac{dM_z}{dt} &= M^+B_{\mathrm{mw}}\eta - \frac{M_z - M_z^0}{T_1} + B_{\mathrm{mw}}\lambda(M^+\cos 2\omega_{\mathrm{mw}}t + M^-\sin 2\omega_{\mathrm{mw}}t). \end{aligned} \tag{A.8}$$

We are interested in the magnetization component that is static in this frame. This component follows the η component of the oscillating field and is not strongly influenced by the counter-rotating λ component. We therefore find the steady state solutions to these Bloch equations with $\eta = 1$ and $\lambda = 0$. They are

$$\begin{aligned} M^- &= M_z^0\gamma\frac{B_{\mathrm{mw}}T_2^2(\omega_{\mathrm{mw}} - \omega_{\mathrm{L}})}{1 + (\omega_{\mathrm{L}} - \omega_{\mathrm{mw}})^2T_2^2 + \gamma^2B_{\mathrm{mw}}^2T_1T_2} \\ M^+ &= M_z^0\gamma\frac{B_{\mathrm{mw}}T_2}{1 + (\omega_{\mathrm{L}} - \omega_{\mathrm{mw}})^2T_2^2 + \gamma^2B_{\mathrm{mw}}^2T_1T_2} \\ M_z &= M_z^0\frac{1 + (\omega_{\mathrm{L}} - \omega_{\mathrm{mw}})^2T_2^2}{1 + (\omega_{\mathrm{L}} - \omega_{\mathrm{mw}})^2T_2^2 + \gamma^2B_{\mathrm{mw}}^2T_1T_2}. \end{aligned} \tag{A.9}$$

From (A.7) we see $M_x = M^-\cos\omega_{\mathrm{mw}}t - M^+\sin\omega_{\mathrm{mw}}t$. Defining the complex susceptibility $\chi = \chi' + i\chi''$ with components

$$\begin{aligned} \chi' &= M_z^0\gamma\frac{T_2^2(\omega_{\mathrm{mw}} - \omega_{\mathrm{L}})}{1 + (\omega_{\mathrm{L}} - \omega_{\mathrm{mw}})^2T_2^2 + \gamma^2B_{\mathrm{mw}}^2T_1T_2} = \frac{M^-}{B_{\mathrm{mw}}} \\ \chi'' &= M_z^0\gamma\frac{T_2}{1 + (\omega_{\mathrm{L}} - \omega_{\mathrm{mw}})^2T_2^2 + \gamma^2B_{\mathrm{mw}}^2T_1T_2} = \frac{M^+}{B_{\mathrm{mw}}}, \end{aligned} \tag{A.10}$$

we find

$$M_x = B_{\mathrm{mw}}(\chi' \cos \omega_{\mathrm{mw}} t - \chi'' \sin \omega_{\mathrm{mw}} t) = \mathscr{R}e\left[\chi B_{\mathrm{mw}} e^{i\omega_{\mathrm{mw}} t}\right]. \tag{A.11}$$

The power absorbed by the steady-state sample over one cycle of the microwave field follows as

$$\begin{aligned}
\overline{P} &= -V\frac{\omega}{2\pi}\int_0^{\frac{2\pi}{\omega}} \frac{d}{dt}\mathbf{M}\cdot\mathbf{B}dt = -V\frac{\omega}{2\pi}\int_0^{\frac{2\pi}{\omega}} \frac{d}{dt}(2M_x B_{\mathrm{mw}}\cos\omega_{\mathrm{mw}} t + M_z B_0)dt \\
&= -V\frac{\omega}{2\pi}\int_0^{\frac{2\pi}{\omega}} \frac{d}{dt}(2\chi' B_{\mathrm{mw}}^2\cos^2\omega_{\mathrm{mw}} t - 2\chi'' B_{\mathrm{mw}}^2\cos\omega_{\mathrm{mw}} t\sin\omega_{\mathrm{mw}} t)dt \\
&= -V\frac{\omega}{2\pi}\int_0^{\frac{2\pi}{\omega}} \left[-4\omega_{\mathrm{mw}}\chi' B_{\mathrm{mw}}^2\cos\omega_{\mathrm{mw}} t\sin\omega_{\mathrm{mw}} t - 2\omega_{\mathrm{mw}}\chi'' B_{\mathrm{mw}}^2(\cos^2\omega_{\mathrm{mw}} t - \sin^2\omega_{\mathrm{mw}} t)\right]dt \\
&= \frac{V}{4\pi}\omega_{\mathrm{mw}} B_{\mathrm{mw}}^2\chi''.
\end{aligned} \tag{A.12}$$

APPENDIX B

DENSITY MATRIX FORMALISM

The density matrix formalism is useful in describing the behavior of systems whose composite particles are not all in the same quantum state. For these ensembles of particles, the average value of an observable A is given by the *ensemble average*, which is the mean of the expectation value of A with respect to each quantum state in the system. For example, the ensemble average for an ensemble with i different states is simply

$$\overline{\langle A \rangle} = \sum_i w_i \langle \psi_i | A | \psi_i \rangle , \tag{B.1}$$

where w_i is the probabilistic weight of the state ψ_i. Inserting the identity operator twice then gives

$$\begin{aligned}
\overline{\langle A \rangle} &= \sum_i w_i \sum_{n,m} \langle \psi_i | m \rangle \ \langle m | A | n \rangle \langle n | \psi_i \rangle \\
&= \sum_{n,m} \langle n | \left(\sum_i w_i \, | \psi_i \rangle \langle \psi_i | \right) | m \rangle \ \langle m | A | n \rangle \\
&= \sum_{n,m} \langle n | \rho | m \rangle \ \langle m | A | n \rangle \\
&= \mathrm{Tr}[\rho A].
\end{aligned} \tag{B.2}$$

The term defined by the parentheses, ρ, is known as the *density operator*. It is useful because it captures all relevant information about the ensemble: both the states present and each of their statistical weights. Since the trace of a matrix is invariant under a change of representation, $[A]$ can usually be evaluated easily by choosing a convenient basis.

The time evolution of the density operator can be calculated by applying the Schrödinger equation to the state kets: *

$$\begin{aligned} i\hbar\frac{\partial\rho}{\partial t} &= i\hbar\sum_i w_i\left(\frac{\partial|\psi_i\rangle}{\partial t}\langle\psi_i| + |\psi_i\rangle\frac{\partial\langle\psi_i|}{\partial t}\right) \\ &= \sum_i w_i\left(\mathcal{H}|\psi_i\rangle\langle\psi_i| - |\psi_i\rangle\langle\psi_i|\mathcal{H}\right) \\ &= -[\rho,\mathcal{H}]. \end{aligned} \tag{B.3}$$

This equation is the *Liouville-von Neumann equation*. It is the quantum-mechanical version of the Liouville theorem in classical statistical mechanics. From this perspective, the term *density* is apposite since it describes the rate of change of density at a point in phase space.

B.1 The density operator for a system at thermal equilibrium

To derive an expression for the density operator for a system at thermal equilibrium, it is necessary to introduce an analogue for entropy. The quantity

$$\sigma = -\operatorname{Tr}[\rho\ln\rho] \tag{B.4}$$

will do: in the basis that diagonalizes ρ—called $|r\rangle$ here—the above expression becomes

$$\sigma = -\sum_r \rho_{rr}\ln\rho_{rr}, \tag{B.5}$$

which is maximized for a completely random ensemble (since all the matrix elements are equal) and vanishes for a pure ensemble (since only one matrix element is nonzero and it is unity). From this expression, it is clear that the normalization condition is

$$\sum_r \rho_{rr} = 1. \tag{B.6}$$

Moreover, because thermal equilibrium implies $\partial\rho/\partial t = 0$, the density operator commutes with the Hamiltonian. This means that the states that diagonlize the density matrix are also the energy eigenstates.

Thermal equilibrium is defined as the state of the system at which entropy is maximized. Writing this as

$$\delta\sigma = 0, \tag{B.7}$$

*The corresponding equation assumes that the statistical weights of the states do not change in time, i.e., the system is free from external forces.

variational calculus can be used to find the ρ that satisfies this condition. At equilibrium, the energy of the system and the states themselves do not vary, so it is necessary to include the constraints

$$\delta[\mathcal{H}] = \sum_n \delta\rho_{nn} E_n = 0 \qquad\qquad \delta(\mathrm{Tr}[\rho]) = \sum_n \delta\rho_{nn} = 0. \tag{B.8}$$

Doing so with Lagrange multipliers gives the entropy maximization condition as

$$\sum_n \delta\rho_{nn} \left[(\ln\rho_{nn} + 1) + \beta E_n + \gamma\right] = 0, \tag{B.9}$$

which requires

$$\rho_{nn} = \exp[-\beta E_n - \gamma - 1]. \tag{B.10}$$

Eliminating γ with the the normalization requirement (B.6) then gives

$$\rho_{nn} = \frac{\exp[-\beta E_n]}{\sum_{n'} \exp[-\beta E'_n]}, \tag{B.11}$$

which looks suspiciously like the Boltzmann probability of a state with energy E_n in classical statistical mechanics. In fact, introducing the partition function,

$$\begin{aligned} Z &= \sum_n e^{-\beta E_n} \\ &= \mathrm{Tr}\left[e^{-\beta\mathcal{H}}\right], \end{aligned} \tag{B.12}$$

shows that the density operator can be written in the form

$$\rho = \frac{e^{-\beta\mathcal{H}}}{Z}, \tag{B.13}$$

which makes the calculation of any ensemble average straightforward:

$$\begin{aligned} \overline{\langle A\rangle} &= \mathrm{Tr}[\rho A] \\ &= \mathrm{Tr}\left[\frac{e^{-\beta\mathcal{H}} A}{\mathrm{Tr}\left[e^{-\beta\mathcal{H}}\right]}\right] \\ &= \frac{\sum_n e^{-\beta E_n}\langle A\rangle_n}{\sum_n e^{-\beta E_n}}. \end{aligned} \tag{B.14}$$

APPENDIX C

CONVERTING TENSORS FROM THE CARTESIAN TO THE SPHERICAL BASIS

A tensor is a collection of components that changes in a prescribed way under a change of coordinates. The *rank* of a tensor is determined by the number of unique indices required to uniquely label each component. Scalars are rank-zero tensors, vectors rank-one tensors, and matrices rank-two tensors. Two popular basis states for expressing tensors are the Cartesian and spherical coordinates. In the Cartesian basis, the components of tensors are written in the form A_a for vectors and A_{ab} for matrices (with a and b ranging over the Cartesian directions x, y, and z), while in the spherical basis tensors have the form $\mathcal{A}_k^{(q)}$, where q can range from zero to the maximum rank of the tensor, and for each value of q the index k can range from $-q$ to $+q$ in unit steps.

The conversions from a vector in the Cartesian basis to a rank-one tensor in the spherical basis are

$$A_0^{(1)} = A_z \qquad\qquad A_{\pm 1}^{(1)} = \mp\frac{1}{\sqrt{2}}(A_x \pm iA_y). \tag{C.1}$$

Here, q can only equal 1, so k ranges from -1 to +1. Thus, regardless of the coordinate system, three unique components are defined.

The conversions from a matrix in the Cartesian basis to a rank-two tensor in the spherical basis are

$$A_0^{(0)} = \frac{1}{3}\sum_q A_{qq} \tag{C.2}$$

$$A_0^{(1)} = \frac{1}{2}(A_{xy} - A_{yx}) \tag{C.3}$$

$$A_{\pm 1}^{(1)} = \mp\frac{1}{\sqrt{2}}\left[(A_{yz} - A_{zy}) \pm i(A_{zx} - A_{xz})\right] \tag{C.4}$$

$$A_0^{(2)} = \sqrt{\frac{3}{2}}\left[(A_{zz} - \frac{1}{3}\sum_q A_{qq}\right] \tag{C.5}$$

$$A_{\pm 1}^{(2)} = \mp\frac{1}{2}\left[(A_{zx} - A_{xz}) \pm (A_{zy} - Ayz)\right] \tag{C.6}$$

$$A_{\pm 2}^{(2)} = \frac{1}{2}\left[A_{xx} - A_{yy} + i(A_{xy} - A_{yx}) - \frac{1}{3}\sum_q A_{qq}\right]. \tag{C.7}$$

In this case, q ranges from 0 to 2. With the corresponding k values, there are nine unique elements, as expected.

APPENDIX D

SUPPLEMENTAL INFORMATION TO CHAPTER 7

D.1 Spin relaxation data for an ion-gel-gated rubrene single-crystal device at -1.0 V

Figure D.1(a) shows the dependence of T_1, T_2, and T_2' on temperature for an ion-gel-gated rubrene single-crystal capacitor held at -1.0 V. The behavior observed is the same as that seen in the -1.5 V and -0.4 V devices (see Chapter 7): relaxation times are on the order of microseconds at room temperature, relaxation times *increase* rather than decrease with temperature, and relaxation times are quite stable throughout the entire temperature range. Figure D.1(b) shows the fit to the data of T_2' as predicted by the Redfield equations (7.1) for a temperature-activated motion frequency.

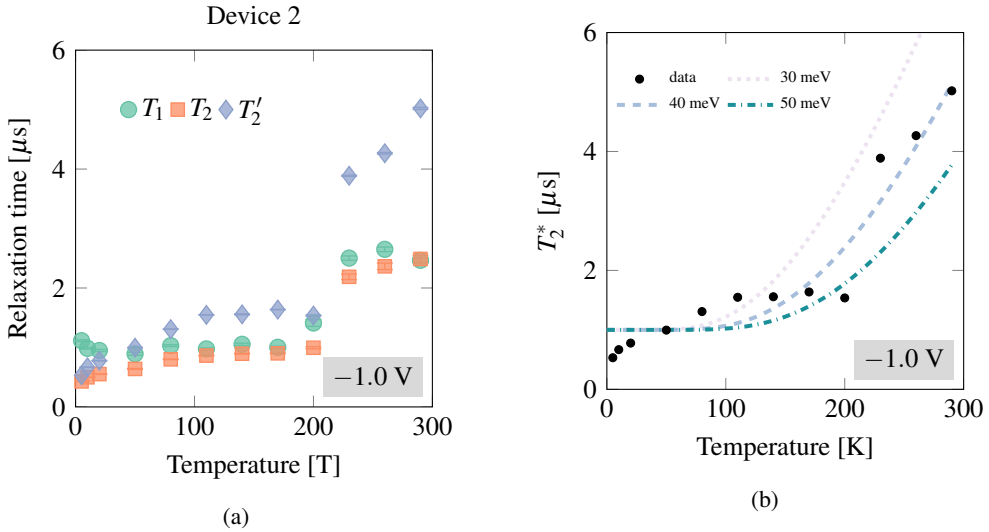

Fig. D.1 **(a)** Relaxation times and **(b)** fits to the Redfield equation ((7.1)) with a temperature-activated motion frequency for an ion-gel-gated rubrene single-crystal gated at -1.0 V.